William & Mary
CHARTERED 1693

W&M ScholarWorks

Dissertations, Theses, and Masters Projects

Theses, Dissertations, & Master Projects

2018

Development of Large-Scale Unstructured Grid Storm Surge and Sub-Grid Inundation Models for Coastal Applications

Zhuo Liu
College of William and Mary - Virginia Institute of Marine Science, lz80521@gmail.com

Follow this and additional works at: https://scholarworks.wm.edu/etd

 Part of the Oceanography Commons

Recommended Citation

Liu, Zhuo, "Development of Large-Scale Unstructured Grid Storm Surge and Sub-Grid Inundation Models for Coastal Applications" (2018). *Dissertations, Theses, and Masters Projects.* Paper 1550153651.
http://dx.doi.org/10.25773/v5-5b4x-1784

This Dissertation is brought to you for free and open access by the Theses, Dissertations, & Master Projects at W&M ScholarWorks. It has been accepted for inclusion in Dissertations, Theses, and Masters Projects by an authorized administrator of W&M ScholarWorks. For more information, please contact scholarworks@wm.edu.

Development of Large-Scale Unstructured Grid Storm Surge and Sub-Grid Inundation Models for Coastal Applications

---

A Dissertation

Presented to

The Faculty of the School of Marine Science

The College of William and Mary in Virginia

In Partial Fulfillment

of the Requirements for the Degree of

Doctor of Philosophy

---

by

Zhuo Liu

August 2018

APPROVAL PAGE

This dissertation is submitted in partial fulfillment of

the requirements for the degree of

Doctor of Philosophy

Zhuo Liu

Approved by the Committee, August 2018

Harry V. Wang, Ph. D.
Committee Chair / Advisor

Yinglong J. Zhang, Ph. D.

Jian Shen, Ph. D.

Carlton H. Hershner, Ph. D.

John M. Klinck, Ph. D.
Old Dominion University
Norfolk, Virginia

Table of Contents

ACKNOWLEDGEMENTS

Of those who have been greatly helpful in the completion of this dissertation, I would like to first express my sincere gratitude to my advisor, Dr. Harry V. Wang, whose support and guidance throughout the course of this research effort has been invaluable to me. I am grateful to have Harry as my mentor and friend and I am excited to continue our collaborations.

I would also like to express my appreciation to the rest of my committee members: Dr. Joseph Zhang, Dr. Jian Shen, Dr. Carl Hershner, and Dr. John Klinck, who have generously offered valuable remarks and constructive feedback over the course of this dissertation effort, as well as Dr. Iris Anderson's graciously serving as the moderator for my dissertation defense.

Furthermore, my sincere thanks go to all my friends at VIMS, especially Mr. Mac Sisson, Dr. Derek Loftis, Dr. Yongjin Xiao, Dr. Ya Wang, Dr. Fei Ye, Dr. Zhengui Wang, Dr. Jiabi Du, Dr. Xiaoteng Shen, Mr. Qubin Qin, Mr. Jingwei Song, Mr. Fei Da, Miss Xun Cai, and all my fellow Chinese friends, for their help and encouragement during this study.

Finally, and foremost, I would like to give special thanks to my wife, Bin, for her understanding and encouragement, and my parents for their support throughout this research endeavor.

LIST OF TABLES

LIST OF FIGURES

ABSTRACT

Storm surge and inundation induced by hurricanes and nor'easters pose a profound threat to coastal communities and ecosystems. These storm events with powerful winds, heavy precipitation, and strong wind waves can lead to major flooding for cities along U.S. Coasts. Recent examples of Hurricane Irene (2011) in North Carolina and Virginia and Hurricane Sandy (2012) in New York City not only demonstrated the immense destructive power by the storms, but also revealed the obvious, crucial need for improved forecasting of storm tide and inundation.

In part I, a large-scale unstructured-grid 3-D barotropic storm tide model SCHISM (Semi-implicit Cross-scale Hydroscience Integrated System Model) is developed with open ocean boundary aligning along the 60-degree West longitude to catch most Atlantic hurricanes that may make landfall along U.S. East and Gulf Coasts. The model, driven by high-resolution NAM (North America Mesoscale) and ECMWF (European Centre for Medium-Range Weather Forecasts) atmospheric fields, was coupled with Wind Wave Model (WWMIII) to account for wave effects, and used to simulate storm surge in 3-D barotropic mode rather than the traditional 2-D vertical average mode. For Hurricane Sandy, the fully coupled wave-current interaction 3-D model using ECMWF atmospheric forcing performs the best. The storm tide results match well with observation at all nine NOAA tidal gauges along the East Coast. The maximum total water level in New York City, is accurately simulated with absolute error of amplitude less than 8 cm, and timing difference within 10 minutes. The scenarios of "2-D" versus "3-D" and "with" versus "without" wind wave model were compared and discussed in details. Overall, the wave contribution amounts to 5-10% of surge elevation during the event. Also, the large-scale model with similar setup is applied to hindcasting storm tide during Hurricane Irene and the results are excellent when compared with observed water level along Southeast Coast and inside Chesapeake Bay.

In part II, a high-resolution sub-grid inundation model ELCIRC-sub (Eulerian-Lagrangian CIRCulation) was developed from the original finite-volume-based ELCIRC model. It utilized the sub-grid method for imbedding high-resolution topography/bathymetry data into the traditional model grid and delivering the inundation simulation on the street level scale. The ELCIRC-sub contains an efficient non-linear solver to increase the accuracy and was executed in the MPI (Message Passing Interface) parallel computing platform to vastly enlarge the water shed coverage, and to expand the numbers of sub-grids allowed. The ELCIRC-sub is first validated with a wetting/drying analytic solution and then applied in New York City for Hurricane Sandy (2012). Temporal comparisons with NOAA and USGS water level gauges showed excellent performance with an average error on the order of 10 cm. It accurately captured the highest surge (during Hurricane Sandy) at Kings Point on both maximum surge height and the explosive surge profile. Spatial comparisons of the modeled peak water level at 80 locations around New York City showed an average error less than 13 cm. The modeled maximum modeled inundation extent also matched well with 80% of the FEMA flooding map. In terms of robustness and efficiency for practical application, ELCIRC-sub surpasses the prototype model UnTRIM^2.

Development of Large-Scale Unstructured Grid Storm Surge and Sub-Grid Inundation Models for Coastal Applications

CHAPTER 1. Introduction

1.1. Literature Review

A storm surge is a rise in sea level that occurs during tropical or extra-tropical cyclones (also known as hurricanes or northeasters, respectively), whose water level height is far above the normal astronomical tide (NWS, 2009). During these events, the wind and pressure-induced forces push the water onto shore rapidly, causing coastal flooding in a short time and over a large area. As a result, the infrastructure service can be broken down, the transportation interrupted, and the cities brought to a standstill; making storm surges very dangerous to coastal regions. Several distinct processes are responsible for the increase of the water level during storms: the atmospheric pressure, the wind fields, the effects of Coriolis force, the wind wave, and the rainfall (Harris, 1963). Coastal inundation induced by storm surge along the U.S. East Coast and Gulf Coast is a substantial threat to residential properties, community infrastructure, and human life each year. For example, Hurricane Katrina (2005) caused the displacement of 1 million people from the central Gulf Coast and total damage of economical loss exceeding 105 billion, making it the costliest hurricane in the US history. Hurricane Irene (2011), which made landfall in North Carolina and went on to cause devastating flooding in several Northeastern states, resulted in $15.8 billion in damage, much of it due to inland flooding (NOAA, 2011). Hurricane Sandy (2012) made landfall along the New Jersey Coast, and resulted in an enormous impact on life and property damage in New York City area, with the estimated cost exceeding $50 billion along the eastern seaboard (NOAA, 2012). Given the projected sea-level rise and increase in storm intensity and/or frequency, the severity and the damage of the flooding is expected to be exacerbated and occur even during a moderate storm. Since the prediction of storm surge and land

flooding is highly interdisciplinary in nature involving atmospheric sciences, hydrology, hydraulics, oceanography, coastal engineering, geographic information, and computer sciences, the numerical modeling and the advanced observation system have been recognized to be the best approaches to advance science, improve technology, and make accurate prediction for realistically combat storm surge and coastal inundation.

Many numerical models have been built for storm surge and inundation predictions in different studies (Blumberg and Mellor, 1987; Casulli and Stelling, 2011; Flather et al., 1991; Jelesnianski et al., 1992; Westerink et al., 1994; Zhang and Baptista, 2008). Among them, one of the most commonly used storm surge model: Sea, Lake, and Overland Surges from Hurricanes (SLOSH) is currently the official storm surge forecast model used by the NOAA and the US government (Glahn et al., 2009; Jelesnianski et al., 1992). Due to the limited number of structured grid cells and simple dynamics in the SLOSH model, it is usually inadequate to deal with complex geometries in the waterways and shoreline and the land topography, which is part of the reason its predictions are on the order of 20% error compared with the observations. An unstructured-grid cross-scale model such as SCHISM can highly resolve coastal region and deep ocean in an effective and efficient way.

Most storm surge simulation has been performed under 2-D hydrodynamic models including SLOSH. However, 2-D models usually under-predict storm surge height since they approximate the entire water column by integrating and averaging velocity from surface to bottom (Weaver and Luettich, 2010; Weisberg and Zheng, 2008; Zheng et al, 2013). Weisberg and Zheng (2008) found that when the same bottom drag coefficient was used for both 2-D and 3-D simulations, the latter simulates larger surge heights.

Since 2-D models simulate the depth-averaged velocity that is usually larger than the near bottom velocity simulated in 3-D models, the 2-D models generate a larger bottom stress than the 3-D models. With the pressure gradient being primarily balanced between the surface and bottom stresses, if the bottom stress is larger, the vertically integrated pressure gradient force must be smaller in 2-D models because the surface wind stress is the same for both models. Hence, the simulated surface slope is smaller for the 2-D simulation, and the storm surges are smaller at most locations. Uncertainties in both surface wind stress and bottom stress parameterizations are important for either 2-D or 3-D surge simulations, and comparisons between 2-D and 3-D simulations, each with the same wind stress parameterization, are determined by differences in their bottom stress.

In 2-D models, the effect of stratification on eddy viscosity for transferring wind momentum into the water column is over-simplified, resulting in under-prediction of the wind-induced set-up and set-down. For example, all of the 2-D models including the ADCIRC model used by U.S. Army Engineer Research and Development Center (2015), Stevens Institute NYHOPS model (Orton et al., 2012), Stony Brook Surge Model^2 (DiLiberto et al., 2011), SLOSH model (Forbes et al., 2014) under-predicted the maximum surge by 0.3 - 1.0 m (about 10-25% relative error) in the modeling of storm surge during Hurricane Sandy (2012) in New York Harbor. The 3-D SCHISM includes the effects of the vertical turbulence on distributing the vertical momentum and uses near bottom layer velocity rather than the vertically-averaged velocity for calculating bottom friction as a function of wave and current interaction.

Wind waves are found to play an important role in storm surge modeling particularly during the storms when the high waves generated in open sea propagate into the shallow

water and break while entering shallow coastal waters. In the process, the decrease of large wave energy was transformed into the radiation stress, the other form of energy, affecting the total water level. Studies have found that wave-induced radiation force is proportion to the gradients of the wave radiation stress and the latter adds incrementally to the storm surge height compared to the case without the presence of waves (Longuet-Higgins and Stewart,1964; Phillips, 1977; Svendsen, 2006). The contributions to the modeled surge heights by wind wave coupled models were found to be about 5-15%. (Huang et al., 2010; Luettich and Westerink, 1999; Zheng et al., 2013). The SCHISM model is fully coupled with the Wind Wave Model (WWMIII) to account for the effects by wave-current interaction (Roland et al., 2012). It will be shown later that accounting for the effects of the wind wave in storm surge simulation leads to the reduction of the average errors of the total storm surge elevation.

The U.S. East Coast and the Gulf Coast are regions that are constantly under threat by severe storms, so it is highly desired to have a large-scale unstructured grid storm surge model that is accurate and efficient, and that can be coupled operationally with a large-scale atmospheric forecast model. Since the hurricane forerunners significantly affect coastal water elevation several days in advance of actual landfalls, the model domain must be large enough to fully contain the storms while it is still far offshore. In doing so, the model (1) can account for the remote effects induced by Ekman and continental shelf wave dynamics, (2) has the advantage of catching as many as hurricanes passing through the Western Atlantic Ocean, (3) makes the open boundary far away from the coast to exclude hurricane's own effect on the boundary condition, and (4) can easily simulate the effect of the long-term sea-level rise variation from the deep ocean.

The atmospheric models chosen to drive SCHISM are NOAA's high frequency forecast from NAM (North American Mesoscale) with 5km spatial resolution (Roger et al., 2005) and ECMWF's 5km/12km-resolution atmospheric forecast products (European Centre for Medium-Range Weather Forecasts) (Magnusson et al., 2014). NAM and ECMWF are two state-of-the-art wind forecast products which are robust, reliable, and have sufficient spatial and temporal coverage in the North America. The wind, pressure, and precipitation fields are interpolated onto SCHISM's unstructured grid and coupled in time and space seamlessly for storm surge simulations.

The SELFE model, a previous version of SCHISM, has successfully simulated 2003 Hurricane Isabel (Cho, 2009), 2008 Hurricane Ike (Teng, 2012), and 2012 Hurricane Sandy (Loftis, 2014). Transitioning from SELFE to SCHISM, several new capabilities have been added: (1) horizontal quad-triangular grid and highly flexible vertical grid system; (2) coupling with wind wave model WWMIII; (3) new advection scheme for the momentum equation with iterative solver; (4) new viscosity formulation to effectively filter out spurious modes without introducing excessive dissipation; (5) a high-order implicit advection scheme for transport equation to handle wide range of courant numbers, which leads to model polymorphism that unifies 1D/2D/3D cells in one single model grid. Liu et al. (2018) has applied the new SCHISM model to study the impacts of small-scale structures on estuarine circulation in the Chesapeake Bay. To expand upon the new capabilities, this study will make use of the latest version of the SCHISM model with the parallel computing power for a large-scale wind wave-coupled storm surge simulation. The model domain covers the Western Atlantic Ocean, U.S. East Coast,

Caribbean Seas, and Gulf Coasts from 98°W to 60°W and from 8°N to 46°N and the model is setup for simulating both 2012 Hurricane Sandy and 2011 Hurricane Irene.

Coastal inundation modeling with wetting and drying process is as important as storm surge simulation. Water movements across the land boundary onto terrestrial surface is a complicated process; in a strict sense a rigorous street-level scale inundation simulation is almost impossible, until the existence of the LIDAR (LIght Detection And Ranging) data. In recent years, the LIDAR data with detailed bathymetric data at a horizontal resolution of 1-5 meters have become available. Recognizing the power of LIDAR data which can and should be used in conjunction with numerical modeling, Casulli and Stelling (2011) are the first to develop a sub-grid model along with the nonlinear solver to account for the nonlinear relationship between total water volume and the raised water level. The sub-grid method was formulated to intrinsically account for sub-grid bathymetric details and more accurately calculating the volume of water transported leading to substantially improved accuracy without increasing the corresponding computational effort.

The idea of sub-grid modeling was first developed as a prototype in a PC UnTRIM model code (Casulli, 1999; Casulli and Zanolli, 2005; Casulli and Stelling, 2011). The first generation UnTRIM[1] solves the 3-D, time-dependent, nonlinear differential equations related to hydrostatic and nonhydrostatic, free-surface flow problems on an unstructured orthogonal grid (Casulli, 2009). Numerically, UnTRIM[1] is based on a semi-implicit finite volume/finite difference scheme and an Eulerian-Lagrangian explicit finite difference operator that allows unconditional stability. The second-generation sub-grid UnTRIM[2] model is coupled with a nonlinear wetting and drying solver, which can

resolve shoreline in the sub-grid due to the property of partial wetting and drying within a coarse base grid. In combining LIDAR data, bathymetry, and building structures database, Wang et al. (2014) and Loftis (2014) conducted the sub-grid UnTRIM^2 modeling to predict Hurricane Sandy (2012)-induced flooding in New York City. The results were reasonable and promising. Subsequently, the model was applied for simulating the 1936 Great flood in Washington, D.C. (Wang et al., 2015), also resulting in reasonable simulations compared with historical field measurements. However, the sub-grid UnTRIM^2 model is inherently a propriety software and the real-world inundation application is limited by: (1) the number of sub-grid it can allow; (2) the area of coverage the model domain can accommodate, and (3) the issue of reconstruction of tangential velocities.

In this dissertation, a new open-source inundation model ELCIRC-sub was developed based on a previously developed finite volume model: ELCIRC (Eulerian Lagrangian CIRCulation) model. ELCIRC-sub was upgraded with a new nonlinear solver based on the architecture of UnTRIM^2 but allows the MPI parallel computing algorithm to accommodate a much larger number of sub-grids and a larger watershed coverage. The boundary forcing can be provided by a large-scale model such as SCHISM and, when the domain size is adaptable, it will be more flexible and robust to choose an appropriate grid boundary for connecting with the large-scale model. Furthermore, the ELCIRC-sub reconstructs the tangential velocity for better conservation of mass, energy and potential velocity (Thuburn e al., 2009). It is to be shown later that ELCIRC-sub was successfully verified with a benchmark numeric wetting/drying test and realistically simulating the inundation in New York City during the 2012 Hurricane Sandy.

1.2. Research Objectives and Chapter Outline

There are two major objectives to this dissertation research.

On the storm surge model, I will apply large-scale storm tide SCHISM model, driven by NAM and ECMWF atmospheric forecast models and coupled with Wind Wave Model (WWMIII) to simulating Hurricane Sandy (2012) in the Greater New York City and Hurricane Irene (2011) in the lower Chesapeake Bay. The advantages of using SCHISM are three-fold: (1) It uses a finite element approach on the unstructured grid which resolves better the complicated shorelines and topography features and allows the fine grid resolution locally where it is needed; (2) It will be fully coupled with the Wind Wave Model (WWMIII) to account for the effects by wave-induced radiation stress and run in 3-D mode with a more realistic bottom boundary conditions, and variation of the vertical eddy viscosity; (3) Because of the usage of the Eulerian and Lagrangian scheme, the time step will be allowed to be larger without restricted by the CFL (Courant Friedrichs, Lewy) condition. These features plus the parallelized computing code using domain decomposition method on the HPC (High Performance Computing) clusters gives SCHISM a competitive edge over other models for its efficiency, robustness, and reliability. With the superior properties, it can make the real-time prediction a reality on a large-scale model domain west of the 60-degree West longitude, spanning the entire U.S. East and Gulf Coasts.

On the coastal inundation modeling, I will implement the sub-grid technique in conjunction with the LIDAR data and develop a nonlinear solver to more accurately calculate wetting and drying process in ELCIRC-sub model. Specifically, ELCIRC-sub will be upgraded to use domain decomposition method on a MPI parallel platform to

allow the model domain to be expanded with larger watersheds and accommodate more sub-grids. The enhancement will increase the flexibility and robustness of ELCIRC-sub inundation model, and its coupling with the SCHISM model.

In summary, the primary objective of my dissertation study is to develop effective, efficient, and reliable numerical models to predict large-scale storm surge along with the coastal inundation during storm events. The effort involves the development of a large-scale, 3-D, unstructured-grid cross-scale model to deal with storm surge from the ocean and a high-resolution street-level inundation model to simulate coastal flooding on land. The two related models will provide the capability to predict storm surge and coastal flooding in multiple regions along the U.S. East Coast and Gulf Coast.

The specific objectives include:

a. Applying a large-scale unstructured-grid storm surge model, driven by atmospheric models and coupled with wind wave model to ensure that storm tide driven by hurricanes from the ocean is accurately simulated in the coastal regions, where the results can be evaluated by observed water elevation and wind wave data.

b. Identifying and analyzing the sensitivity to different atmospheric forcing, the differences between 2-D and 3-D simulation, and the effects of wind wave.

c. Developing the high-resolution coastal inundation model using sub-gird techniques and nonlinear solver for wetting and drying processes in an expanded watershed coverage.

d. Visualizing street-level inundation results and evaluating sub-grid model performance by comparing with water gauges measurements and inundation databases.

The outline for the remainder of this dissertation is as follows:

Chapter 2: The methodology associated with the large-scale storm tide SCHISM model, and Wind Wave Model (WWMIII).

Chapter 3: Tidal and storm tide simulation results of the coupled wind wave and storm tide model in 2012 Hurricane Sandy and 2011 Hurricane Irene, and analysis of the effects of wind forcing, 3-D formulation, and wind wave.

Chapter 4: The methodology associated with the ELCIRC-sub inundation model, and numerical benchmark wetting/drying tests of the newly developed nonlinear solver.

Chapter 5: Detailed descriptions of ELCIRC-sub inundation model setup, model forcing and observations, and temporal and spatial analysis of model results in 2012 Hurricane Sandy.

Chapter 6: Discussion on large-scale storm tide model and sub-grid inundation model, and final conclusions of this dissertation.

CHAPTER 2. Development of Storm Surge Model - SCHISM and Wind Wave Model - WWMIII

2.1. Descriptions of SCHISM Model

The SCHISM (Semi-implicit Cross-scale Hydroscience Integrated System Model) is a 3-D baroclinic finite element model solving primitive shallow-water equation on unstructured horizontal and vertical grids. It is a derivative product built from the original SELFE v3.1dc model (Zhang and Baptista 2008) and, with new enhancements and upgrades, now is distributed with an open-source Apache v2 license. The SCHISM modelling system uses efficient semi-implicit Eulerian-Lagrangian scheme coupling with different system models and was designed for effectively simulating 3-D baroclinic circulation and associated processes in the estuaries and coastal waters across lake-river-shelf-ocean scales. The horizontal grid structure uses finite-element discretization comprised of mixed quadrilateral and triangular grids without limitations from the orthogonality of the grid property. The vertical grid structure uses hybrid vertical coordinates including spatially-varying LSC^2 (localized sigma coordinate system) vertical grid based on local water depths (Zhang et al., 2015). The entire SCHISM system was efficiently parallelized via domain decomposition and MPI (Message Passing Interface) and has been tested widely against standard ocean/coastal benchmarks. It has been applied to many estuarine systems around the globe, in the context of general circulation, tsunamis, storm-surge inundation, water quality, oil spills, sediment transport, coastal ecology, and wave-current interaction, as shown in Figure 1.

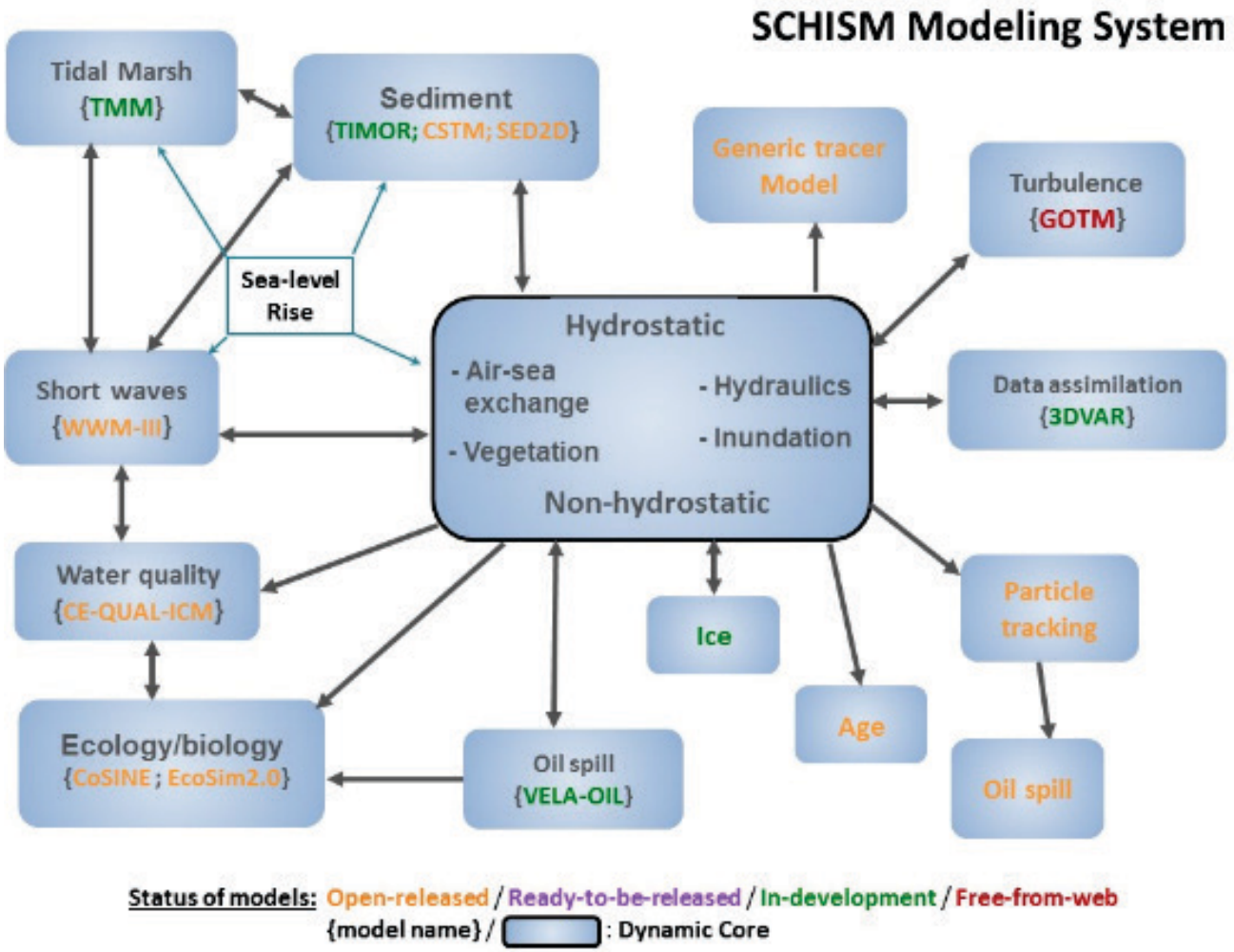

Figure 1: SCHISM modeling system. The modules that are linked by arrows can exchange internal data directly without going through the hydrodynamic core in the center.

2.1.1. Governing Equations and Numerical Methods

The SCHISM model solves the Reynolds-averaged Navier Stokes equation in its hydrostatic form and transport of salt and heat. The governing equations are solved for free surface elevation, water velocities, salinity, and temperature of the water (Zhang and Baptista, 2008; Zhang et al., 2016).

The momentum equation is shown as follows:

$$\frac{D\mathbf{u}}{Dt} = \frac{\partial}{\partial z}\left(\nu \frac{\partial \mathbf{u}}{\partial z}\right) - g\nabla\eta + \mathbf{F} \tag{1}$$

The continuity equation (in 3-D and 2-D depth-integrated forms) can be shown as:

$$\nabla \cdot \mathbf{u} + \frac{\partial w}{\partial z} = 0 \tag{2}$$

$$\frac{\partial \eta}{\partial t} + \nabla \cdot \int_{-h}^{\eta} \mathbf{u} dz = 0 \tag{3}$$

The transport equation is then represented as:

$$\frac{\partial C}{\partial t} + \nabla \cdot (\mathbf{u}C) = \frac{\partial}{\partial z}\left(\kappa \frac{\partial C}{\partial z}\right) + F_h \tag{4}$$

Where

∇	$(\frac{\partial}{\partial x}, \frac{\partial}{\partial y})$
D/Dt	material derivative
(x,y)	horizontal Cartesian coordinates
z	vertical coordinate, positive upward
t	time
$\eta(x, y, t)$	free-surface elevation
$h(x, y)$	bathymetric depth
$\mathbf{u}(x, y, z, t)$	horizontal velocity, with Cartesian components (u,v)
w	vertical velocity
$\boldsymbol{F}$	other forcing terms in momentum (baroclinic gradient $(-\frac{g}{\rho_0}\int_z^\eta \nabla\rho d\zeta)$, horizontal viscosity, Coriolis, earth tidal potential, atmospheric pressure, radiation stress)
g	acceleration of gravity, in $[ms^{-2}]$
C	tracer concentration (e.g., salinity, temperature, sediment etc.)
ν	vertical eddy viscosity, in $[m^2s^{-1}]$
κ	vertical eddy diffusivity, for tracers, in $[m^2s^{-1}]$
F_h	horizontal diffusion and mass sources/sinks

The differential system (Eq. 1–4) is closed with turbulence closure of the generic length-scale model of Umlauf and Burchard (2003), and proper initial and boundary conditions for each differential equation. The 3-D model domain is discretized into triangular elements in the horizontal and a series of vertical layers. The unknown variables are staggered on triangular prisms as shown in Figure 2.

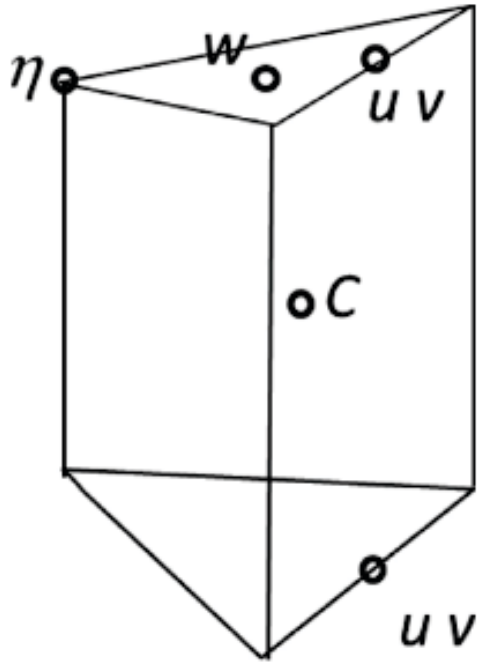

Figure 2. Staggering of variables in SCHISM. The elevation is defined at node (vertex) of a triangular element, horizontal velocity at side center and whole levels, vertical velocity at element centroid and whole level, and tracers at the prism center. The variable arrangement on a quad prism in SCHISM is similar. The top and bottom faces of the prism may not be horizontal, but the other 3 faces are always vertical.

The SCHISM model first solves the barotropic pressure gradient term in the momentum equation (Eq. (1)) with a semi-implicit schematization. The unknown velocities (defined at side centers) are first eliminated from the equations with the aid from the bottom boundary layer, resulting in an integral equation for the unknown elevations alone, which can be efficiently solved with a parallel solver (Jacobian Conjugate Gradient) (Zhang and Baptista, 2008). The time stepping is done using a 2nd-order Crank-Nicolson method, i.e., with the implicitness factor being 0.5 (in practice a value slightly larger than 0.5 is used for robustness).

The SCHISM then solves the momentum equation Eq. (1) along each vertical column at the center of each element side. A semi-implicit Galerkin finite-element method is used, with the pressure gradient and the vertical viscosity terms being handled implicitly with all other terms treated explicitly. Once all velocities at every element side are determined, the velocity at each node is computed by a weighted average of all surrounding sides evaluated by proper interpolation in the vertical. The velocity at each node is computed within each element from the three sides using a linear shape function as an averaging technique and is kept discontinuous between elements. This method can introduce parasitic oscillations, so a Shapiro filter is built into the model code as a smoothing function to suppress the static measurements (Shapiro, 1970).

A finite-volume approach is applied to the continuity equation, to solve for vertical velocity, as depicted in Figure 2. In this case, vertical velocity is solved from the bottom to the surface, in conjunction with the bottom boundary condition. Solution of the two-equations turbulence closure equations and update of the vertical grid including the

marking of wetting and drying nodes/sides/elements constitute the remaining operations in a time stepping loop.

Major features of SCHISM are highlighted as follows:

(1) Finite element/finite volume formulation.

(2) Unstructured mixed triangular/quadrangular grid in the horizontal dimension.

(3) Hybrid SZ coordinates or new LSC^2 in the vertical dimension.

(4) Polymorphism: a single grid can mimic 1D/2DV/2DH/3D configurations.

(5) Higher-order Eulerian-Lagrangian treatment of momentum advection.

(6) Semi-implicit time stepping (no mode splitting): no CFL stability constraints.

(7) Robust matrix solver including an implicit solver for transport equations.

(8) Natural treatment of wetting and drying processes for inundation studies.

(9) Mass conservative, monotone, higher-order transport solver: TVD^2; WENO.

(10) No bathymetry smoothing is required.

2.1.2. Initial and Boundary Conditions

The governing equations require the initial condition to be specified for unknown variables in each SCHISM model simulation. These include initial values for surface elevation, water velocities, salinity, and temperature, specified in “elev.ic”, “salt.ic” and “temp.ic” input files with values at each grid node, respectively. Inclusion of additional parameters and/or tracers requires providing initial conditions for each parameter and/or

tracer added. In this dissertation, since only the barotropic mode of SCHISM is utilized for storm tide simulations, the standard initial condition applied is the zero-motion condition with a model "spin up/warm up" period prior to the storm event to account for tidal propagation in regions with relatively complex shoreline geometry. The tidal potential function and tidal elevation are specified at the open boundary initiated by a hyperbolic tangent function to simulate a series of tidal harmonic constituents with a typical duration of 2 to 3 days for a large-scale domain, such as those used in modeling Hurricane Sandy (2012) and Hurricane Irene (2011).

Surface boundary condition is applied mainly by surface wind stress over the water at the air-sea interface. A variety of methods are used to parameterize surface wind fields (Pond and Pickard, 1998; Zeng et al., 1998). SCHISM uses outputs from atmospheric models to drive storm surge simulations. Surface stress is evaluated by:

$$(\tau_{W_x}, \tau_{W_y}) = \rho_a C_{ds} \left|\vec{W}\right| (W_x, W_y) \quad (5)$$

Where:

ρ_a: air density (kg/m^3);

C_{ds}: wind drag coefficient;

(W_x, W_y): x/y-direction wind velocity at 10 m above the mean sea surface;

$\left|\vec{W}\right|$: wind magnitude (m/s).

The drag coefficient is usually set via the formula of Garrat (1977) which is a linear function of wind magnitude and has upper/lower limits. Details of surface wind forcing for large-scale storm tide SCHISM model will be explained in Chapter 3.

At the bottom boundary, the 3-D SCHISM model is balanced between bottom friction stress and internal stress. Bottom stress is usually defined as:

$$(\tau_{b_x}, \tau_{b_y}) = \rho_0 C_{db} \left|\overrightarrow{U_b}\right| (u_b, v_b) \quad (6)$$

Where:

ρ_0: water density (kg/m^3);

C_{db}: bottom drag coefficient;

(u_b, v_b): u/v-direction near bottom velocity;

$\left|\overrightarrow{U_b}\right|$: bottom velocity magnitude (m/s).

Accurate parameterization of bottom drag coefficient is necessary to effectively simulate bottom friction stress, and a spatially varying coefficient is often needed. Manning's coefficient, n, as an empirically derived value, is used in 2-D depth-averaged long wave formulation. In this dissertation, both 2-D and 3-D models use the same spatially-varying Manning's n value to convert to the C_{db} values. It should be noted that there is an alternative approach for 3-D models by specifying bottom drag coefficient using bottom roughness and the equivalent Manning's n formulation (see Appendix 3).

Open ocean boundary in SCHISM model usually consists of elevation, velocity, river flux, salinity, and temperature which need to be specified at the surrounding boundaries of the model domain where the time series values are required. For large-scale storm tide simulation, tidal elevation at the deep ocean boundary (at 60-degree West meridian of longitude) were specified using eight dominant tidal constituents (M_2, N_2, S_2, K_2, O_1 P_1, K_1, and Q_1). This is sufficient because the domain is so large that the boundary is normally unaffected by the hurricanes.

2.2. Descriptions of Wind Wave Model (WWMIII)

The Wind Wave Model (WWMIII) is a third-generation wave model developed by Roland (2009, 2012), which is an unstructured grid spectral wave model, incorporating most existing source terms for wind input and dissipation. WWMIII is based on the source code by Hsu et al. (2005) and was revised further in terms of numerical schemes and physics (Roland, 2009, 2012).

2.2.1. Governing Equations and Numerical Methods

The governing equation of WWMIII is mainly the Wave Action Equation (hereafter WAE). It includes growth, decay, advection, and refraction of wind waves due to varying depths and currents computed by the hydrodynamic model. It can be written for Cartesian coordinates as follows (e.g. Komen et al., 1994):

$$\frac{\partial}{\partial t}N + \nabla_X\left(\dot{X}N\right) + \frac{\partial}{\partial \sigma}\left(\dot{\theta}N\right) + \frac{\partial}{\partial \sigma}\left(\dot{\sigma}N\right) = S_{tot} \qquad (7)$$

where the Wave Action N, which is invariant in slowly varying media (Bretherton and Garrett, 1968), and is expressed as:

$$N_{(t,X,\sigma,\theta)} = \frac{E_{(t,X,\sigma,\theta)}}{\sigma} \qquad (8)$$

with E being the variance density of the sea level elevations, σ the relative wave frequency, and θ the wave direction. The advection velocities in the different phase spaces are given following the Geometric Optics Approximation (e.g., Keller, 1958).

$$\dot{X} = c_X = \frac{dX}{dt} = \frac{d\omega}{dk} = c_g + U_{A(k)} \quad (9)$$

$$\dot{\theta} = c_\theta = \frac{1}{k}\frac{\partial \sigma}{\partial d}\frac{\partial d}{\partial m} + k \cdot \frac{\partial U_{A(k)}}{\partial s} \quad (10)$$

$$\dot{\sigma} = c_\sigma = \frac{\partial \sigma}{\partial d}\left(\frac{\partial d}{\partial t} + U_A \cdot \nabla_X d\right) - c_g k \frac{\partial U_{A(k)}}{\partial s} \quad (11)$$

Here s represents the coordinate along the wave propagation direction and m represents that perpendicular to it. X is the Cartesian coordinate vector (x, y) in the geographical space, d is the water depth obtained from SCHISM, k is the wave number vector, c_g the group velocity and ∇_X is the gradient operator in the geographical space. The group velocity is calculated from the linear dispersion relation. The effective advection velocity $U_{A(k)}$ depends in general on the wave number vector of each wave component (Andrews and McIntyre, 1978a, b). In the previous applications, this was approximated by the surface current. In Eq. (7), the terms on the left-hand side represent, respectively, the change of wave action in time, the propagation of wave action in geographical space, depth-, and current-induced refraction (with propagation velocity or turning rate c_θ), and the shifting of σ due to variations in mean current and depth (with propagation velocity or shifting rate c_σ). The wave diffraction effect is introduced into the WAE through the correction of wave number and propagation velocities using a diffraction-corrected parameter (Holthuijsen et al., 2003).

S_{tot} is the source term including the energy input due to wind S_{in}, the nonlinear interaction in deep and shallow water (S_{nl4} and S_{nl3}), the energy dissipation in deep and

shallow water due to white capping and wave-breaking (S_{ds} and S_{br}), and the energy dissipation due to bottom friction S_{bf}; the source term can be presented as:

$$\frac{DN}{Dt} = S_{total} = S_{in} + S_{nl4} + S_{ds} + S_{nl3} + S_{br} + S_{bf} \quad (12)$$

WWMIII solves the WAE using the fractional step method as described by Yanenko (1971). The fractional step method allows the splitting of the time-dependent four-dimensional problems in well-defined parts for which dedicated numerical methods can be used to have a well-defined consistent and convergent numerical method (e.g. Tolman, 1992). As an alternative and innovative method to the well-known family of finite volume schemes or finite element schemes, the family of Residual Distribution Schemes (RD schemes, also known as "fluctuation splitting schemes", (Abgrall, 2006)) has been implemented in the present WWMIII model.

The RD schemes are a new family of numerical schemes that borrow ideas from the finite element (FE) and the finite volume (FV) framework. As a result, compact schemes and accurate solutions that are carefully designed to obey most important constraints, such as the conservation property, positivity, and linear preservation (2nd-order in smooth flow) and that can be well parallelized, can be achieved. The source terms are integrated in three separate fraction steps according to their time scales or nonlinearity. In the 1st step we integrate the dissipative terms in shallow water such as wave-breaking and bottom friction and this is done without the necessity of an action limiter using a TVD Runge-Kutta scheme of 3rd order (Gottlieb and Shu, 1998). Then, the triad interaction source terms are integrated using a dynamic approach as suggested by Tolman (1992). Lastly, we integrate the deep-water source terms using the well-known semi-implicit approach by Hersbach and Janssen (1999).

2.2.2. Wave-Current Interaction and Coupling WWMIII with SCHISM

The wave-current interaction includes the following three aspects: (1) wave-induced radiation stress based on the formulation of Longuet-Higgins and Stewart (1964); (2) wave-enhanced surface stress as well as turbulent mixing (e.g., Craig and Banner, 1994); (3) wave-enhanced bottom stress (Grant and Madsen, 1979).

a. Wave-induced radiation stress

Waves travelling in a specific direction generate radiation stresses, and this term may be defined as the excess flow of momentum due to the presence of the waves. Wave transformation generates radiation stress gradients that drive set-up and currents. This will be analyzed in detail in Section 3.2.3 and Section 3.3.3. The radiation stress is introduced into the explicit term F in the momentum equation (Eq. (1)) of SCHISM model. The finite–element formulation is applied to this additional radiation stress term when the wave-induced stresses are considered in the model run. The radiation stress (a net momentum of flux produced by wave transformation in shallow water) can be parameterized with different formulations (Mellor, 2003, 2005, 2008, 2011a, b; Xia et al., 2004). The wave-induced stresses (gradient of the radiation stress) Rs according to Longuet-Higgins and Stewart (1964) in the x- and y-directions can be estimated in the linear form, accounting for the mean flow momentum (Mastenbroek et al.,1993):

$$\begin{Bmatrix} R_s = (R_{sx}, R_{sy}) \\ R_{sx} = -\frac{1}{\rho_0 H}\frac{\partial S_{xx}}{\partial x} - \frac{1}{\rho_0 H}\frac{\partial S_{xy}}{\partial y} \\ R_{sy} = -\frac{1}{\rho_0 H}\frac{\partial S_{yy}}{\partial y} - \frac{1}{\rho_0 H}\frac{\partial S_{xy}}{\partial x} \end{Bmatrix} \quad (13)$$

with Sxx, Sxy, Syy being the components of the radiation stress tensor, where H is the total water depth. Note that the stress is uniform in the vertical dimension under this formulation. The radiation stress gradients have large values in regions with significant wave breaking. Wave setup is the super elevation of mean water level owing to the presence of breaking incident waves.

b. Wave-enhanced surface stress

When considering the effect of wave-enhanced surface stress, the total surface stress is estimated based on the actual sea state using the theory of Janssen (1991). The total stress can be passed to the current model (SCHISM) to account for the surface stress and the enhanced mixing due to the wave-breaking is expounded upon in Craig and Banner (1994). The wave decay due to the wave dissipation at the cost of white capping and depth-induced breaking also results in transfer of momentum from waves into the currents that can be parameterized using effective shear stress.

c. Wave-enhanced bottom stress

In shallow water regions, the wave-induced bottom stress in the wave bottom boundary layer can affect sediment transport. The formulation of wave-enhanced bottom stress used was originally proposed by Grant and Madsen (1979) and later modified by Mathisen and Madsen (1996). When the effects of wave-enhanced bottom stress are considered, the original bottom roughness will be replaced with an apparent roughness, which can be different from the original bottom roughness (Zhang et al., 2004).

Among these three processes that represent wave effects on water elevation, the radiation stress generally plays a more important role in coastal storm surge than the other two effects (Huang et al., 2010; Sheng et al., 2010). So, in this dissertation, I focus

on the radiation stress in evaluating the effects of wind wave in a coastal storm surge application.

d. Model coupling

Computing wind waves directly in a storm surge model can be quite challenging and computationally expensive. However, recent development of wave-current modeling enables improved representation of wave-related physical processes through two-way information exchange between wave and circulation models (referred to as coupled models).

In this dissertation, WWMIII is coupled with SCHISM at the source code level by parallelizing it via the same domain decomposition scheme as that used by SCHISM. The usage of the same sub-domains in the two models can eliminate the need for interpolation and simplify the exchange of information between current and wave models, resulting in better efficiency. The WWMIII is then recast as a subroutine inside SCHISM. Due to different time stepping schemes used in SCHISM and WWMIII, the time steps used in the two models are kept different to take advantage of each model's efficiency, and information exchange between the two models occurs at a pre-specified interval. During the information exchange, the wind, sea surface elevation, wet/dry flags, and currents are passed from SCHISM to WWMIII, and the calculated radiation stress is returned to SCHISM. The radiation stress is estimated as given in Roland et al. (2012) based on the directional spectra itself and is counted in momentum equations in the main SCHISM model. The coupling of SCHISM with WWMIII has proved to be efficient and robust by Roland et al. (2012) in many challenging benchmarks. The initial and boundary conditions of WWMIII are explained in Section 3.2.1.

CHAPTER 3. Applications of Coupled Wind Wave and 3-D Barotropic Storm Tide Model

3.1. Model Domain and Grid

The high-resolution large-scale storm tide SCHISM model makes use of a large horizontal grid containing 313,407 nodes and 592,827 elements for simulation with an open ocean boundary aligning with the 60-degree West longitude (Figure 3). This covers the entire U.S. East Coast, Caribbean Sea, as well as the Gulf of Mexico. The model grid includes 294 open boundary nodes where elevation forcing can be applied with tidal forcings. The boundary is sufficiently far from land that it is normally not affected by approaching hurricanes that make landfall to the U.S. Coasts. The high-resolution, large-scale storm surge model grid is flexible and can be locally refined by including detailed localized information in specified coastal regions, e.g. New York Harbor (Hurricane Sandy simulation) and Chesapeake Bay (Hurricane Irene simulation). The grid resolution ranges from approximately 20 km in the Atlantic Ocean near open boundary to 20 - 30 m (e.g., in the lower Chesapeake Bay and Hudson River near New York City).

The bathymetry of the open ocean and continental shelf in this mesh are interpolated from NOAA's bathymetric sounding database, the Digital Nautical Charts database, ETOPO1 1-minute gridded elevations/bathymetry for the world database (NOAA National Geophysical Data Center, 1999, 2011; National Ocean Service, 1997; U.S. Department of Defense, 1999). In coastal regions, for example, New York Harbor, NOAA Coastal Relief Model (~90 m resolution) (NOAA NGDC, 2011) and NOAA Bathymetric Survey Data (10-20 m resolution) (National Ocean Service, 2006) are used; In the Chesapeake Bay, detailed bathymetry in 10-m resolution from FEMA Region III (Figure 4) is used. The model grid also permits specification of LSC^2 vertical grid in the 3-D mode which uses different numbers of layers from deep ocean (>5000 m, e.g. 36

layers) all the way to shallow rivers (<2 m, e.g. 6 layers). The master grid of LSC^2 provides a clear view of the depth-varying number of vertical layers (Figure 5). In this way it has been proven that both computational efficiency and model accuracy are preserved (Zhang et al., 2015).

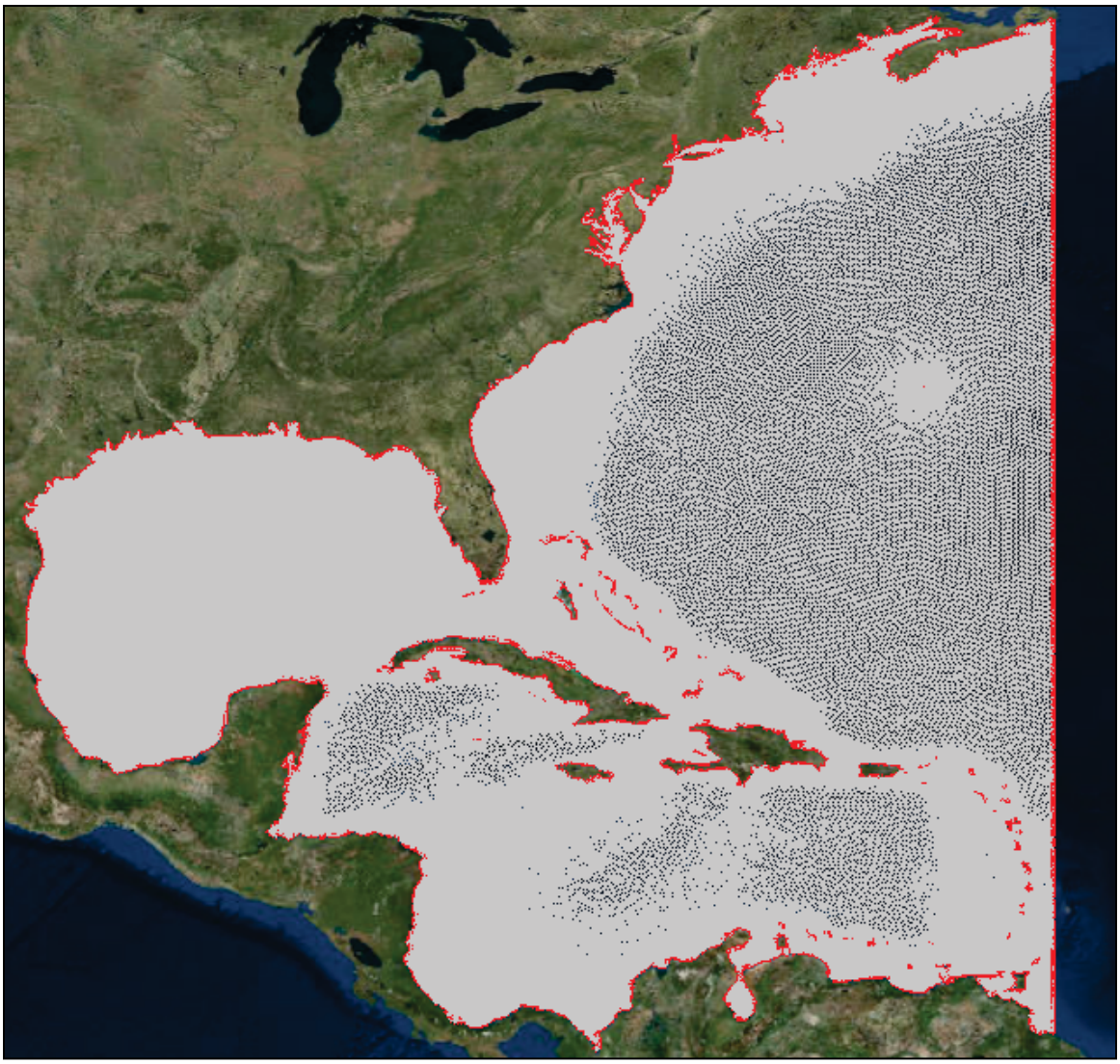

Figure 3: High-resolution large-scale storm surge model domain grid with an ocean boundary aligning with the 60-degree West longitude (grid elements shown in grey color) which covers entire U.S. East and Gulf Coasts.

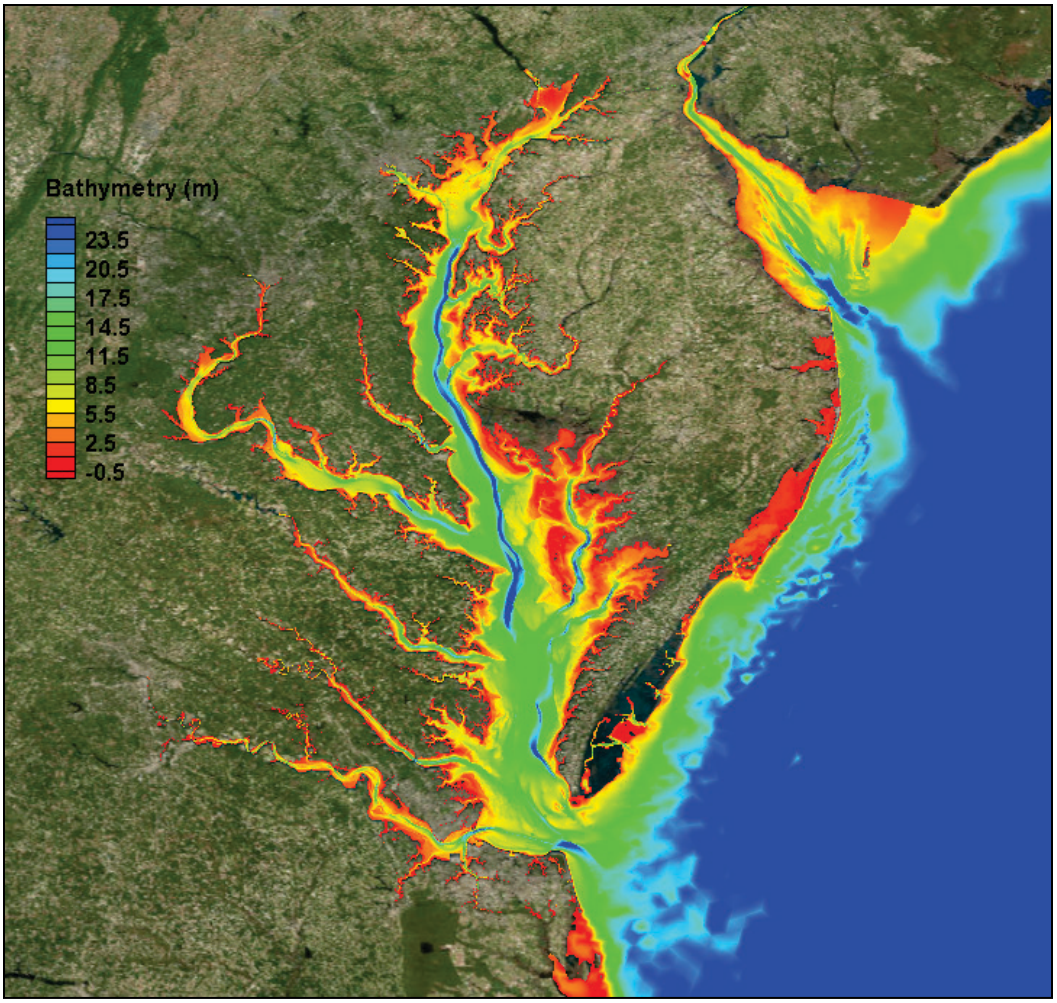

Figure 4: Detailed 10-m-resolution FEMA Region III bathymetry information inside Chesapeake Bay, Delaware Bay, and part of Atlantic Ocean.

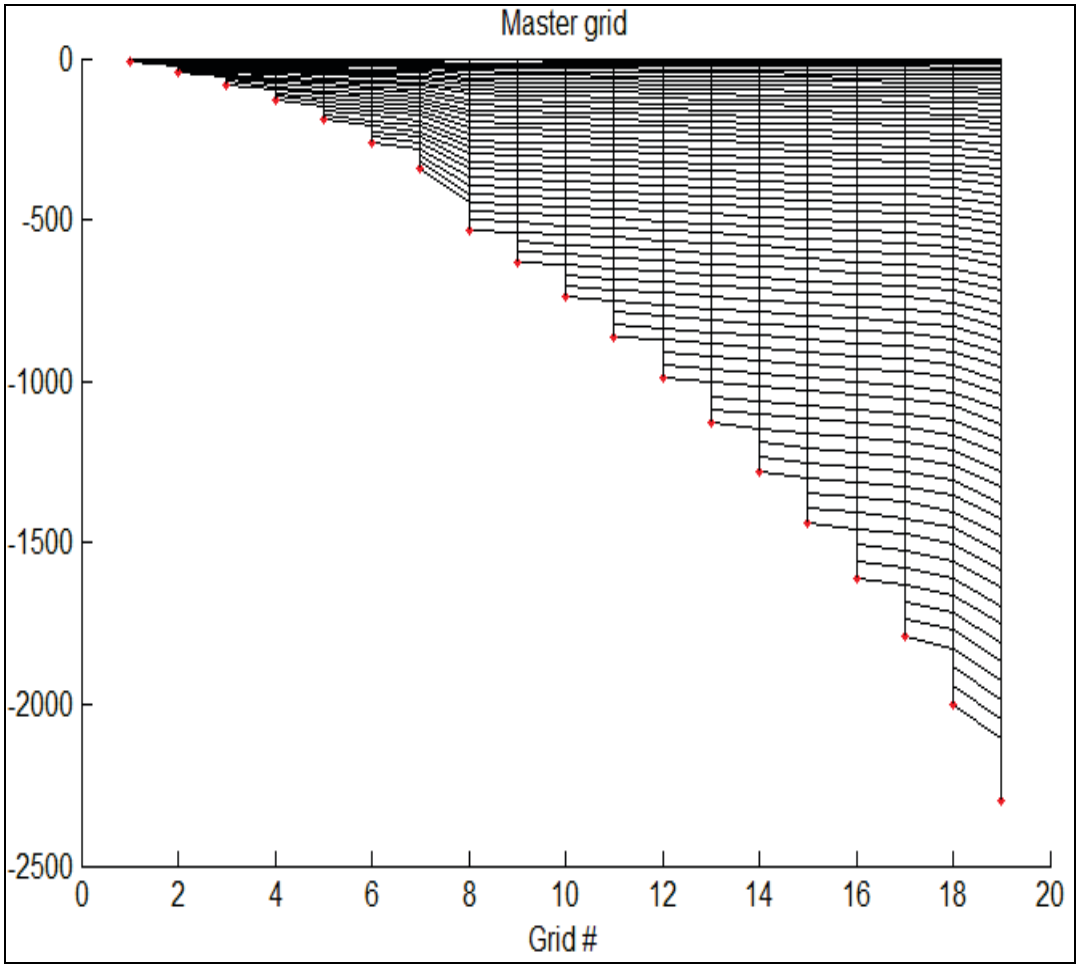

Figure 5: Master grid of LSC^2 vertical grid in SCHISM. Y-axis shows depths. Black lines represent depth-varying vertical layers.

3.2. Hurricane Sandy (2012) in the Greater New York City

On October 22, 2012, Hurricane Sandy started to form in the Caribbean Sea, and intensified as it moved northward to the U.S. East Coast. The storm turned into a Category 3 Hurricane over the mid-Atlantic Bight just before sharply turning to the northwest on October 29th (Figure 6). ECMWF was the earliest of various forecast models to predict this abrupt veering of wind direction (Figure 7). The unique shift in storm track was largely due to a large-scale wind flow pattern favoring an upper-level block over Greenland and a mid-level atmospheric trough coming from the U.S. Southeast. Consequently, Hurricane Sandy made landfall just north of Atlantic City near Brigantine, NJ, as a Category 1 Hurricane on October 30, 2012, at approximately 00:30 UTC.

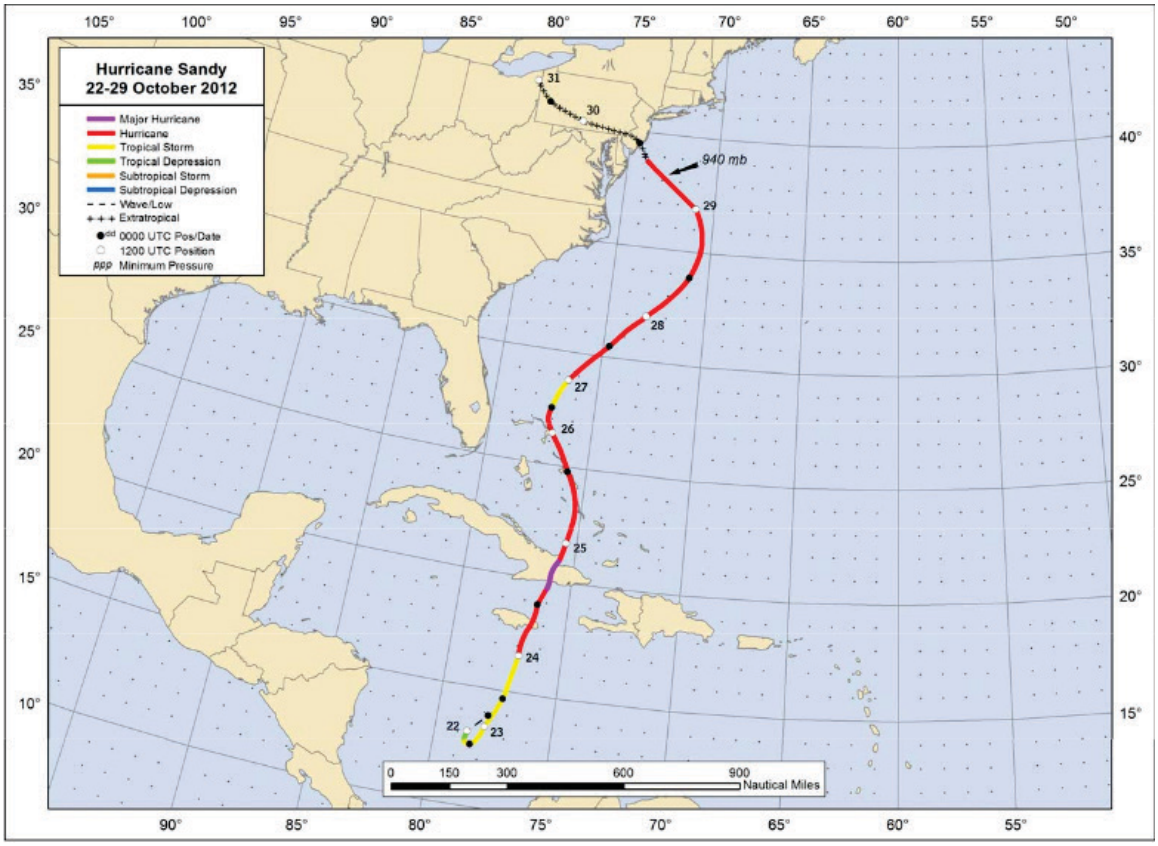

Figure 6: Hurricane Sandy (2012) Track reported by NOAA National Hurricane Center.

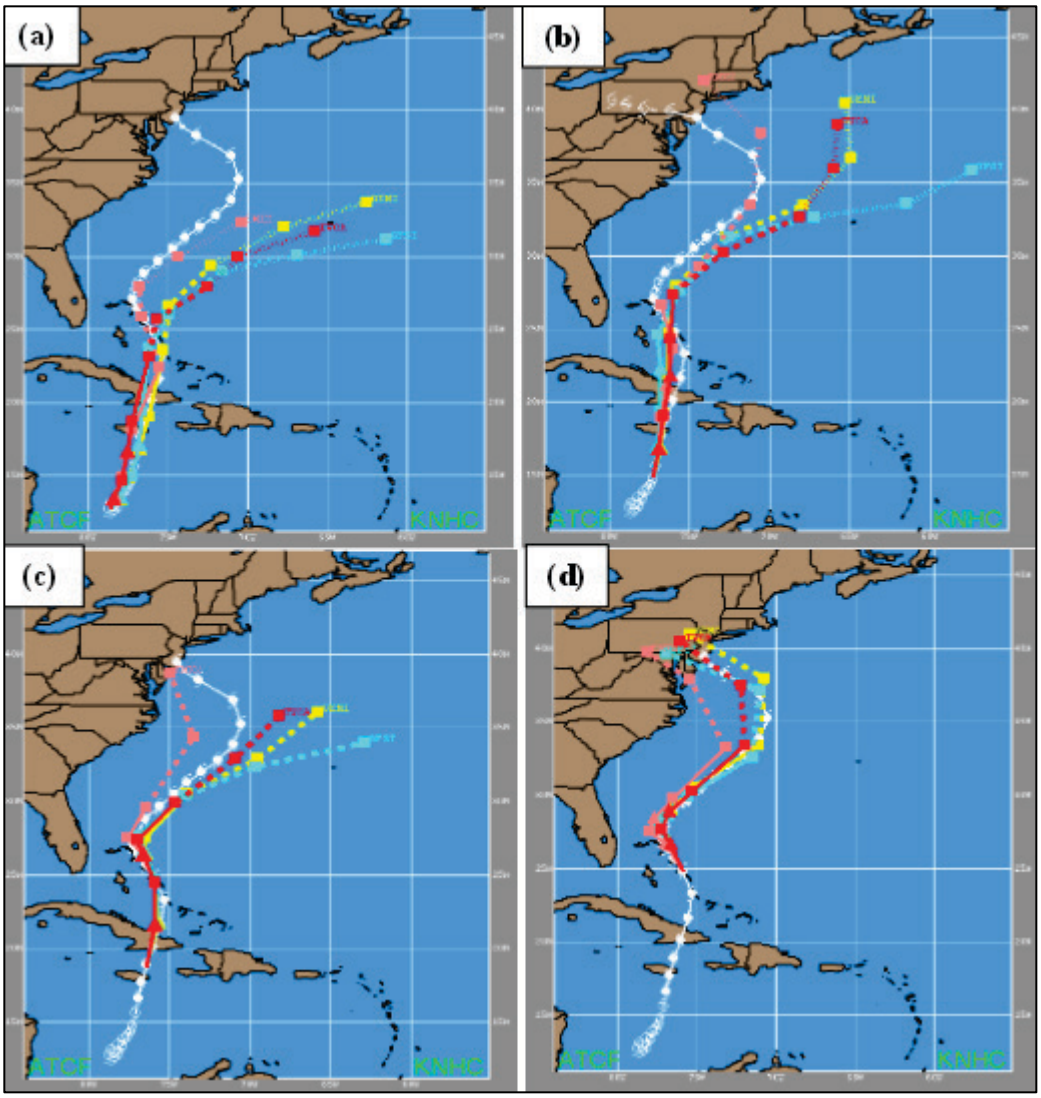

Figure 7: Model forecast tracks at 0000 UTC 23 October 2012 (a), 0000 UTC 24 October 2012 (b), 0000 UTC October 25 2012 (c), and 0000 UTC 26 October 2012 (d). Solid color lines are for forecasts through 72 hours, while dashed lines are from 72-120 hours, and dotted lines represent the 120-168 hour forecasts (top panels only). The official track is in white, the European Centre for Medium Range Weather Forecasts (ECMWF) is in coral, the Global Forecast System (GFS) is in cyan, the GFS ensemble is in yellow, and the Track Variable Consensus Aids (TVCA) model consensus is in red.

Hurricane Sandy caused enormous damage to residential properties, community infrastructure, and human life in the U.S. East Coast. The storm surge created some of the most devastating impacts, including flooding in New York City's subway tunnels, LaGuardia and Kennedy airports, damage to the New Jersey transit system, and the coastal seashore (NOAA, 2012). An abnormal storm tide with disastrous water levels occurred in New Jersey, New York City, and a portion of the Long Island Sound. The NOAA tide gauges records show peak water levels at The Battery, NY, Bergen Point, NY, Sandy Hook, NJ, and Bridgeport, CT, at 2.74, 2.90, 2.44, and 1.77 m, (or 9.0, 9.53, 8.01, and 5.82 feet) above mean higher high water, respectively (NOAA, 2012). The storm tide triggered significant flooding in New York in the lower Manhattan, the Hudson River Valley, and the East River, with some of the most catastrophic flooding being observed along Staten Island and to the south along the New Jersey coast.

Storm surge can be particularly damaging when it occurs simultaneously with a high tide. At Kings Point, near the head of the Long Island Sound, the highest storm tide was observed where the peak surge occurred concurrently with a tidal trough (Figure 8). The observed storm tide could have been at least 2 m higher at Kings Point if the storm surge occurred during the high tide.

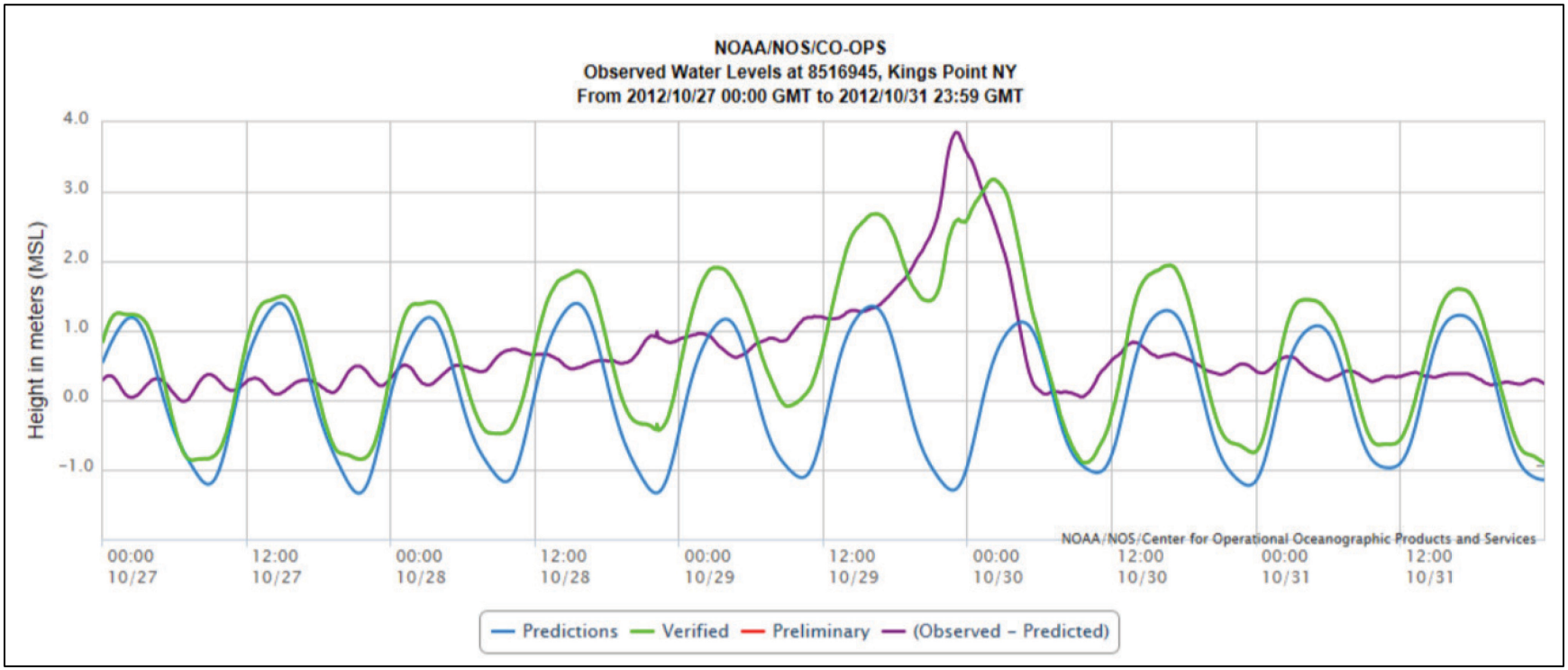

Figure 8: Observed water level at Kings Point, NY during Hurricane Sandy.

Since the hurricane moved along the offshore of the U.S. East Coast from South Florida to New Jersey, this coastline was impacted by remote winds before landfall. According to NOAA observations, Duck, NC, Chesapeake Bay Bridge Tunnel (CBBT), VA, and Cape May, NJ experienced the long-wave fore-runner of Hurricane Sandy that already set water up around October 25, which was 5 days before landfall. In order to simulate this fore-runner of Sandy, a simulation period of 21 days was specified instead of the typical 3 or 4 days.

All storm tide runs started on October 10, 2012 00:00 UTC, the same start-time of wind and pressure fields, and all simulations ended on October 31, 2012 00:00 UTC. The simulations were conducted by 200 computational cores via Sciclone HPC cluster at The College of William and Mary. The four simulations using current-only model all had more than 120 times real-time speedup while the other four coupled model runs had approximately 80 times real-time speedup. Section 3.2.3 lists the details of each simulation's setup.

3.2.1. Model Forcing and Available Observation

Tidal elevations are forced along the 294 nodes at the Atlantic open-ocean boundary using eight major astronomical tidal constituents including the semidiurnal M_2, N_2, S_2 and K_2 constituents along with the diurnal O_1, K_1, Q_1 and P_1 constituents using data from the ADCIRC Tidal Databases (ADCIRC, 2001). The tidal potential constants, and Earth elasticity factors, which reduce the magnitude of the tidal potential forcing due to the earth tides are accounted for in the SCHISM model such that the nodal factor and

equilibrium argument for boundary and interior domain forcing tidal constituents are based on the starting time of the simulation.

The atmospheric model outputs, 10 m u/v wind and mean sea-level pressure, are applied as the model's surface forcings. These atmospheric model data outputs were processed into NetCDF files for use in conjunction with the 'sflux' input format (http://ccrm.vims.edu/w/index.php/Atmospheric_forcing). The atmospheric products used include:

(1) 5-km resolution, 3-hourly NAM-NEST product for Hurricane Sandy, 10/10 00:00 UTC to 10/31 00:00 UTC, 2012: 10 m u/v wind in m/s; mean sea level pressure in Pa.

(2) 12-km resolution, 3-hourly ECMWF T1279 product for Hurricane Sandy (10/10 00:00 UTC to 10/31 00:00 UTC, 2012): 10 m u/v wind in m/s; mean sea level pressure in Pa.

The open boundary forcing for wind wave model - WWMIII was not required as the strong wave-generating storms by hurricane winds were completely contained within the model domain during the hurricane events simulated. If wave-generating storms extended beyond the model domain, then wave conditions at the open ocean boundary will need to be included by interpolating from other larger-domain wave model results. Initial condition is set as default: no wave exists in the model domain at the beginning of a simulation.

For the Hurricane Sandy simulation, the observations used were from:

a) 9 NOAA tide gauges along the U.S. East Coast and in Long Island Sound;

b) 2 NBDC observation buoy stations in New York / New Jersey Bight.

The 9 NOAA tidal gauges were used for comparing with modeled storm tide elevation relative to Mean Sea Level (MSL). The 2 NDBC buoys (NDBC, 2012) were utilized for comparisons with modeled significant wave height, and peak wave period. The locations and detailed information of these stations are shown in Figures 9-10 and Table 1.

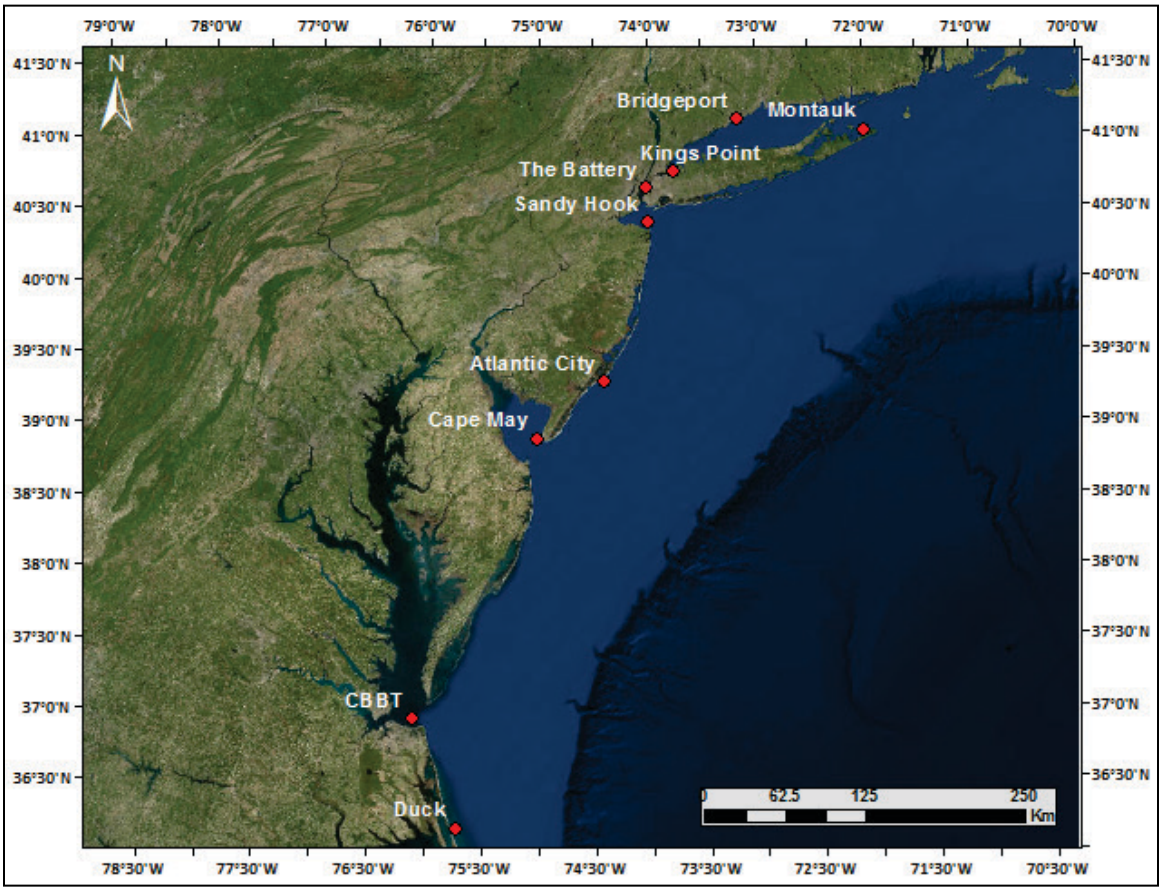

Figure 9: Locations of 9 NOAA tidal gauges (red dots) used in water elevation comparisons.

Figure 10: Locations of 2 NDBC observation buoys (blue dots labeled as '44065' and '44025') used in wave comparisons.

Table 1: Detailed information for NOAA tidal gauges and NDBC buoys.

Station ID	Station Name	Latitude	Longitude	Observation
NOAA-8510560	Montauk, NY	41.0687	-71.9810	Water level
NOAA-8467150	Bridgeport, CT	41.1620	-73.1005	Water level
NOAA-8516945	Kings Point, NY	40.8291	-73.7642	Water level
NOAA-8518750	The Battery, NY	40.6957	-74.0210	Water level
NOAA-8531680	Sandy Hook, NJ	40.4597	-74.0216	Water level
NOAA-8534720	Atlantic City, NJ	39.3294	-74.4010	Water level
NOAA-8536110	Cape May, NJ	38.9443	-75.0174	Water level
NOAA-8638863	CBBT, VA	36.9709	-76.1056	Water level
NOAA-8651370	Duck, NC	36.1987	-75.7366	Water level
NDBC-44065	44065	40.3650	-73.6984	Wave data
NDBC-44025	44025	40.2889	-73.1710	Wave data

3.2.2. Tidal and Storm Tide Hindcast in New York City and the Mid-Atlantic Bight

Tidal calibration and harmonic analysis were conducted to ensure that SCHISM properly modeled long-wave propagation along the U.S. East Coast and inside New York Bay. With only tidal sinusoidal motion at the open ocean boundary, the large-scale SCHISM model was run without any wind forcing. Eight harmonic tidal constituents (M_2, N_2, S_2, K_2, O_1, P_1, K_1, and Q_1) were applied at 294 nodes at the 60-degree West

longitude boundary based on the ADCIRC Tidal Data Base (ADCIRC, 2001). Both 2-D and 3-D barotropic tidal runs were conducted and the results were almost identical. To keep this section brief, results from the tidal runs are presented in Appendix 2. The tidal simulation spanned 90 days from September 1st 00:00 UTC through November 30th 00:00 UTC, 2012. The bottom friction coefficient is derived from Manning's formulation and is the same value for both 2-D and 3-D models. A standard manning of n=0.025 was applied in most of the areas except in (1) Hudson River, n=0.010; and (2) East River, n=0.045. These values were consistent with previous studies in the New York Bight (Blumberg et al., 1999). Additionally, nodal factor and equilibrium arguments were also accounted for in the 'bctides.in' input file. 9 NOAA tidal gauges were utilized to verify model accuracy. Analysis tables of tidal amplitude and tidal phase between modeled tide and NOAA predicted tide for the 5 major harmonic constituents show excellent results (see Appendix 2 (1)) that SCHISM model accurately simulates tidal propagation across Western Atlantic to the U.S. Eastern Seaboard and embayments.

Modeled storm tide results were compared with NOAA tidal gauge data at locations shown in Figure 9. The 3-D SCHISM model performed better than our previous 2-D model (Liu et al., 2014; Wang et al., 2014). At all stations, the differences between the coupled wave-current model and current-only emerge only after October 29 when Sandy with strong wind approached near the U.S. East Coast, and the major differences only occurred in New York Bay (explained in Section 3.2.3.3). The SCHISM coupled with WWMIII simulated the maximum storm tide with an error less than 8 cm at The Battery, NY, which is located at the tip of the lower Manhattan. At this station and Sandy Hook, NY, SCHISM coupled with WWMIII increases the maximum storm tide level by 0.18 -

0.2 m (5-6 % of total water level above MSL) over SCHISM without WWMIII. The coupled wave-current 3-D model using ECMWF wind forcing has the best agreement with observation based on the calculated correlation coefficient (R^2), Root-Mean-Square Error (RMSE), and Mean Absolute Error (MAE) values (Table 2). The average RMSE across all stations is less than 13 cm.

Table 2: Statistical evaluation of SCHISM modeled storm tide from 3D-W-E simulation for 9 NOAA stations.

Stations	R^2	RMSE (m)	MAE (m)
Montauk, NY	0.959	0.091	0.074
Bridgeport, CT	0.976	0.142	0.107
Kings Point, NY	0.964	0.199	0.141
The Battery, NY	0.961	0.155	0.110
Sandy Hook, NJ	0.972	0.128	0.102
Atlantic City, NJ	0.955	0.175	0.128
Cape May, NJ	0.973	0.105	0.090
CBBT, VA	0.926	0.142	0.111
Duck, NC	0.975	0.080	0.063

Figures 11-13 present the overall best simulation results at 9 stations which have been grouped into: 1) Long Island Sound: Montauk, Bridgeport, Kings Point; 2) New York and New Jersey: The Battery (lower Manhattan), Sandy Hook, Atlantic City; 3) Southeast Coast: Cape May, CBBT, Duck. The surge traveled from Montauk westward toward Kings Point near the western end of Long Island Sound. R^2 at those stations are all above 0.95, and the averages of RMSE and MAE are 14 cm and 10 cm, respectively. Phase discrepancy in the model results at the Kings Point between 00:00 UTC October 30 and 12:00 UTC October 30 suggests that some local effects may contribute to the phase shift during the peak surge, but this model was unable to catch it perfectly based on the

current resolution of the bathymetry and atmospheric forcing. In Chapter 5, a newly developed high-resolution sub-grid inundation ELCIRC-sub model was applied in this region and the model was able to simulate even more accurately for this maximum surge at Kings Point, NY. The results from stations in New York City, New York Lower Bay and New Jersey coast are also very reasonable. R^2 at Sandy Hook and The Battery are both above 0.96, the averages of RMSE and MAE are 14 cm and 10 cm, respectively. The stations along the Southeast coast first experienced remote wind effects of the hurricane so they had maximum surge coming about 12 hours before other northern stations. The model also performs well there with R^2 above 0.92, and RMSE and MAE averages of 11 cm and 9 cm, respectively. In general, the large-scale coupled wind wave and 3-D storm surge SCHISM model performed very well during this severe hurricane event with better results than many other published studies, especially over the location of the most concern, New York City.

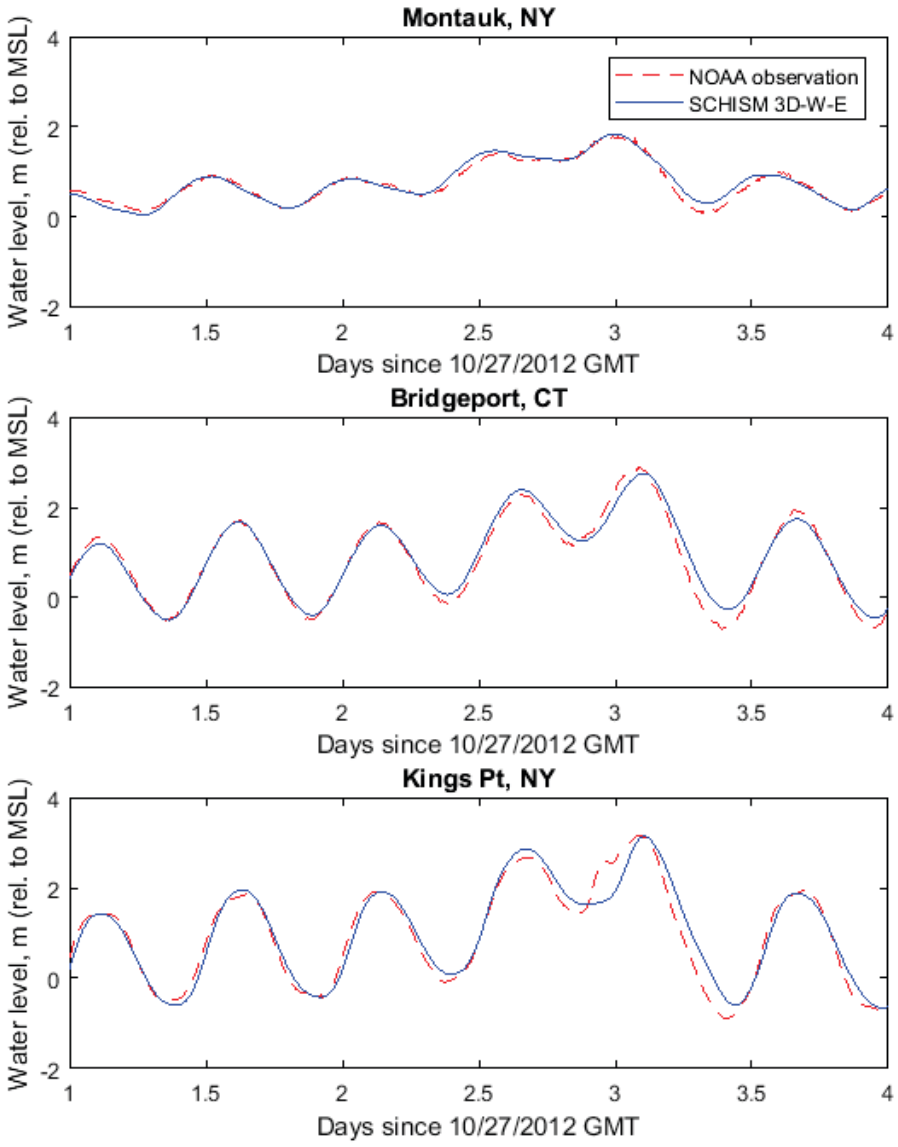

Figure 11: Time series of comparisons of NOAA observation and SCHISM modeled storm tide (3D-W-E: 3-D coupled wind wave model using ECMWF forcing) results for stations in Long Island Sound.

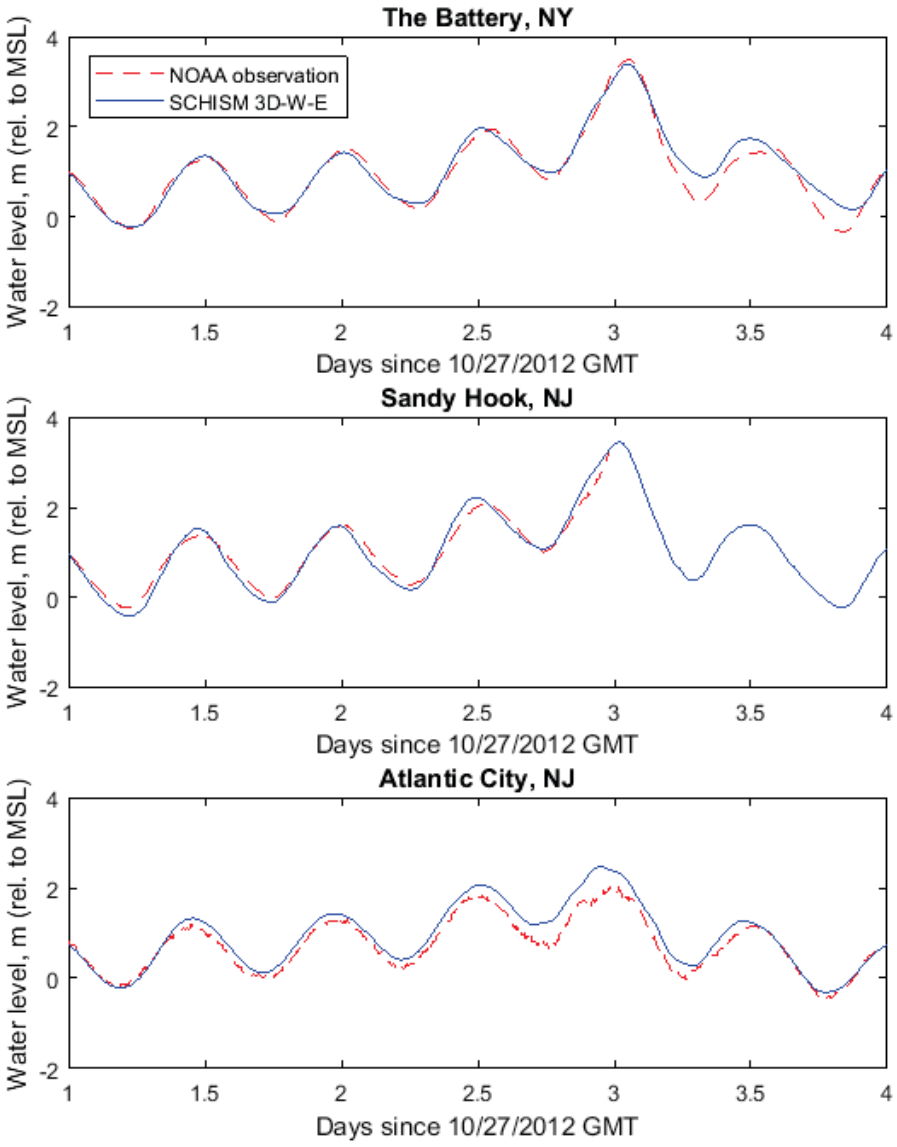

Figure 12: Time series of comparisons of NOAA observation and SCHISM modeled storm tide (3D-W-E: 3-D coupled wind wave model using ECMWF forcing) results for stations near New York Harbor and Atlantic City, NJ. Note there was discontinuity in NOAA observations at Sandy Hook.

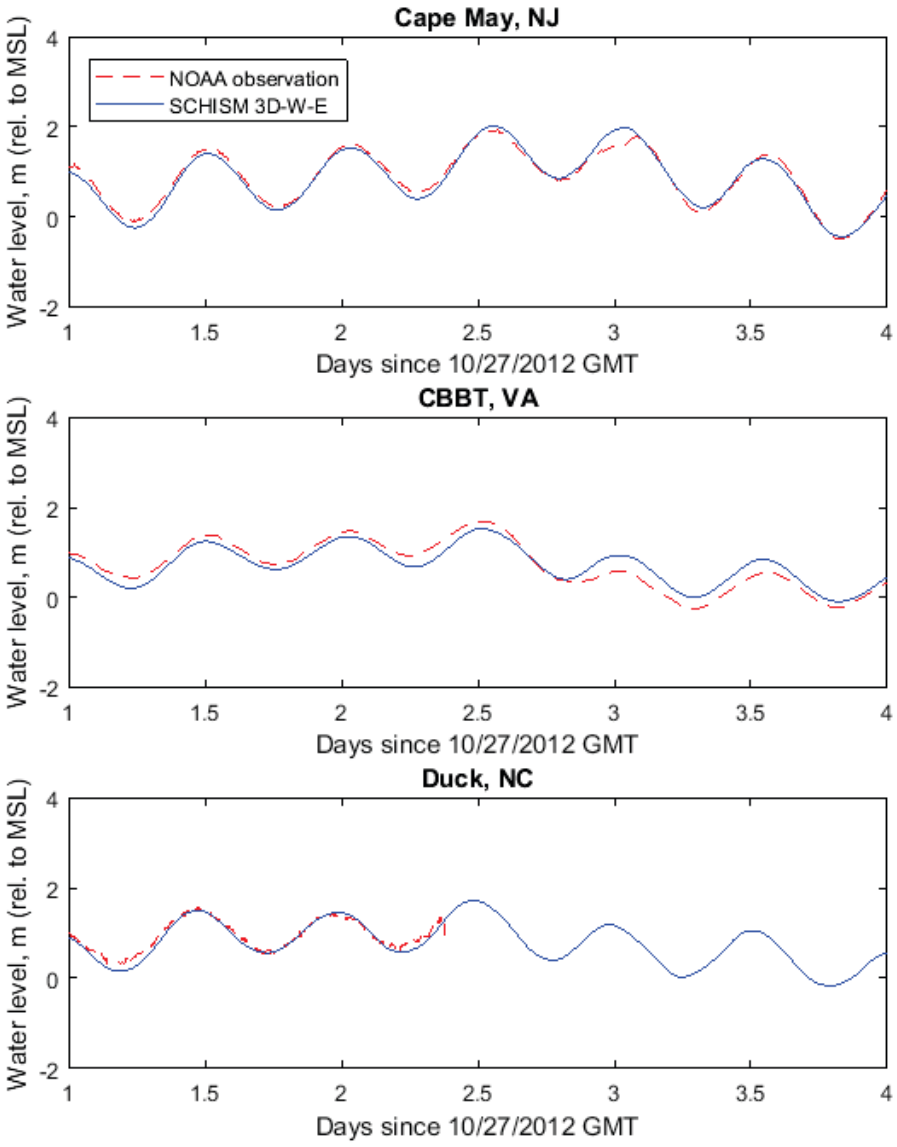

Figure 13: Time series of comparisons of NOAA observation and SCHISM modeled storm tide (3D-W-E: 3-D coupled wind wave model using ECMWF forcing) results for stations along the Southeastern coast. Note there was discontinuity in NOAA observations at Duck.

3.2.3. Effects of Wind Forcing, 3-D Formulation, and Wave-Current Coupling

In simulating coastal surge dynamics, it is well-known that the quality of the wind forcing can significantly influence the simulation results. The 3-D formulation and the momentum transported by wind waves are also shown to be important. The effects of these dynamics including: (1) surface stress as a function of wind speed and direction (Lapetina and Sheng, 2015; Magnusson et al., 2014); (2) bottom stress as a function of near-bottom velocity (Weisberg and Zheng, 2008; Zheng et al., 2013); and (3) wave-induced radiation stress gradient (Huang et al., 2010; Sheng et al., 2010), were well-recognized.

In this section, the quality of surface wind forcing, bottom stress representation in 3-D model, and wave-current coupling will be analyzed to evaluate their contribution to the total water level during Hurricane Sandy. In order to investigate these corresponding issues, a total of eight storm tide simulations were set up (their names are shown below) and their results were compared with the observation in New York City.

1) 3D-W-N: The 3-D SCHISM coupled with WWMIII (NAM atmospheric forcing);

2) 3D-N: The 3-D SCHISM alone (NAM atmospheric forcing);

3) 2D-W-N: The 2-D SCHISM coupled with WWMIII (NAM atmospheric forcing);

4) 2D-N: The 2-D SCHISM alone (NAM atmospheric forcing);

5) 3D-W-E: The 3-D SCHISM coupled with WWMIII (ECMWF atmospheric input);

6) 3D-E: The 3-D SCHISM alone (ECMWF atmospheric field input);

7) 2D-W-E: The 2-D SCHISM coupled with WWMIII (ECMWF atmospheric input);

8) 2D-E: The 2-D SCHISM alone (ECMWF atmospheric field input).

3.2.3.1. ECMWF vs. NAM

Comparisons of storm tide simulations using different atmospheric forcings (NAM, ECMWF) were conducted to determine how the quality of wind forcing can affect storm surge simulation. These two forcing were both concatenated short-period forecast (0, 3, 6, 9 hours) with reanalysis at 00Z and 12Z on each day. Figures 14-17 show the time series of comparisons between simulation results from the following groups respectively, and NOAA observation at New York City (The Battery, NY): 1) 3D-W-N, 3D-W-E; 2) 3D-N, 3D-E; 3) 2D-W-N, 2D-W-E; 4) 2D-N, 2D-E.

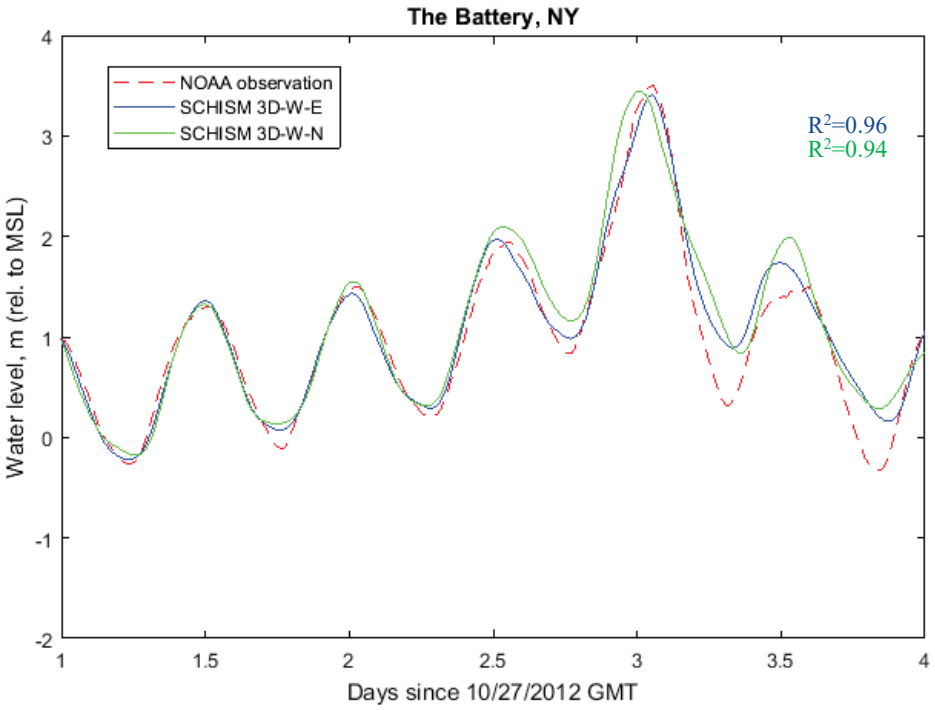

Figure 14: Time series of comparisons of NOAA observation and storm tide model (3D-W-N, 3D-W-E) results at The Battery, NY. The R^2 value is labeled with corresponding color.

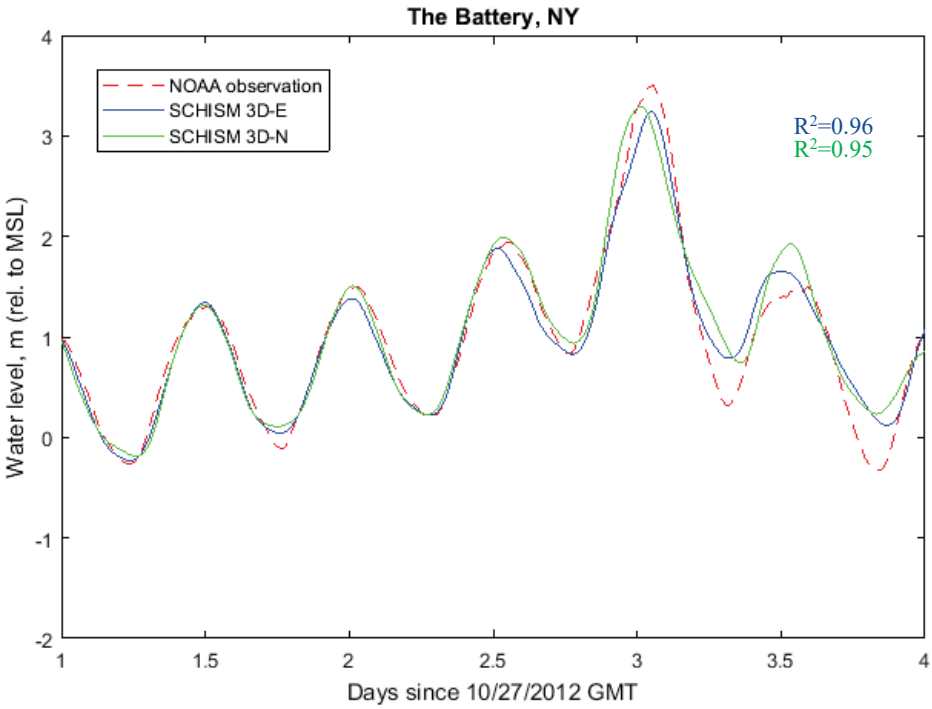

Figure 15: Time series of comparisons of NOAA observation and storm tide model (3D-N, 3D-E) results at The Battery, NY. The R^2 value is labeled with corresponding color.

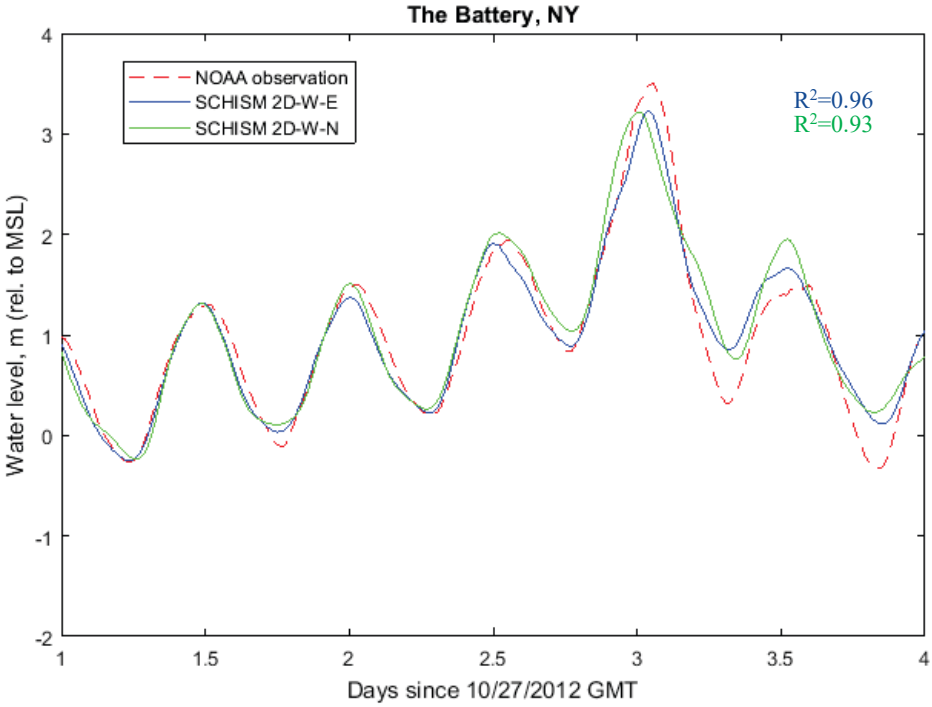

Figure 16: Time series of comparisons of NOAA observation and storm tide model (2D-W-N, 2D-W-E) results at The Battery, NY. The R^2 value is labeled with corresponding color.

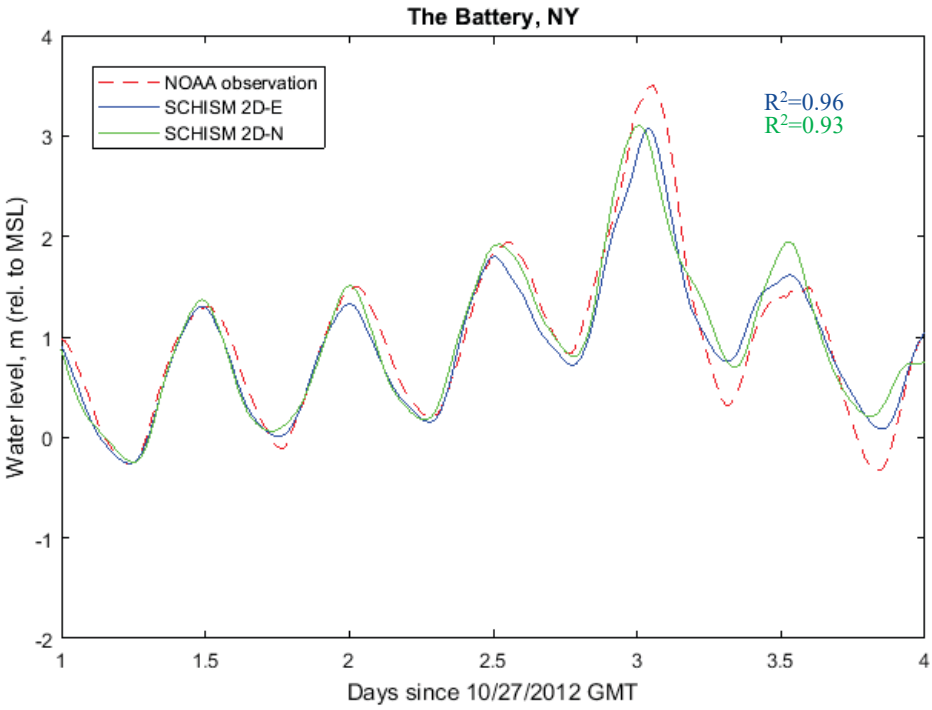

Figure 17: Time series of comparisons of NOAA observation and storm tide model (2D-N, 2D-E) results at The Battery, NY. The R^2 value is labeled with corresponding color.

In general, the runs using ECMWF atmospherical model have better storm tide results during landfall than those using the NAM model in all four comparison scenarios. The NAM runs have larger phase discrepancy and overprediction. ECMWF and NAM were compared in wind speed forecast at different stations in the model domain with NOAA NBDC wind observation (u/v wind) data. For example, five operational observation stations along East Coast were chosen to compare NAM, ECMWF, and observed winds during Hurricane Sandy: CHLV2 (outside Chesapeake Bay mouth), CMAN4 (Delaware Bay mouth), 44065 (New York/New Jersey Bight), BGNN4 (New York Harbor), BRHC3 (Long Island Sound). All observed wind speeds were adjusted to the speed at 10 m above ground speed. The comparisons (u, v, wind speed magnitude)

show that around landfall time, ECMWF has much better quality in both u/v direction as well as wind speed than NAM product as shown in Figure 18 – Figure 22 at all stations. Before Sandy made landfall, NAM was slightly better phase at some stations, e.g. 44065 and BGNN4. This is also consistent with the time series plot at The Battery, NY that the NAM runs have slightly better phase before 10/29 12:00 GMT. Also, in Long Island Sound, the error of both wind forcing is larger than other stations, which may explain the larger error of storm tide in this region.

Thus, these comparisons confirm that the quality of the wind field has a direct impact on the accuracy of storm tide simulations as the surface stress during landfall was dominated by wind stress (see Section 2.1.2: Eq. (5)). Since the model runs using ECMWF forcing clearly have the better results when Sandy made landfall, it will be used for later comparisons to analyze the effects of 3-D formulation and wind wave.

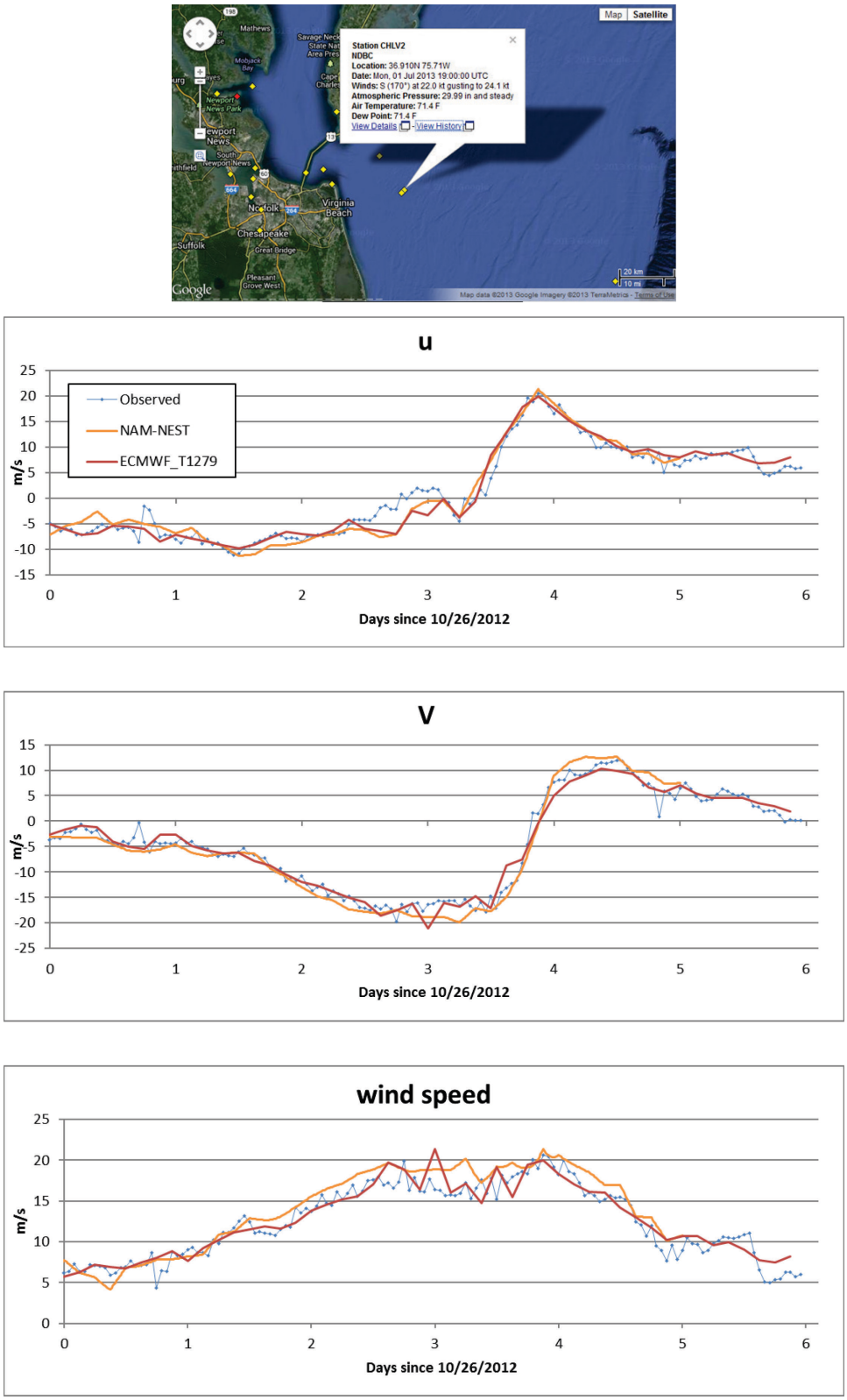

Figure 18: From top to bottom: location of NDBC station CHLV2; time series of comparisons of u, v, wind speed magnitude between observation, NAM-NEST, and ECMWF T1279.

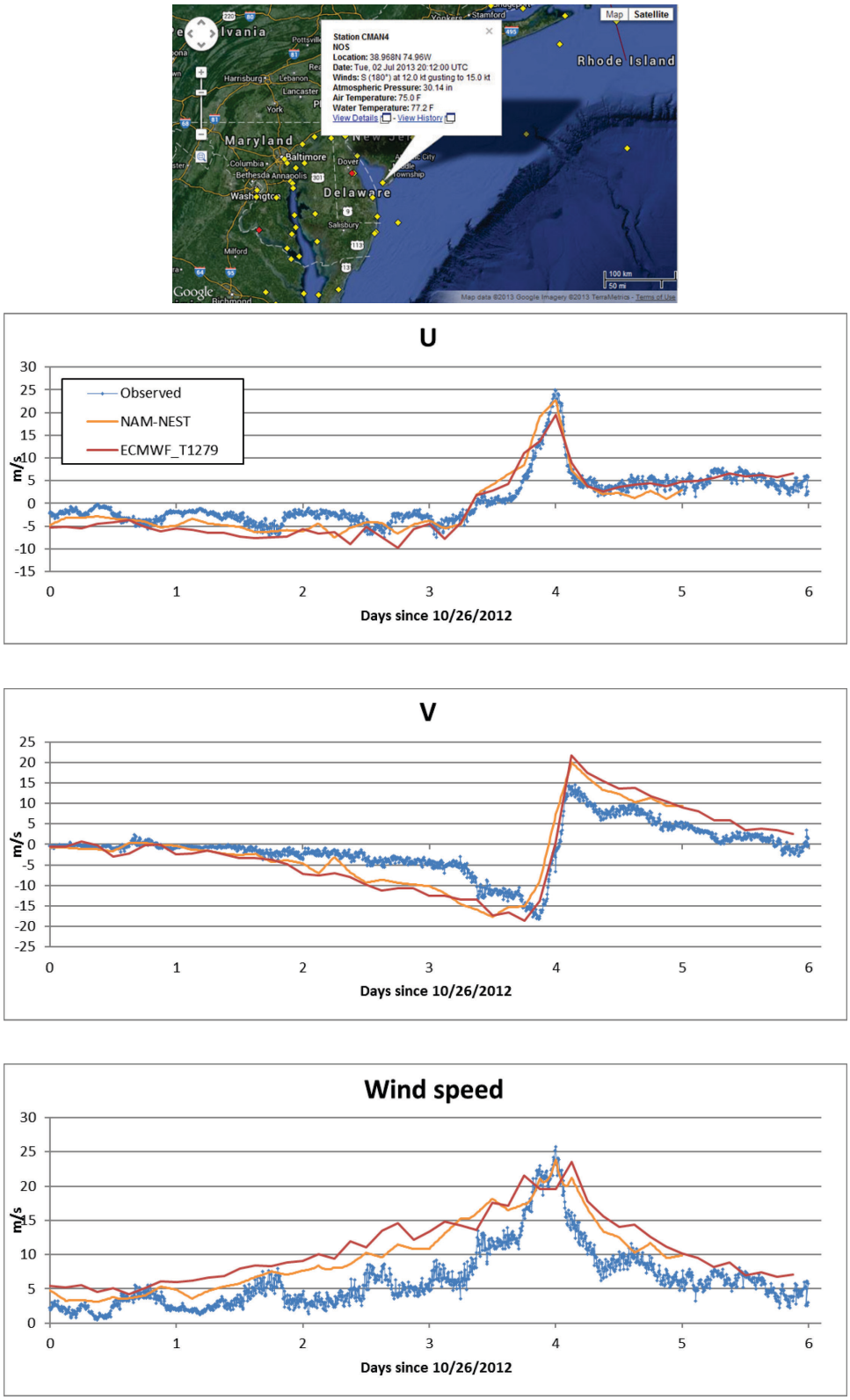

Figure 19: From top to bottom: location of NDBC station CMAN4; time series of comparisons of u, v, wind speed magnitude between observation, NAM-NEST, and ECMWF T1279.

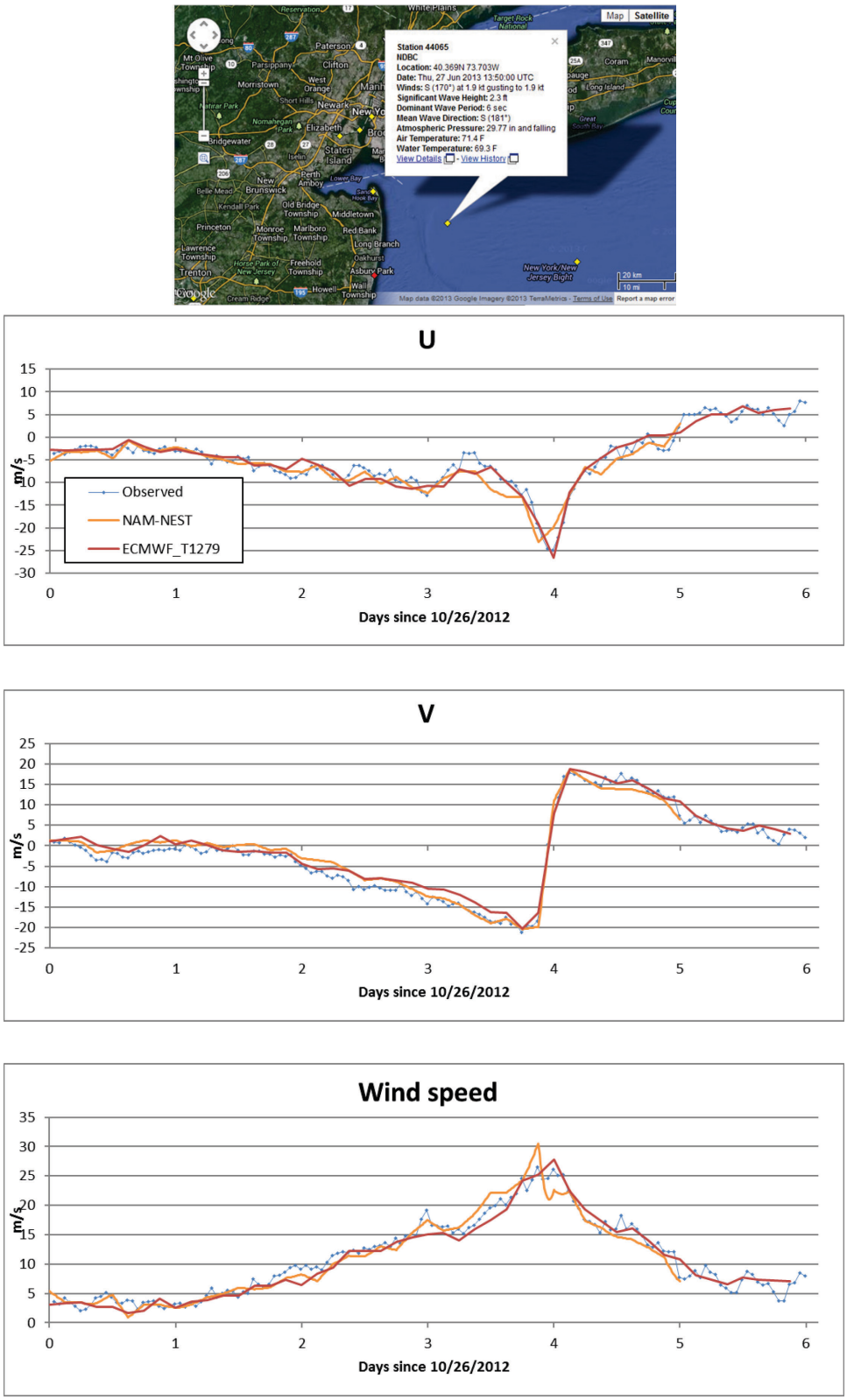

Figure 20: From top to bottom: location of NDBC station 44065; time series of comparisons of u, v, wind speed magnitude between observation, NAM-NEST, and ECMWF T1279.

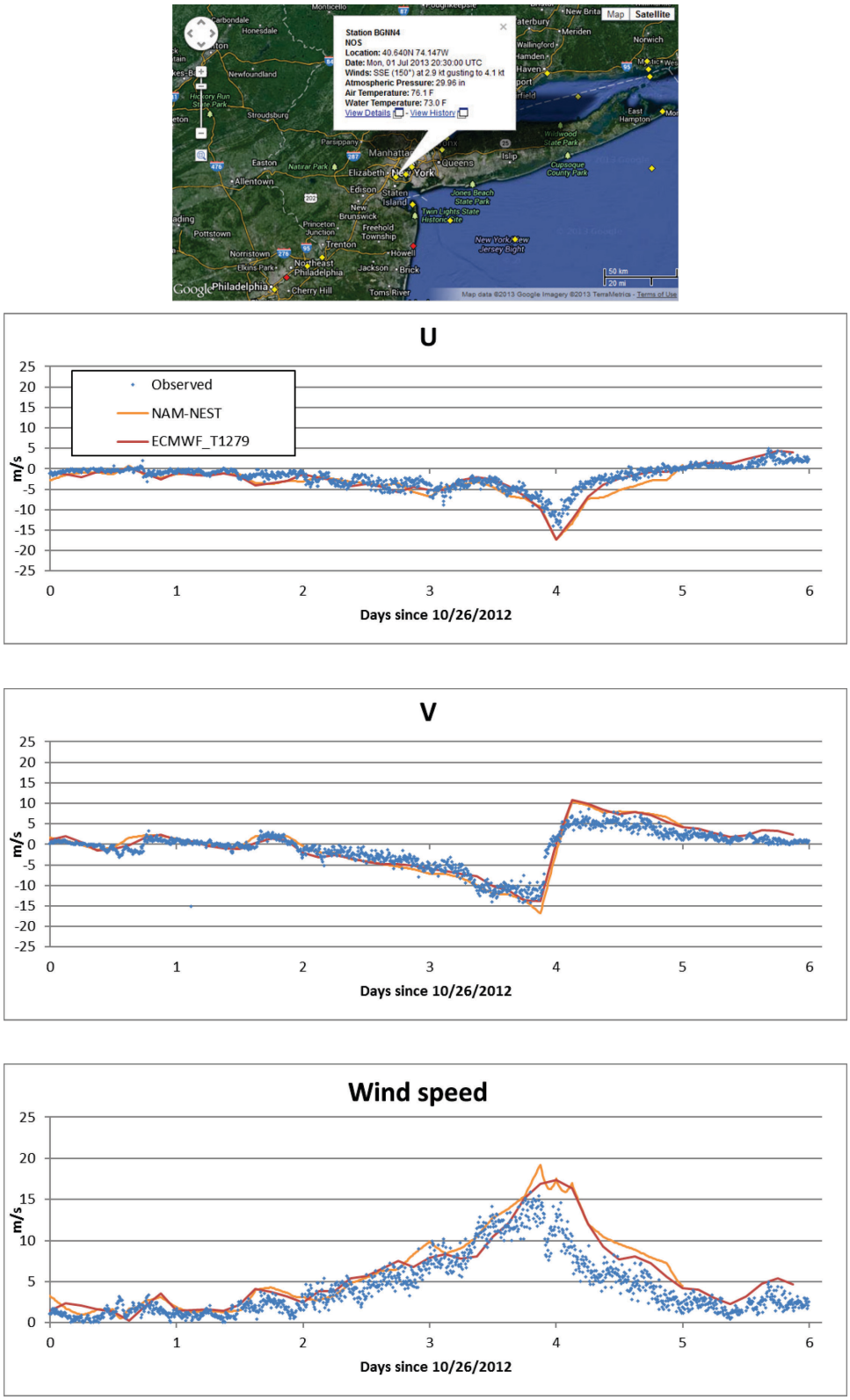

Figure 21: From top to bottom: location of NDBC station BGNN4; time series of comparisons of u, v, wind speed magnitude between observation, NAM-NEST, and ECMWF T1279.

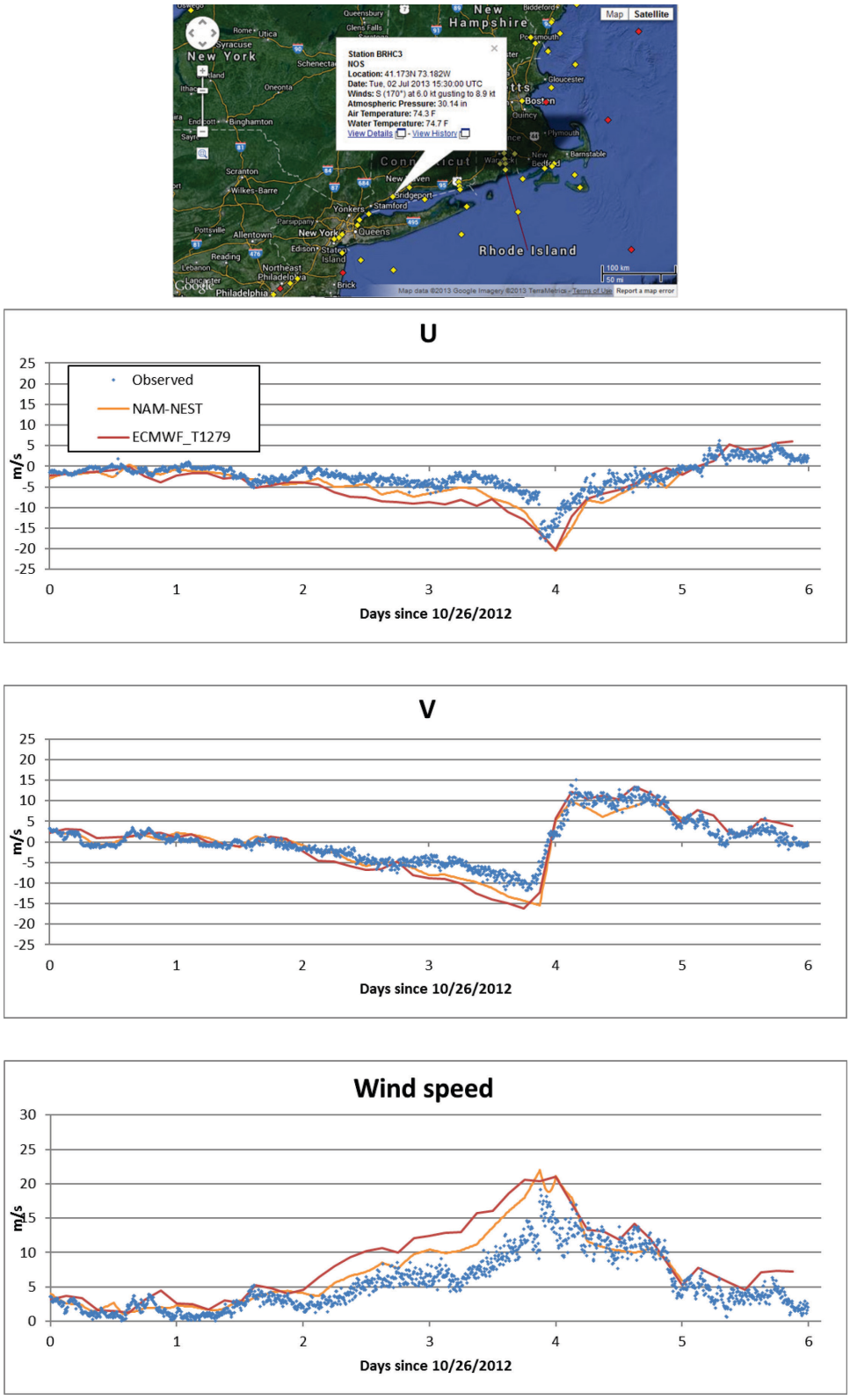

Figure 22: From top to bottom: location of NDBC station BRHC3; time series of comparisons of u, v, wind speed magnitude between observation, NAM-NEST, and ECMWF T1279.

3.2.3.2. 3-D Barotropic Model vs. 2-D Model

To verify the necessity of a 3-D circulation model in accurately modeling the maximum storm tide over New York City, comparisons between 4 tests: 3D-W-E, 2D-W-E, 3D-E, and 2D-E in two groups below with observations are presented in Figures 23 and 24: 1) 3D-W-E, 2D-W-E; 2) 3D-E, 2D-E.

The comparisons show that 3D-W-E and 3D-E increased and improved storm tide results around landfall by 5-10% over 2D-W-E and 2D-E, respectively. Also, the difference between 3-D and 2-D models was quite similar in the coupled model as in the circulation-only model, so it is necessary to analyze why the 3-D model is intrinsically different from the 2-D model.

The major difference in storm surge results between 3-D and 2-D modeling follows from the momentum balances. Storm surge derives from the tendency of vertically integrated pressure gradient force (due to the sea surface slope) to balance the difference between the surface and bottom stresses. The surface stress is the wind stress, which should be same in either 2-D or 3-D models, for they use exactly same formulation of wind stress. However, the bottom stress is where 2-D and 3-D models make the difference. The bottom stress usually follows a quadratic friction law, but in the 2-D model this is based on depth-averaged velocity, while in the 3-D model it is based on the near-bottom velocity. Hence, the bottom stress will be different in these two models when the near-bottom velocity differs from the vertically averaged velocity. And this difference could affect the surge estimation. When the bottom stress calculated by a 2-D model is inconsistent with that calculated by a 3-D model, the only recourse (other than the Coriolis accelerations and horizontal diffusions) in the momentum balance is for the

pressure gradient force to be changed. As storm surge is the integral of the surface slope in spatial and temporal dimensions, misrepresentation of bottom stress will result in errors in surge. During the period of a hurricane's landfall, the bottom stress is usually overestimated in the 2-D model of a storm surge simulation because the vertically average velocity is larger than the near-bottom velocity. In this case, the pressure gradient force (the surface slope) is underestimated. Thus, the surge heights are lower than those from the 3-D model. The modeled peak water level by a 2-D model is approximately 0.15 – 0.18 m lower than that by a 3-D model.

So, the 3-D structure is intrinsically important in modeling storm surge. 2-D models may overestimate (or underestimate) bottom stress, requiring physically unrealistic parameterizations of surface stress or other techniques for model calibration (Weisberg, et al., 2008) like in ADCIRC model. The analysis of the dynamical balances inherent to storm surges and the comparisons of model results suggest that 3-D models are preferable over 2-D models for simulating storm surges. Currently, most of the U.S. agencies charged with hurricane forecast, planning, and surge risk mapping utilize 2-D storm surge models. The findings in this dissertation would suggest that to be changed to 3-D models if the efficiency of a 3-D model is not an issue operationally.

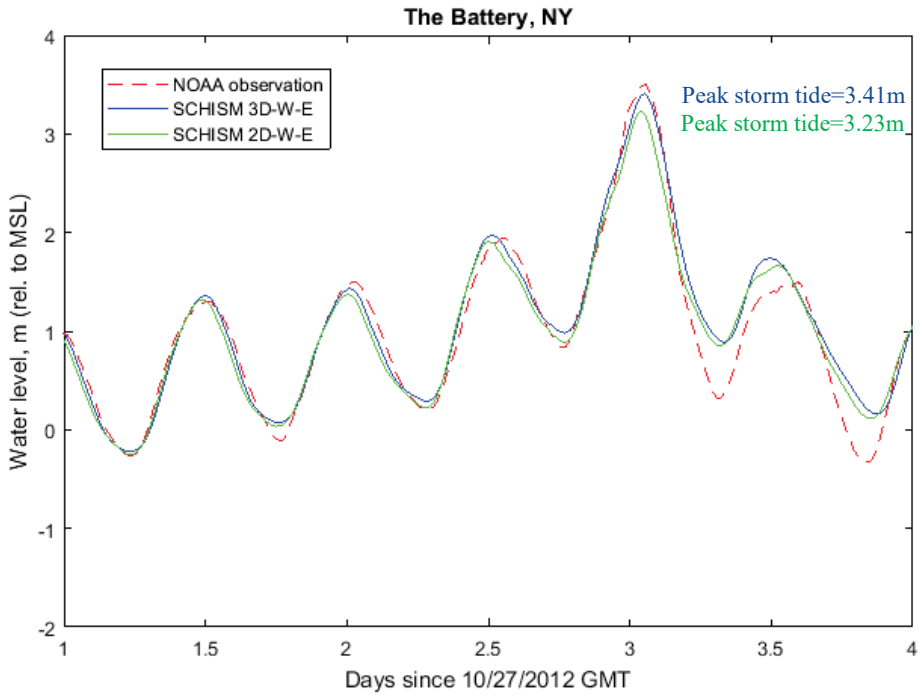

Figure 23: Time series of comparisons of NOAA observation and storm tide model (3D-W-E, 2D-W-E) results at The Battery, NY. The peak storm tide result is labeled with corresponding color.

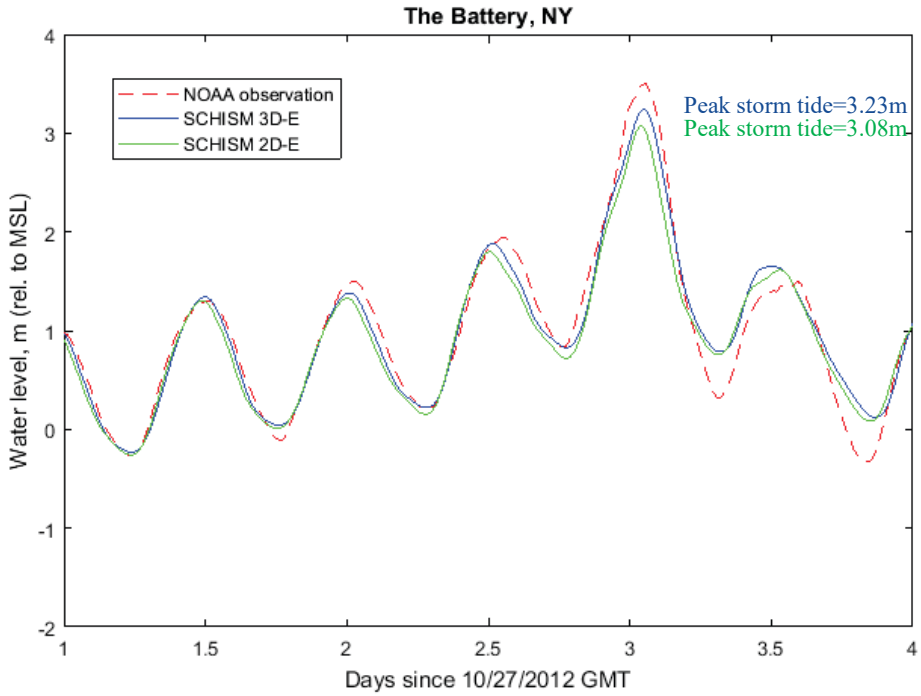

Figure 24: Time series of comparisons of NOAA observation and storm tide model (3D-E, 2D-E) results at The Battery, NY. The peak storm tide result is labeled with corresponding color.

3.2.3.3. Coupled Wave-Current Model vs. No-Wave Model

Comparisons between 4 tests: 3D-W-E, 3D-E, 2D-W-E, and 2D-E with observations (Figures 25 and 26) in two groups below: 1) 3D-W-E, 3D-E; 2) 2D-W-E, 2D-E, are presented to show the importance of including the effects of wind wave in modeling the maximum storm tide over New York City. Overall, among these four models, 3-D SCHISM coupled with WWMIII (3D-W-E) performs the best and can reach the maximum storm tide with the minimum error. 3D-W-E and 2D-W-E have higher and more accurate peak water level than 3D-E and 2D-E, respectively (Figures 25 and 26). The increase is on the order of 5-10% of the total water level. The effects of wind wave on 2-D and 3-D models are similar in this case because the radiation stress formulation is the same for both the 2-D and 3-D simulations.

The wind wave model's performance was evaluated during this extreme event. The modeled significant wave heights as well as peak discrete wave periods calculated by WWMIII using ECMWF wind forcing are compared with available observations at 2 NOAA/NDBC buoy stations located in the New York/New Jersey Bight (Station 44025 and Station 44065) (Figure 27). At Stations 44065 and 44025, observed significant wave heights could reach 9.9 m while the wave model is able to catch the peak at the right time with reasonable error less than 10% of maximum height. Comparisons of peak discrete periods also show satisfactory model performance: around landfall (October 30, 2012 UTC), the error of modeled wave period is quite small, on the order of 1 second.

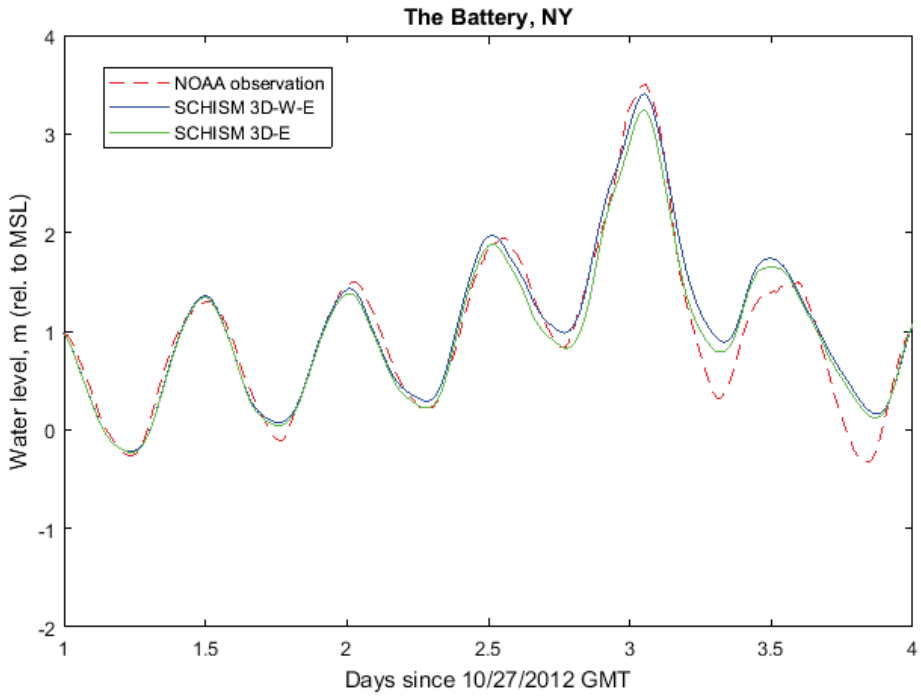

Figure 25: Time series of comparisons of NOAA observation and storm tide model (3D-W-E, 3D-E) results at The Battery, NY.

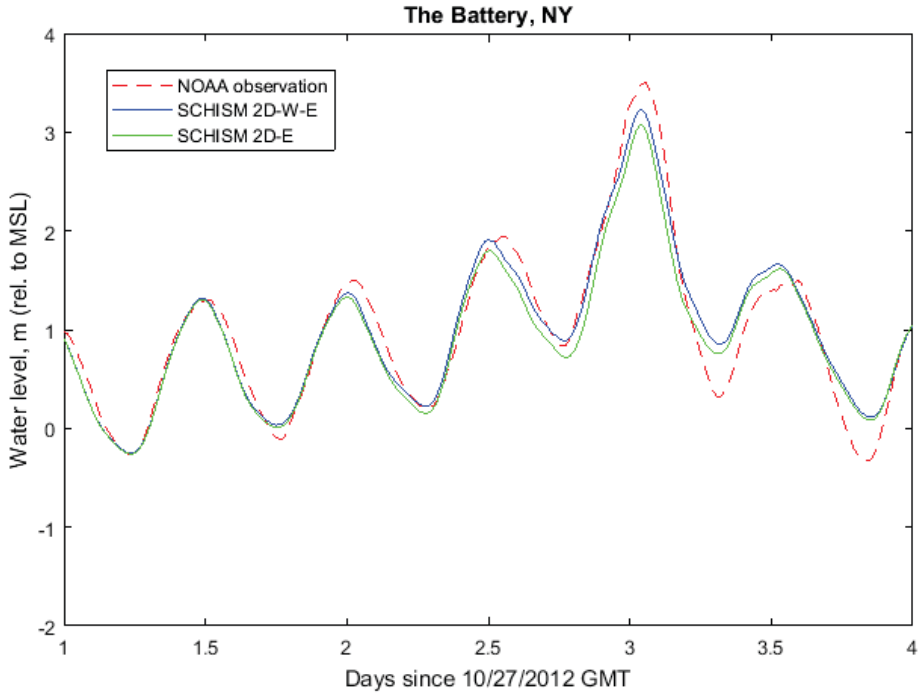

Figure 26: Time series of comparisons of NOAA observation and storm tide model (2D-W-E, 2D-E) results at The Battery, NY.

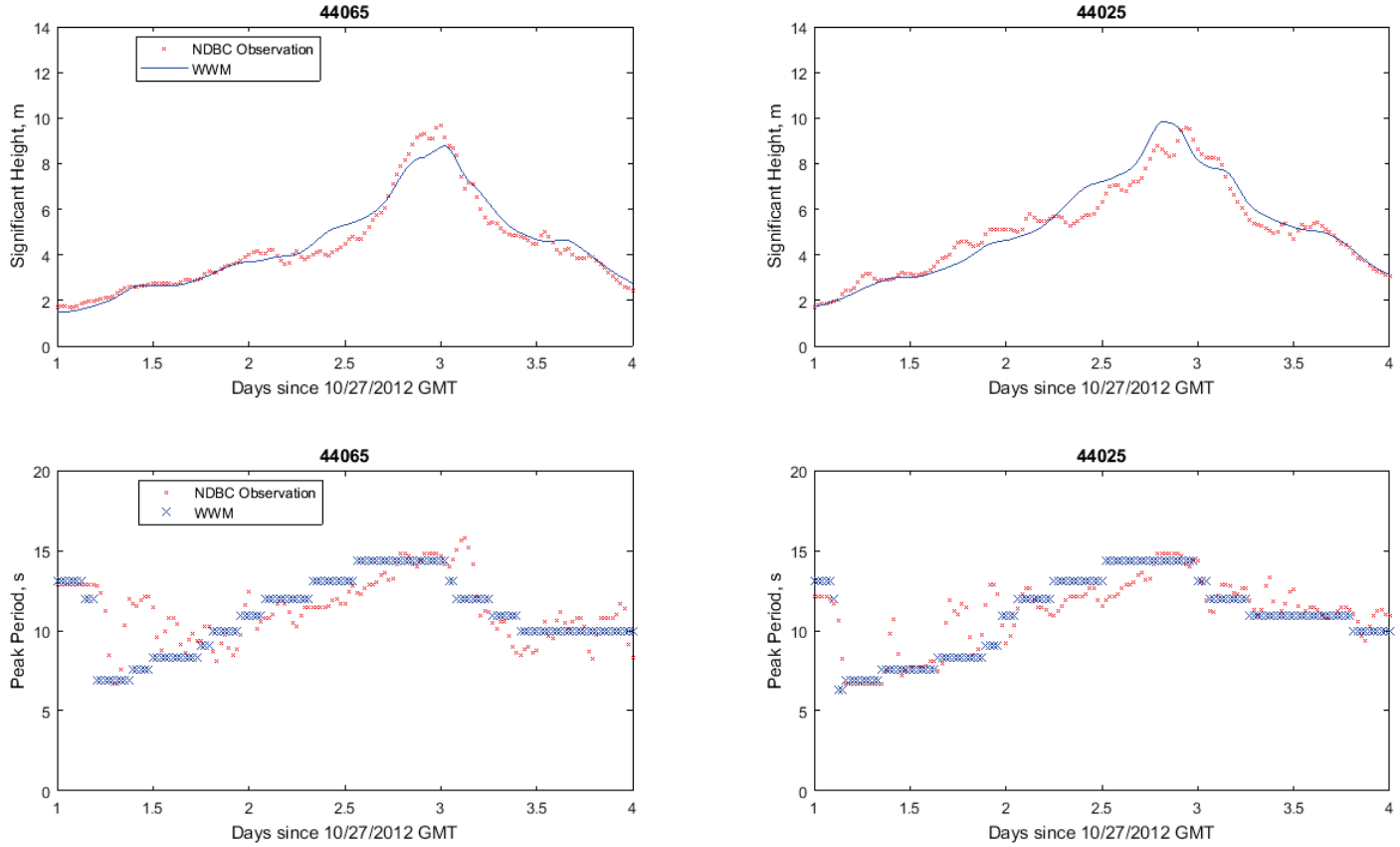

Figure 27: Time series of comparisons of NDBC observation and WWMIII model results at Station 44025 and Station 44065.

The spatial pattern of the modeled maximum storm tide during Hurricane Sandy shows that the water elevation increases when approaching the shoreline and reaches the maximum value in the shallow areas near New York City (Figures 28 and 29). The modeled maximum significant wave heights decrease when the higher than 10 m wave starts to break near shore (Figure 30), and the change of wave heights generally followed the change of water depths. The wave setup in this section was calculated as the difference between (maximum storm tide in the coupled model) and (maximum storm tide in the no-wave model), to analyze the effects of wind wave on the peak water elevation. Figure 31 shows the spatial distribution of wave setup in Hurricane Sandy. The wave setup extended to areas that were not directly exposed to the highest waves such as in estuaries, especially in the New York Harbor where the larger wave setup occurred. In much deeper water like Long Island Sound, the wave setup was very small.

The wave-induced increase in water level computed with the coupled model ranged from 0.1 to 0.3 m (5-10 % of maximum storm tide) and was spatially variable. When the hurricane pushed large waves into the relatively narrow entrance of New York Bay, it caused significant wave breaking (corresponding to the rapidly reduced wave heights as shown in Figure 30) and thus large radiation stress gradients onshore (based on Section 2.2.2 Eq. (13)). When the radiation stress gradients were added into the momentum equation of the coupled model, the pressure gradient (surface slope) term needs to be larger to balance the radiation stress terms. Thus, the integrated total water level in those areas is larger. In general, in shallow areas where wave breaking is common, the effects of wind wave on storm tide results can be more significant than in the deep water.

The coupled model was found to be a useful tool in identifying regions where wave setup effects were important, and the accuracy of storm tide simulation can be improved.

In summary, detailed comparisons of results from 8 different storm tide model runs were made and the conclusion was that the 3-D SCHISM barotropic model using ECMWF wind forcing and coupled with the wind wave model WWMIII has the best overall performance at New York City during Hurricane Sandy. The results are better than a previous study for Hurricane Sandy using 2-D SELFE model (Loftis, 2014). This is mainly because it could utilize higher quality atmospheric forcing, more accurately calculate the bottom stress in 3-D mode, and include wave effects from breaking waves near shore with the wind wave model.

Despite overall excellent performance of SCHISM model for simulating storm tide during Hurricane Sandy, we did observe over-prediction of the water level for 1 day after the peak storm surge at The Battery in New York City. This over-prediction of water level in the later stage of Hurricane was also observed in the lower Chesapeake Bay during Hurricane Isabel (not shown). It is our belief that the unusual water level drop after the peak surge at The Battery is due to the sea level set down in the offshore as a result of the Ekman transport by the prevailed southerly wind after Hurricane made the landing. To model the coastal sea level set down properly, it may require more accurate wind forcing after landfall and a 3-D baroclinic model with proper representation of the vertical stratification over the coastal water.

In next section, the simulation of Hurricane Irene (2011) along VA, NC coasts, and inside Chesapeake Bay, is based on this successful large-scale storm tide modeling application.

Figure 28: Bathymetry in part of SCHISM model domain near New York/New Jersey Bight.

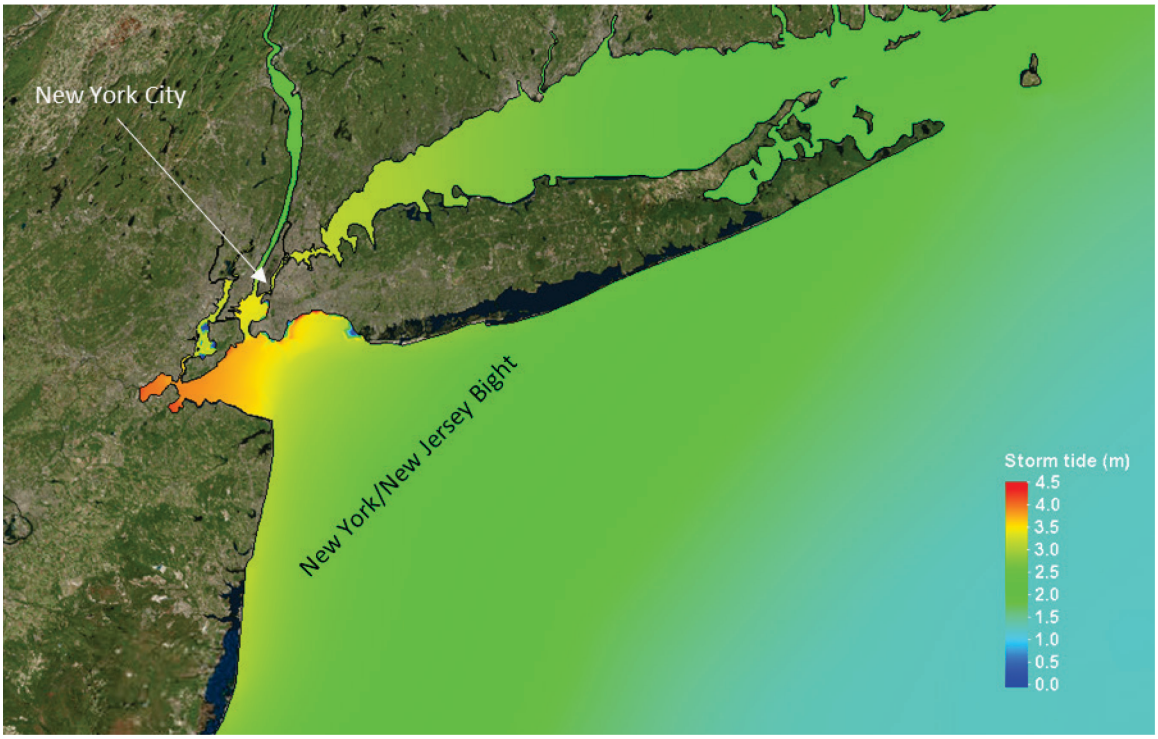

Figure 29: Maximum storm tide modeled by 3-D SCHISM coupled with WWMIII in Hurricane Sandy.

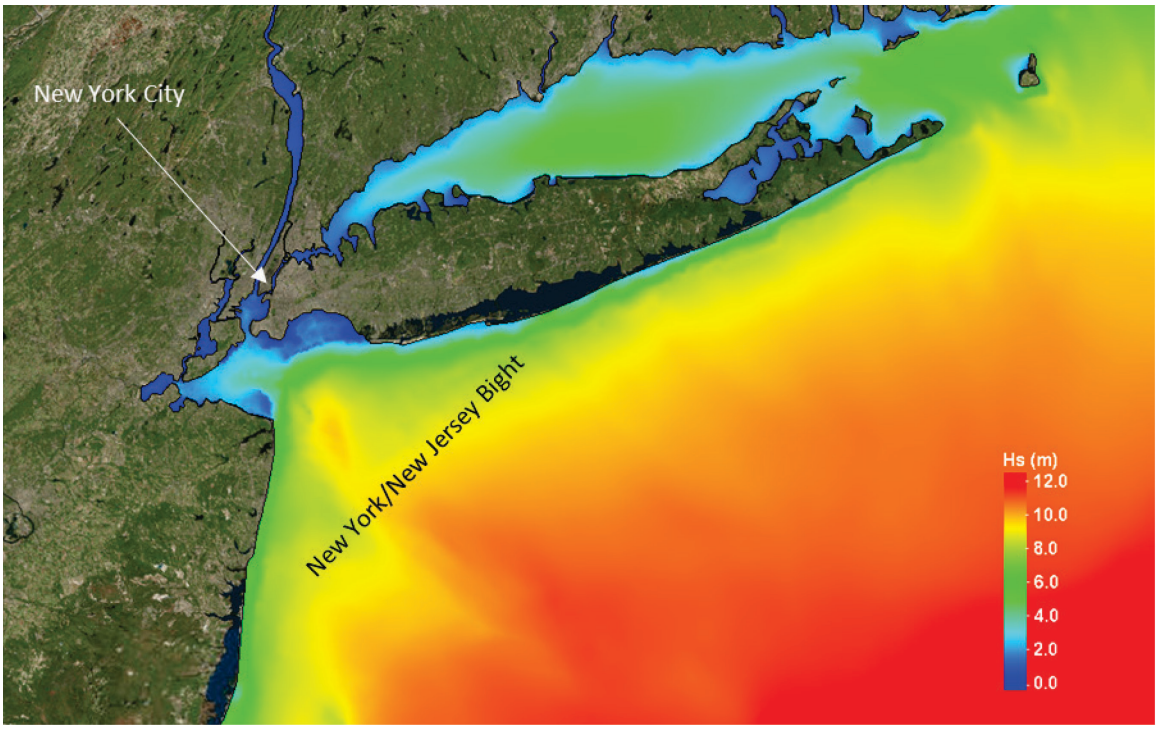

Figure 30: Maximum significant wave height modeled by 3-D SCHISM coupled with WWMIII in Hurricane Sandy.

Figure 31: Wave setup on maximum water elevation in Hurricane Sandy.

3.3. Hurricane Irene (2011) in Southern Chesapeake Bay

The Hurricane Irene in 2011 was a large and powerful Atlantic hurricane that left extensive flood and wind damage along its path through the Caribbean, the United States East Coast and as far north as Canada (NOAA, 2011). Irene made landfall near Cape Lookout, North Carolina at around 11:30 UTC on August 27, 2011 as a strong Category 1 storm (Figure 32). The peak wind gust recorded was 115 mph at the Cedar Island Ferry Terminal in Carteret County as the eye was moving ashore (Figure 33). The peak storm tide (relative to MSL) at the mouth of Chesapeake Bay (CBBT) was around 1.75 m (Figure 34) when the peak surge coincided with high tide.

Irene caused widespread damage across a large portion of the eastern United States as it moved north-northeastward, bringing significant effects from the mid-Atlantic through New England. Roughly 7.4 million homes and businesses lost electrical power, with approximately 3.3 million still without power as of August 30, three days after landfall. Coastal areas suffered extensive flood damage followings its potent storm surge, with additional freshwater flooding reported in many areas. The storm spawned scattered tornadoes, causing significant property damage as evidenced by destroyed homes. Rivers in at least six Northeastern states reached hundred-year flood levels. Throughout its path in the contiguous United States, Irene caused damages of approximately $15.6 billion (2011 USD) (NOAA, 2011).

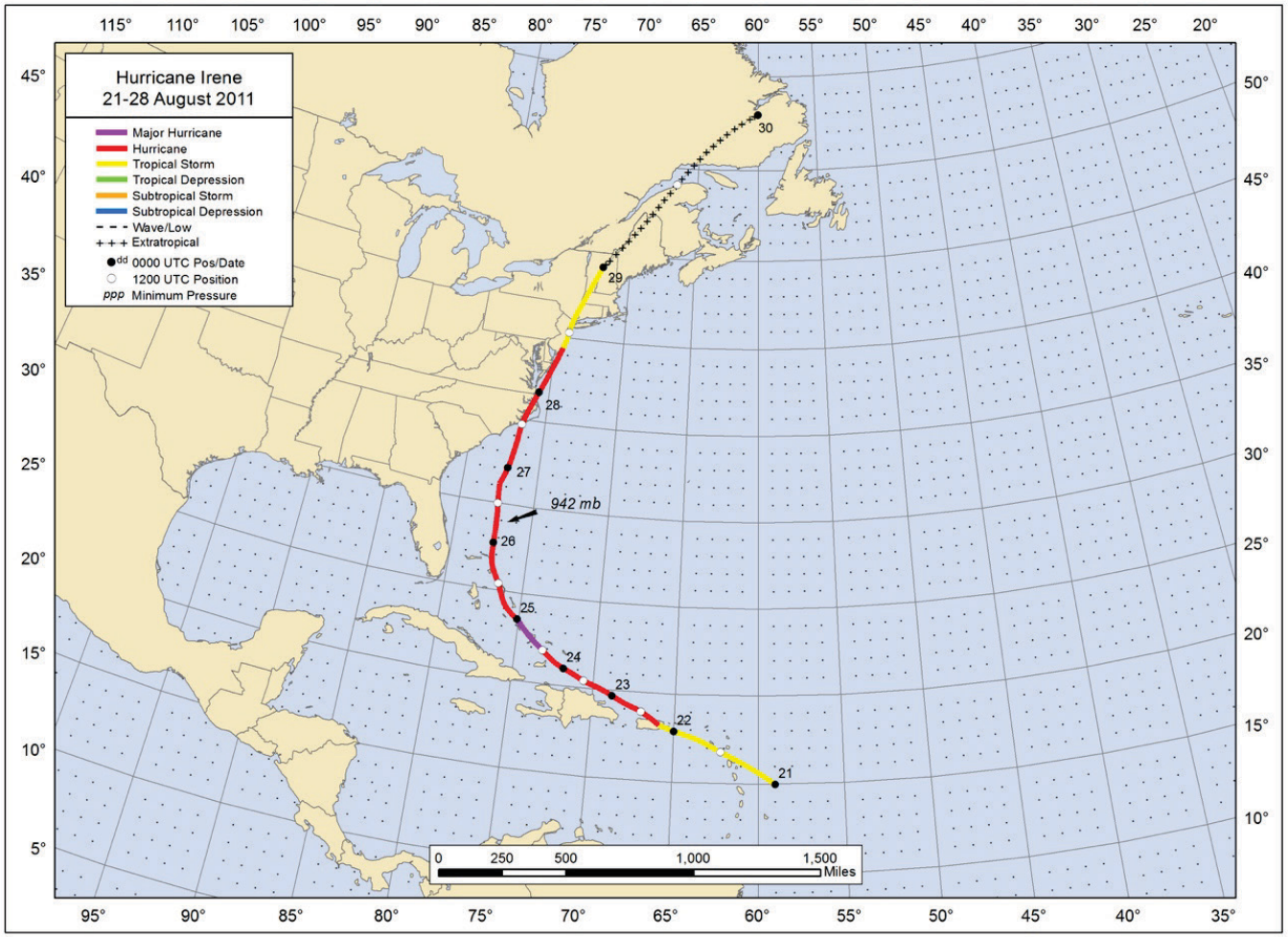

Figure 32: Hurricane Irene (2011) Track reported by NOAA National Hurricane Center.

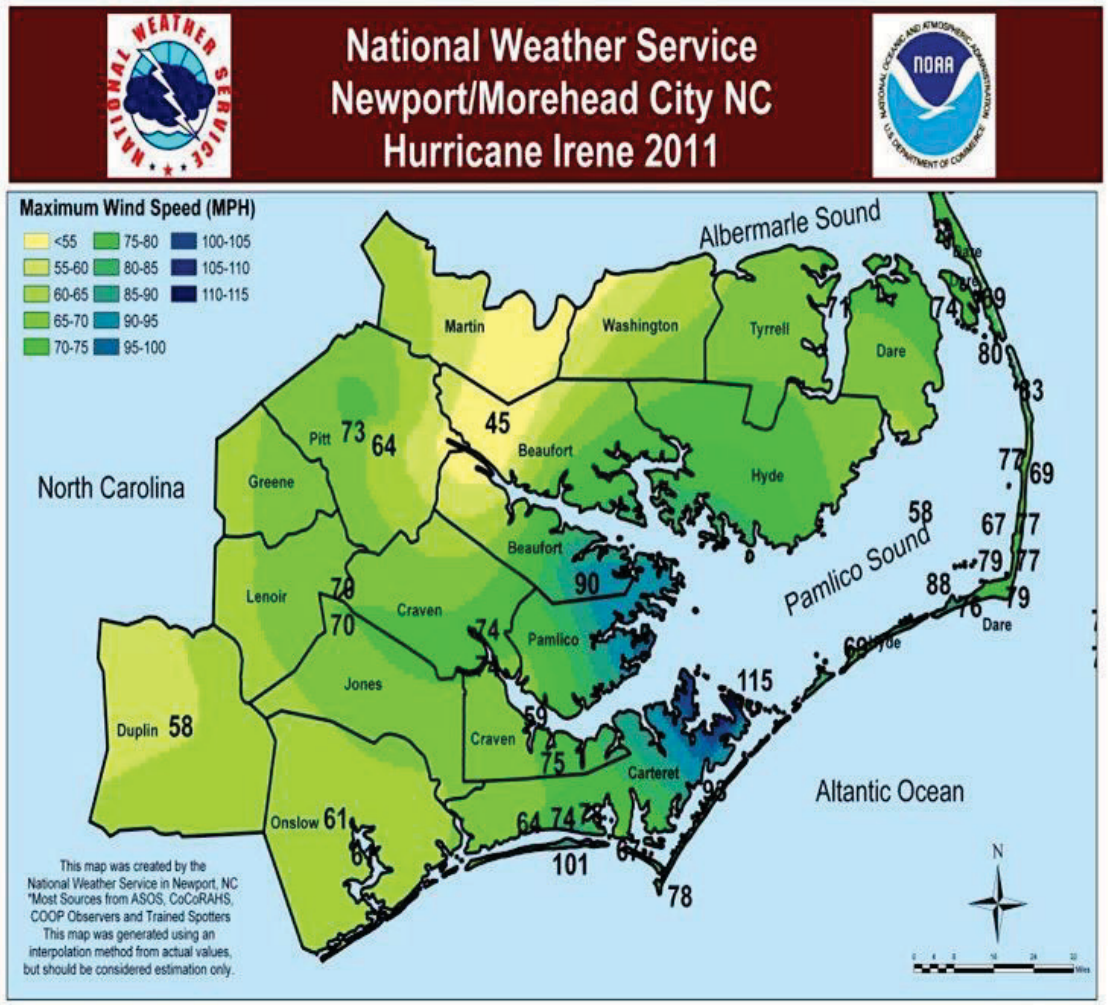

Figure 33: Peak Wind Gusts from Hurricane Irene, August 27, 2011.

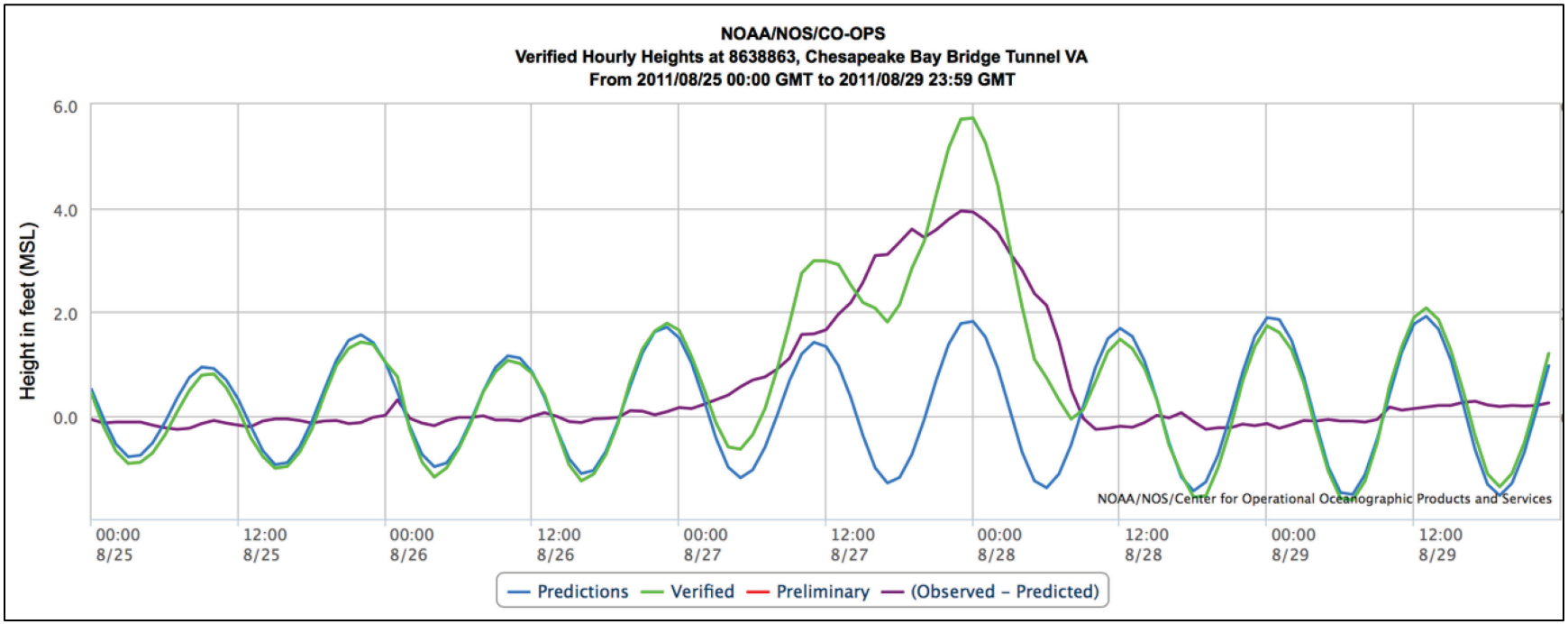

Figure 34: Observed water level at CBBT, VA during Hurricane Irene.

Based on the excellent model performance during Hurricane Sandy from Section 3.2, a 3-D barotropic storm tide simulation by SCHISM coupled with WWMIII using ECMWF wind forcing was also set up to simulate the storm tide and wind wave during Hurricane Irene. A large-scale grid was specifically refined inside Chesapeake Bay (the highest resolution is approximately 15 m in the lower Bay) with 10 m-resolution DEM, which covers all NOAA tidal gauges inside the Bay. The refined grid consists of 788,915 nodes and 1,524,968 elements. The simulation was also executed on Sciclone HPC cluster with 200 computation cores, and the coupled model had approximately 50 times real-time speedup. The coupled wave and storm tide run started on August 17th 00:00 UTC and ended on September 1st 00:00 UTC, 2011, using the same temporal coverage of wind and pressure fields. 12km 3-hourly ECMWF T1279 product was used for this storm tide hindcast effort. To analyze the effects of wind wave on Hurricane Irene storm tide simulation, a 3-D current-only model was also setup and its results were used to compare with the coupled wave-current model to estimate the wave radiation stress gradients contribution to overall water levels. The efficiency of this model was around 100 times real-time speedup. Tidal prediction and verified observation data from 12 NOAA tide gauges along the East Coast and inside Chesapeake Bay were utilized for comparisons with modeled astronomical tides and storm tide during Hurricane Irene (2011). All hourly predicted and 6-minute observed water level data were collected at respective data sources in meters relative to MSL. 3 NDBC Buoy stations off Virginia and North Carolina coasts were used to evaluate WWMIII model performance.

Tidal calibration and harmonic analysis were conducted for three months from July 1st through September 30th, 2011. Observed water level between August 17th and

September 1st, 2011 were used for comparisons with modeled storm tide. R^2, RMSE, and MAE values were calculated to evaluate SCHISM storm tide model performance. The comparisons between modeled water level and NOAA data are grouped into two regions: 1) Outside the Bay: VA, NC, and SC coast; 2) Inside Chesapeake Bay.

3.3.1. Model Forcing and Available Observation

Tidal forcing is applied at the open ocean boundary via similar approach as in the Hurricane Sandy simulation. Tidal elevations are forced along the 294 nodes comprising the Atlantic open-ocean boundary using eight astronomical tidal constituents including the semidiurnal M_2, N_2, S_2 and K_2 constituents along with the diurnal O_1, K_1, Q_1 and P_1 constituents. Atmospheric outputs, 10 m u/v wind and mean sea-level pressure, obtained from atmospheric models were applied as model's surface forcings. The atmospheric model used here is: 12-km resolution, 3-hourly ECMWF T1279 product (concatenated short period forecasts with reanalysis at 00Z and 12Z) for Hurricane Irene (08/17 00:00 UTC to 09/01 00:00 UTC, 2011) including 10 m u/v wind in m/s; mean sea level pressure in Pa. Atmospheric model data outputs were processed into NetCDF files for use with the 'sflux' input format. Boundary forcing for WWMIII was not required as the hurricane winds were completely contained within the model domain during the hurricane events. Initial condition is set as default as no wave exists in the model domain at the beginning of a simulation.

For the Hurricane Irene simulation, the observations used for comparisons were at:

a) 12 NOAA tide gauges along the U.S. Southeast Coast and inside Chesapeake Bay;

b) 3 NBDC observation buoy stations off VA, NC, and SC coasts.

The 12 NOAA tidal gauges were used for tidal calibration and comparisons with modeled storm tide elevation relative to MSL. The 3 NDBC buoys were utilized for comparisons with modeled significant wave height, and peak wave period. The locations and detailed information of these stations are shown in Figure 35 and Table 3.

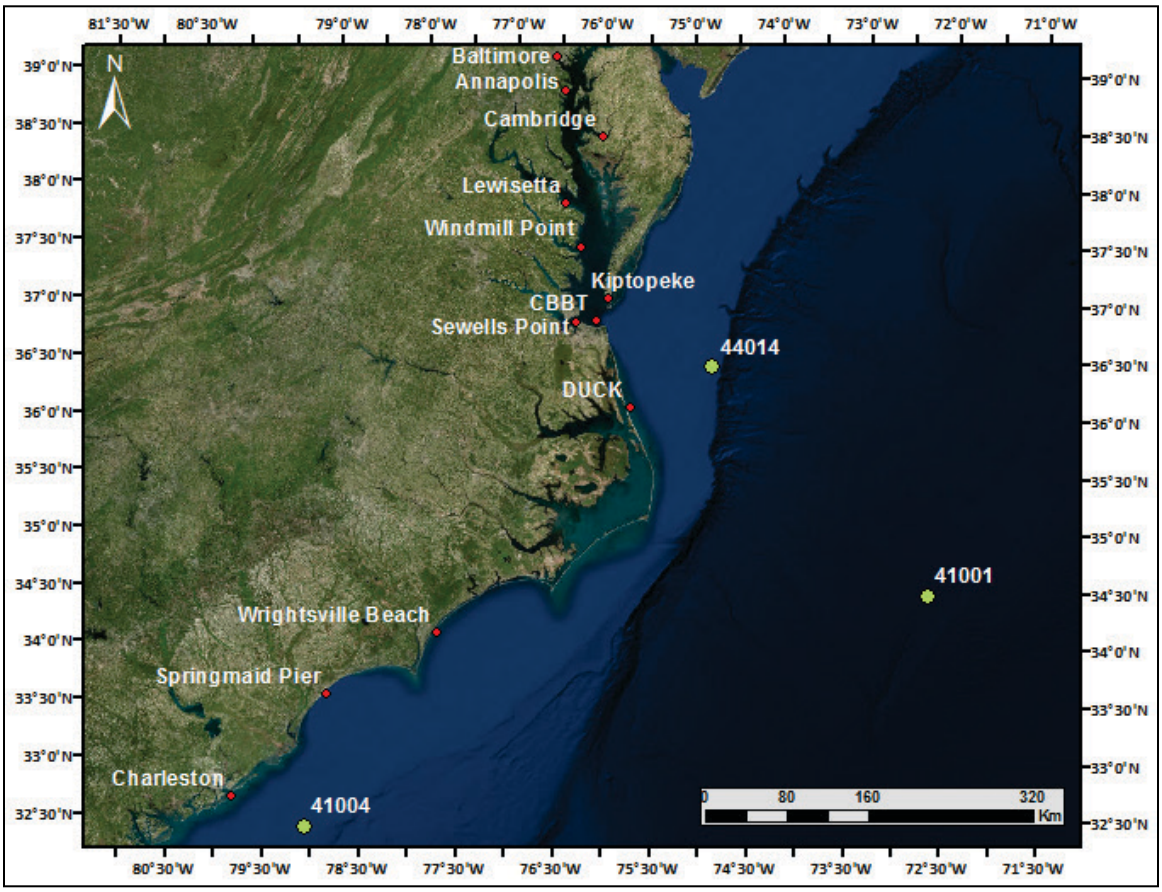

Figure 35: Locations of 12 NOAA tidal gauges (red dots) and 3 NDBC buoys (green dots) used in water elevation comparisons.

Table 3: Detailed information for NOAA tidal gauges and NDBC buoys.

Station ID	Station Name	Latitude	Longitude	Observation
NOAA-8574680	Baltimore, MD	39.2667	-76.5783	Water level
NOAA-8575512	Annapolis, MD	38.9833	-76.4801	Water level
NOAA-8571892	Cambridge, MD	38.5817	-76.0627	Water level
NOAA-8635750	Lewisetta, VA	37.9867	-76.4633	Water level
NOAA-8636580	Windmill Point, VA	37.6134	-76.2909	Water level
NOAA-8632200	Kiptopeke. VA	37.1650	-75.9883	Water level
NOAA-8638863	CBBT, VA	36.9709	-76.1056	Water level
NOAA-8638610	Sewells Point, VA	36.9434	-76.3331	Water level
NOAA-8651370	Duck, NC	36.1987	-75.7366	Water level
NOAA-8658163	Wrightsville Beach, NC	34.2133	-77.7867	Water level
NOAA-8661070	Springmaid Pier, SC	33.6550	-78.9183	Water level
NOAA-8665530	Charleston, SC	32.7344	-79.8292	Water level
NDBC-44014	44014	36.6110	-74.8430	Wave data
NDBC-41001	41001	34.6251	-72.6170	Wave data
NDBC-41004	41004	32.5010	-79.0991	Wave data

3.3.2. Tidal and Storm Tide Hindcast in Virginia, North Carolina, and South Carolina Coasts and inside Chesapeake Bay

Tidal calibration and harmonic analysis were conducted to ensure that SCHISM properly models long-wave propagation into Chesapeake Bay. With only tidal sinusoidal motion at the open ocean boundary, the large-scale SCHISM model was run without any wind forcing. Eight harmonic tidal constituents (M_2, N_2, S_2, K_2, O_1, P_1, K_1, and Q_1) were applied at the 60-degree West longitude boundary utilizing the ADCIRC Tidal Data Base. The tidal simulation spanned 90 days and started on July 1st 00:00 UTC through September 30th 00:00 UTC, 2011. Inside Chesapeake Bay, the Manning's value is set to 0.015. These values were consistent with previous study in the Chesapeake Bay (Gao, 2011). Twelve NOAA tidal gauges were utilized to verify model accuracy. The modeled tides match well with NOAA prediction at all 12 locations. Statistical values such as R^2, RMSE, and MAE were calculated and presented in Appendix 2 (2). SCHISM tidal simulation is accurate with R^2 values larger than 0.96 and average RMSE of 4-5 cm at all stations. At the upper Bay stations such as Baltimore and Cambridge, the error was slightly larger than at the middle and lower Bay stations due to the uncertainties of bathymetry. The harmonic analysis results of 5 major constituents' (M_2, N_2, S_2, O_1, and K_1) are shown in Appendix 2 (2).

Modeled storm tide from two simulations was compared with NOAA tidal gauge data at 6 locations along VA, NC, and SC coasts (Figure 36). The coupled model performed well at all stations according to the statistics calculations (Table 4) and could simulate the maximum storm tide with error on the order of 7-8 cm along VA and NC coasts. The average R^2 for all stations is 0.97, the average RMSE is 11 cm, and the

average MAE is 9 cm. The model results at Charleston and Springmaid Pier have ~5 cm larger error due to model not highly resolving the South Carolina coast. The WWMIII model's results (significant wave heights and peak wave periods) were also compared with NDBC observation at three stations off VA and NC coasts (Figure 37). The time series of comparisons confirm again that WWMIII model worked well with high quality ECMWF wind product. The average relative error of modeled wave height is around 10%, and the error in peak period is 1-3 seconds.

Table 4: Statistical evaluation of SCHISM with WWM modeled storm tide and NOAA observed water level at 6 stations along VA, NC, and SC coasts.

Stations	R^2	RMSE (m)	MAE (m)
Kiptopeke, VA	0.966	0.084	0.072
CBBT, VA	0.965	0.093	0.076
Duck, NC	0.960	0.110	0.089
Wrightsville Beach, NC	0.966	0.108	0.079
Springmaid Pier, SC	0.970	0.128	0.106
Charleston, SC	0.974	0.127	0.108

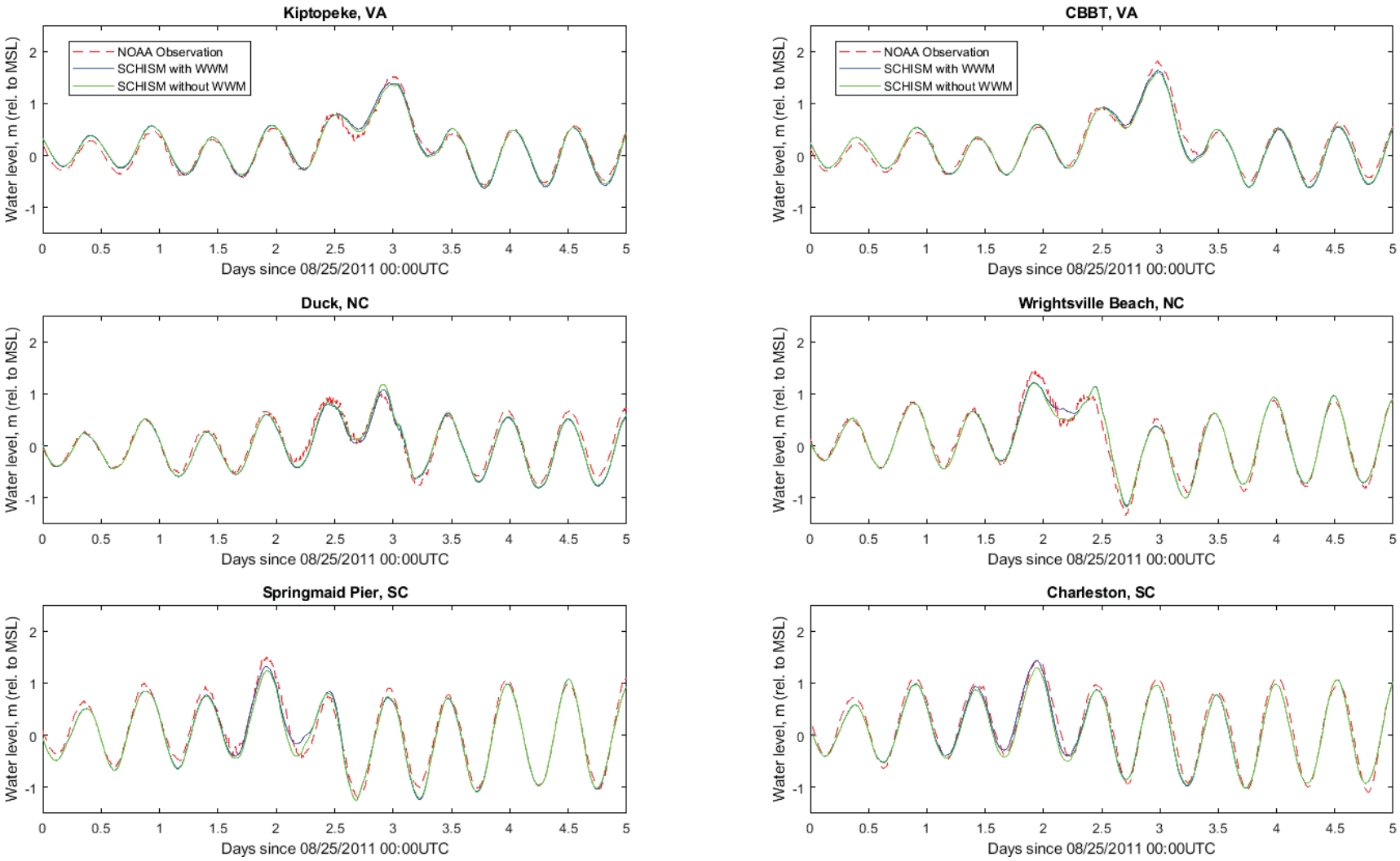

Figure 36: Time series of NOAA observation and SCHISM modeled storm tide results at 6 stations along VA, NC, and SC coasts.

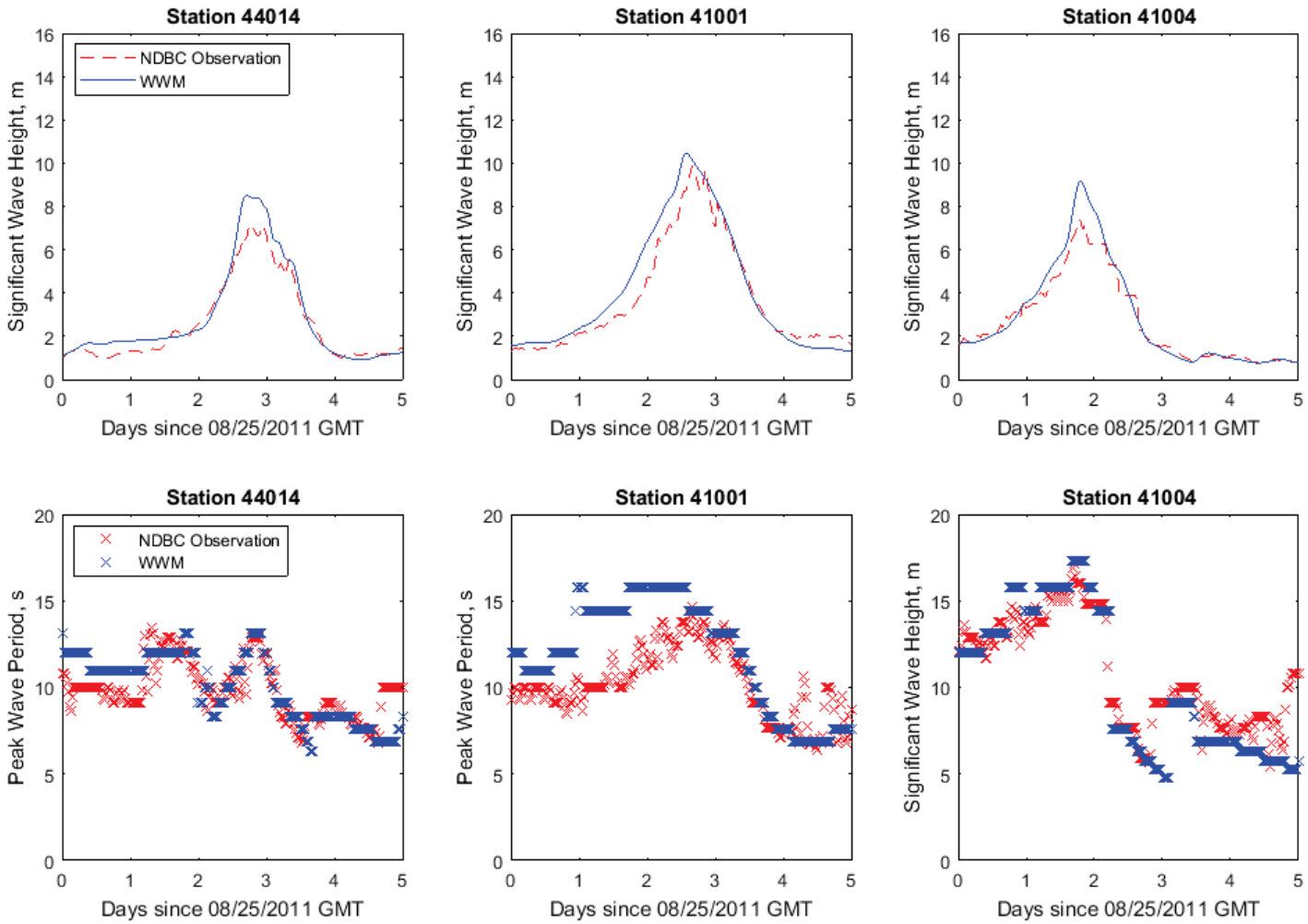

Figure 37: Time series of comparisons of NDBC observed wave data (significant wave heights and peak wave periods) and WWMIII results at 3 NDBC stations: 44014, 41001, and 4100

Modeled storm tide from two simulations was also compared with NOAA tidal gauge data at 6 locations inside Chesapeake Bay (Figure 38). Also, the coupled model has excellent results at all stations inside the estuary, which further proves the strong cross-scale capability of SCHISM. According to the statistics calculations (Table 5), the average R^2 and RMSE are 0.92 and 9 cm, respectively. The SCHISM model coupled with WWMIII was able to reasonably simulate the negative surge (reduced total water level) observed at Baltimore, MD, in the upper Chesapeake Bay (Figure 38). The error in upper Bay is slightly larger than other areas because the model's resolution is coarser to keep model reasonably efficient.

Table 5: Statistical evaluation of SCHISM with WWM modeled storm tide and NOAA observed water level at 6 stations inside Chesapeake Bay.

Stations	R^2	RMSE (m)	MAE (m)
Baltimore, MD	0.903	0.116	0.087
Cambridge, MD	0.913	0.080	0.065
Annapolis, MD	0.906	0.095	0.075
Lewisetta, VA	0.949	0.084	0.072
Windmill Point, VA	0.952	0.083	0.070
Sewells Point, VA	0.971	0.090	0.072

In summary, 3-D barotropic SCHISM storm tide model coupled with wind wave model WWMIII using ECMWF atmospheric forcing was also effectively applied in hindcasting water elevation during 2011 Hurricane Irene with very reasonable results along the southeast coast and inside Chesapeake Bay. From the overall comparison of water level, these two models (the coupled model and no-wave model) had similar performance in Chesapeake Bay, but the difference between them is larger along NC and SC coasts.

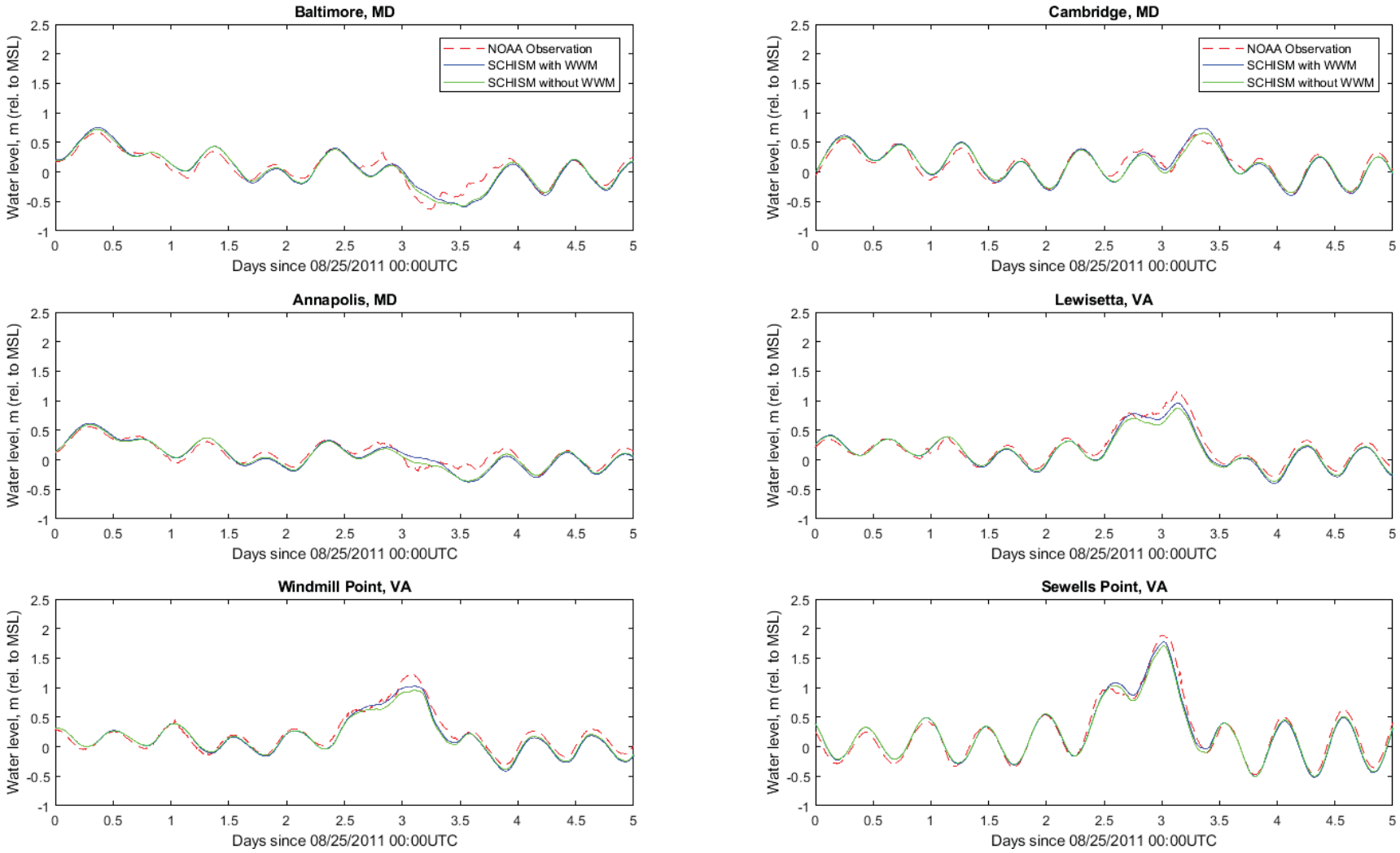

Figure 38: Time series of NOAA observation and SCHISM modeled storm tide results at 6 stations inside Chesapeake Bay.

3.3.3. Effects of Wind Wave

The time series of wave setup are plotted against modeled total water levels at each location along VA, NC, and SC coasts, and inside Chesapeake Bay (Figures 39 and 40). Along Southeast Coast, the magnitude of wave setup is smaller at two VA stations near the Bay mouth where they are near the deep channel. At Duck, NC, there was slight wave set-down of approximately 0.1 m. At the two stations along SC coast, the wave setup is larger than 0.2 m. In addition to the spatial variation, the timing of max wave setup also differs a lot. From the south (Charleston, SC) to the north (Kiptopeke, VA), the delay in phase is consistent with Irene's track which represents the direction of storm-induced wave propagation. Also, the peak setup didn't coincide with the peak water level.

Inside Chesapeake Bay, the magnitude of wave setup was similar at each station on the order of 0.07 - 0.1 m and the timing is consistent with phase delay from the Bay mouth (Sewells Point, VA) to the upper Bay (Baltimore, MD). Although the wave setup was smaller in the Bay, the relative weight of wave set up to the total water level increases upstream. Overall, the effects of wind wave were on the order of 5-15% at the stations along coastline and near the Bay mouth.

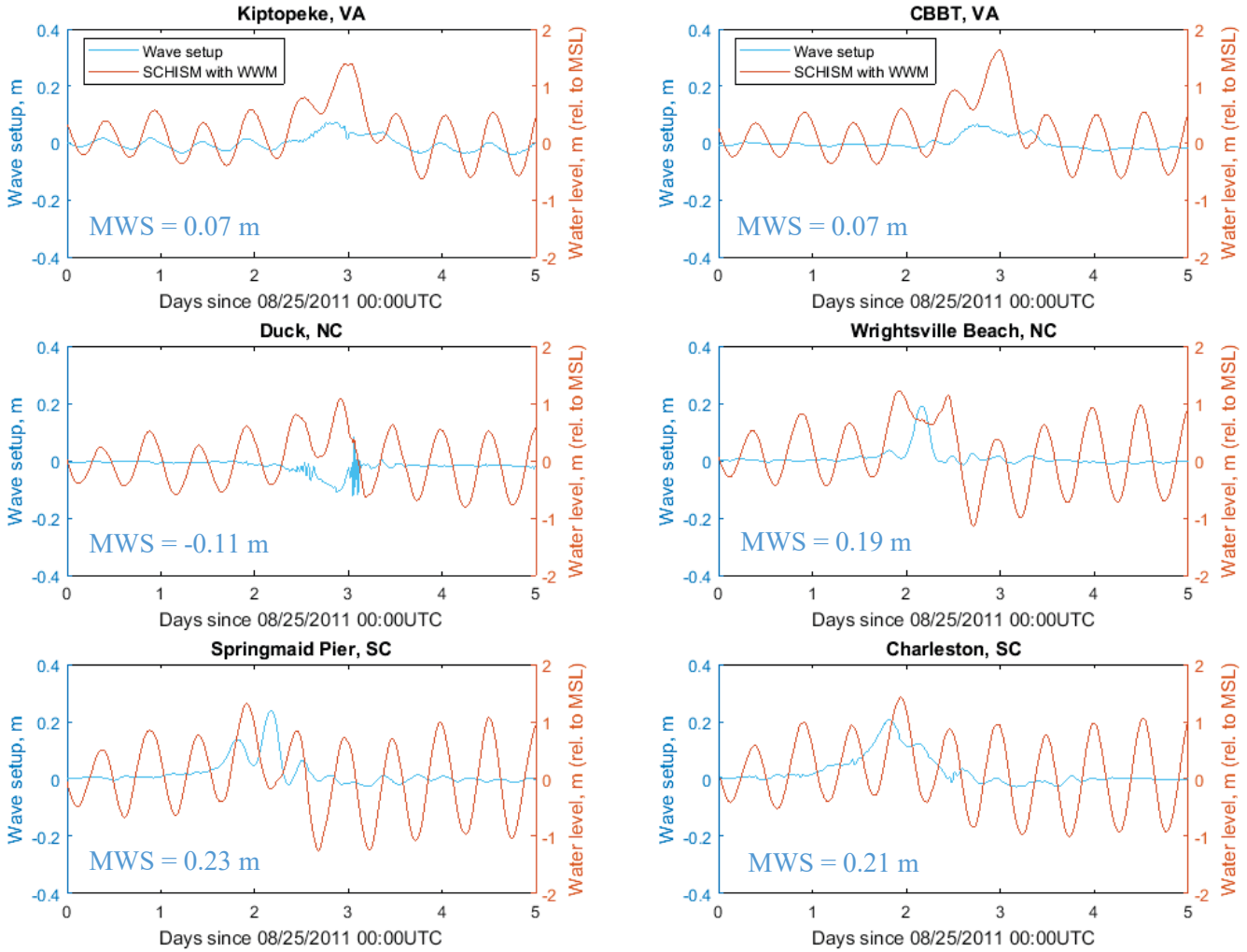

Figure 39: Time series of wave setup (blue) and storm tide (orange) from the coupled model at 6 stations along VA, NC, and SC coasts. Note that different scales for left and right y-axis. The Maximum Wave Setup/Setdown (MWS) is labeled in each Figure.

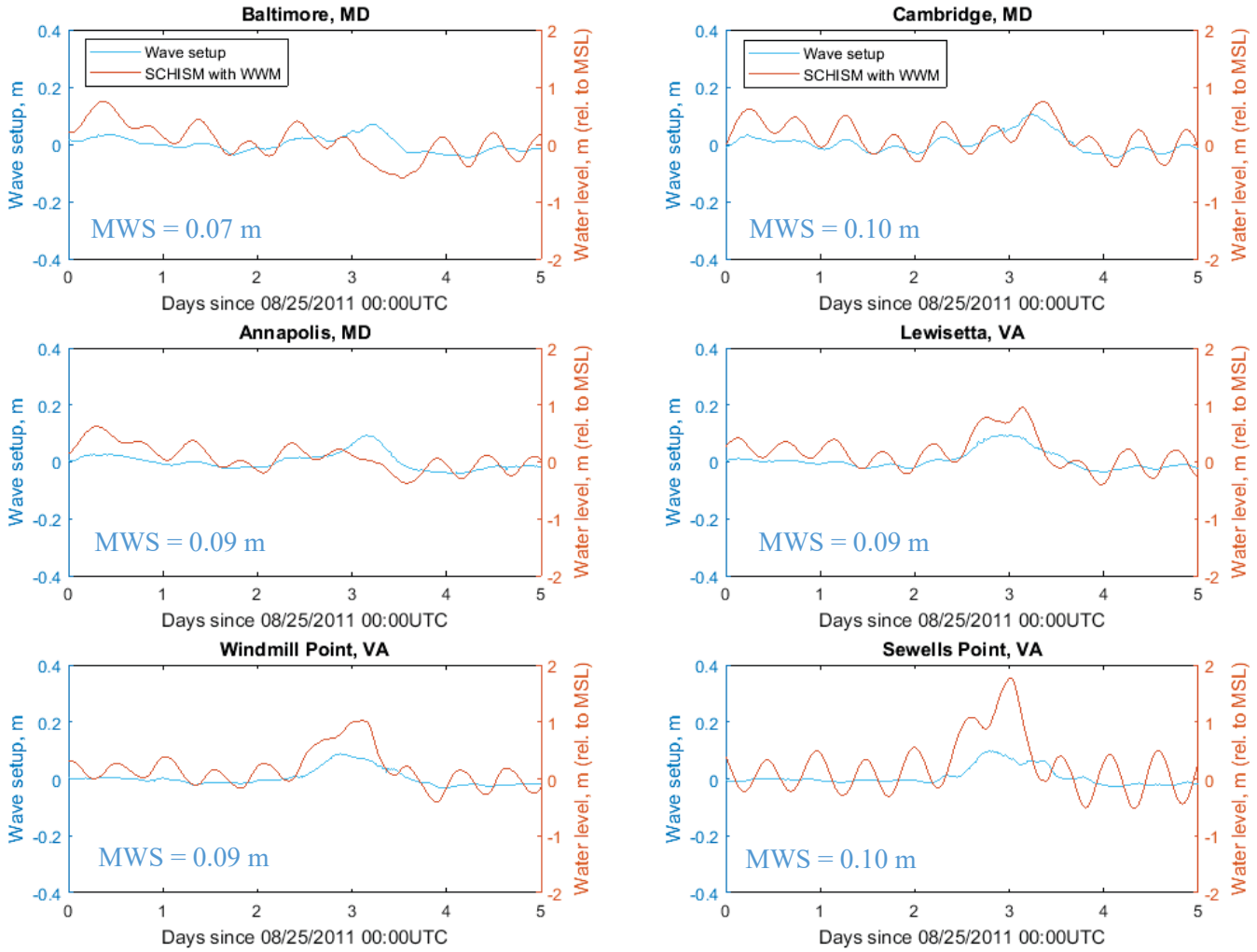

Figure 40: Time series of wave setup (blue) and storm tide (orange) from the coupled model at 6 stations inside Chesapeake Bay. Note that different scales for left and right y-axis. The Maximum Wave Setup/Setdown (MWS) is labeled in each Figure.

As Irene approached the SC coast around 8/27, since the depth changes dramatically from deep ocean to the SC and NC coasts (Figure 41), the significant wave heights (> 10 m) reduced quickly across shore (Figure 42), which generated large radiation stress gradient towards shore, and thus caused a larger wave setup of 0.2 m. The offshore wave height was the primary control on wave setup since it provided the energy available to produce setup. Later when the hurricane was directly passing through Duck, NC around 08/28, the local wind conditions changed quickly, which caused the conditions of the wind wave to vary rapidly during short periods, and thus high frequency fluctuations of the wave setup were observed here. In this area when the wave radiation stress gradient was pointing offshore, a minor wave set-down of 0.1 m was observed at this station.

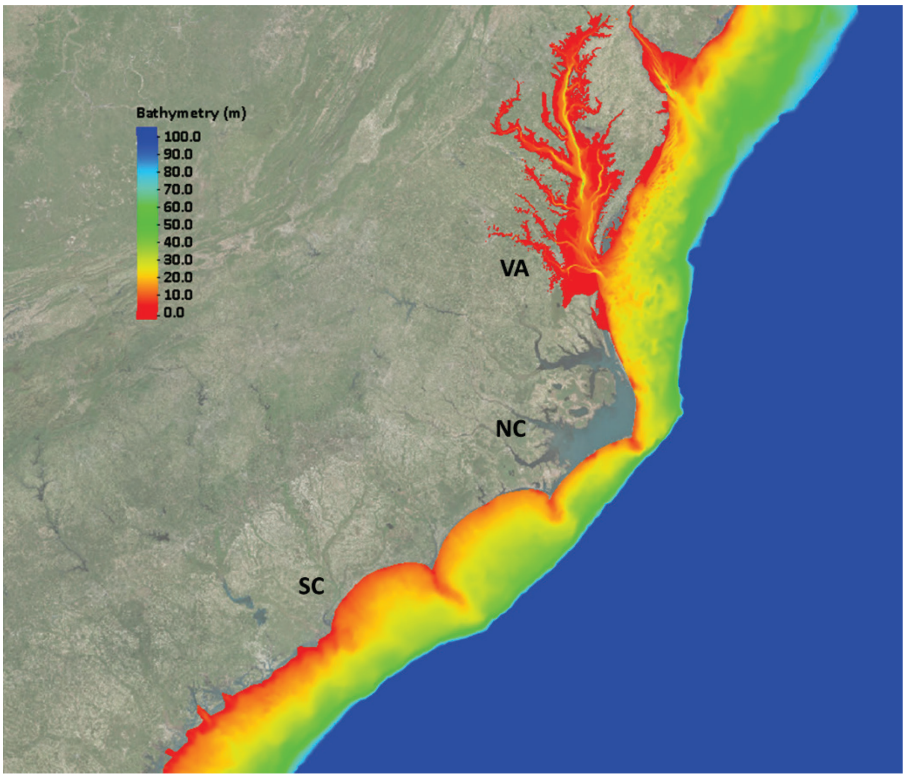

Figure 41: Model bathymetry in part of model domain.

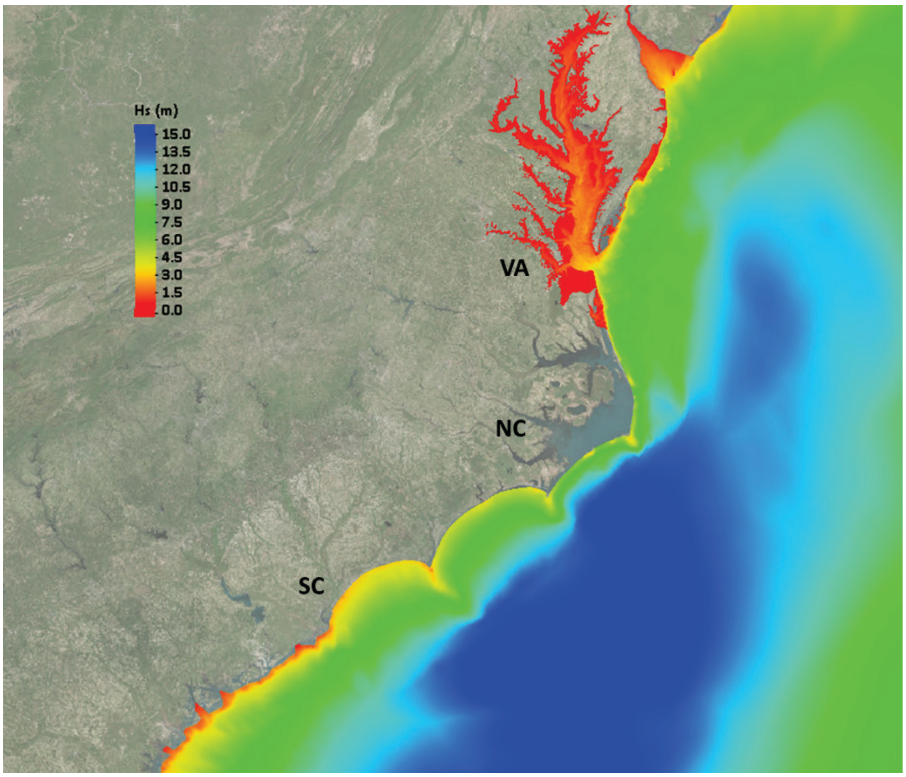

Figure 42: Maximum significant wave heights in VA, NC, and SC coasts.

After Irene passed the Bay mouth on 8/28, the wave traveling towards the upper Bay continued to break when entering the shallower regions (Figure 43). The maximum significant wave heights in Chesapeake Bay is shown in Figure 44. Stephens et al. (2011) demonstrated that wave setup is also highly influenced by the profile shape. Thus, the wave setup could differ substantially in space as the result of the variability of the cross-shore profile shape. Higher waves (2-3 m) were observed in the main stem of Chesapeake Bay due to deep channel. Around the Bay mouth, there was not much change in wave heights so the wave breaking as well as wave setup at CBBT and Kiptopeke was very small. When the wave entered the much shallower water in the lower James River, there was larger wave breaking (from 3 m to 1m) so a larger wave setup at Sewells Point was

observed. From middle-Bay to upper-Bay, the significant wave heights along the deep channel remained at a similar magnitude on the order of 2 m. The wave breaking cross shore was similar too so the wave setup from Windmill Point to Annapolis was on a similar order. However, near Baltimore, the wave height was already reduced to 1 m so the wave breaking and radiation stress gradient was very small at this station. As a result, the wave setup here was the smallest in the Bay.

Since Chesapeake Bay has a much larger spatial scale than the New York Bay, the effects of wind wave are both spatially and temporally varying. The wave setup is mainly driven by the significant waves offshore and the angle of breaking, but also by the shape of the estuaries and rivers. The momentum change caused by radiation stress from wave breaking is highly dependent on the slope and depth of the bottom, and its variation from site to site is considerable. During Hurricane Irene, the wave setup and the relative contribution to overall water levels varied throughout the study area including stations along the coast and in the estuary and rivers. In general, the absolute value of wave set up is smaller in the estuary than along the coast; however, the contribution of wave setup is more significant (relative to the total water level) in the upper estuary. In terms of the wave setup on maximum storm tide by Hurricane Irene, it was mostly less than 0.1 m (Figure 45), smaller than what we observed during Hurricane Sandy.

This analysis suggests that the effects of wave radiation stress gradients in larger estuaries and their tributaries are much more complicated than a small-size estuary. The effects were spatially and temporally varying because of the difference in bathymetry and geometry. To fully study the coupled wave-current dynamics inside a large estuary like Chesapeake Bay, more studies of different hurricanes with different tracks are warranted.

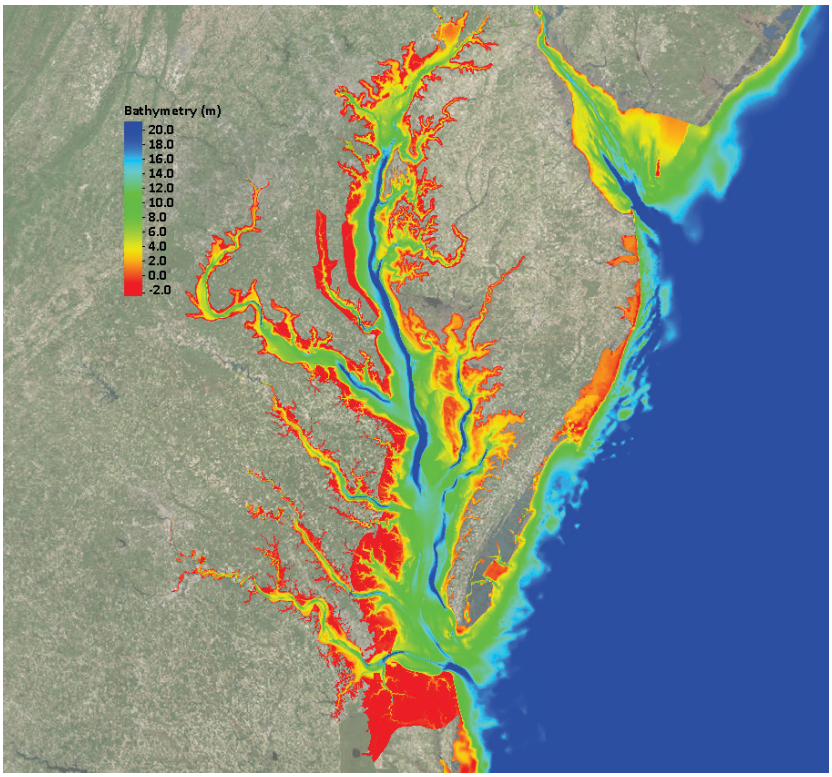

Figure 43: Model bathymetry (m) in Chesapeake Bay.

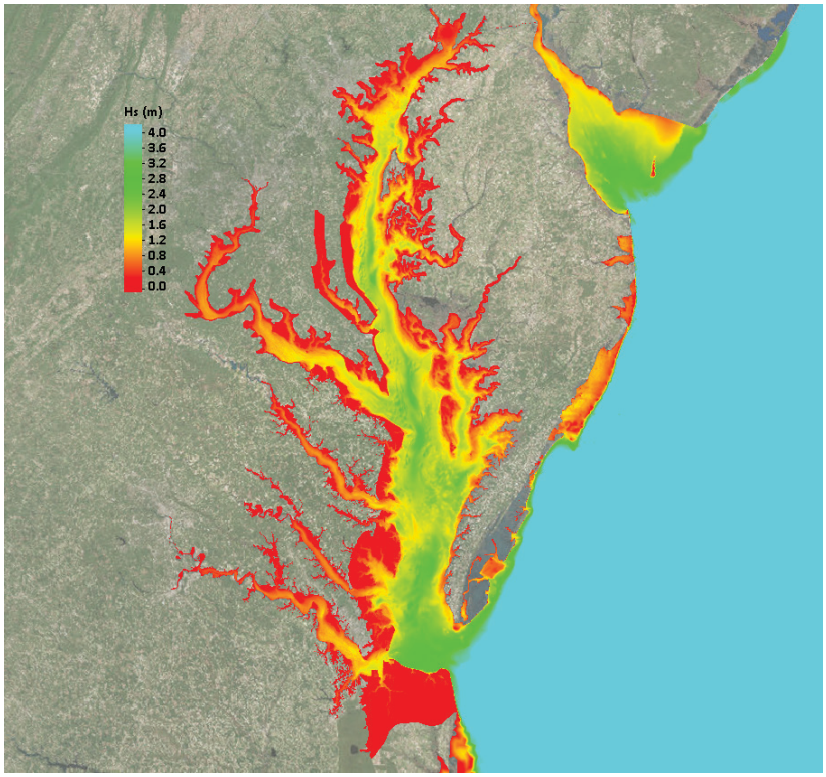

Figure 44: Maximum significant wave heights in Chesapeake Bay.

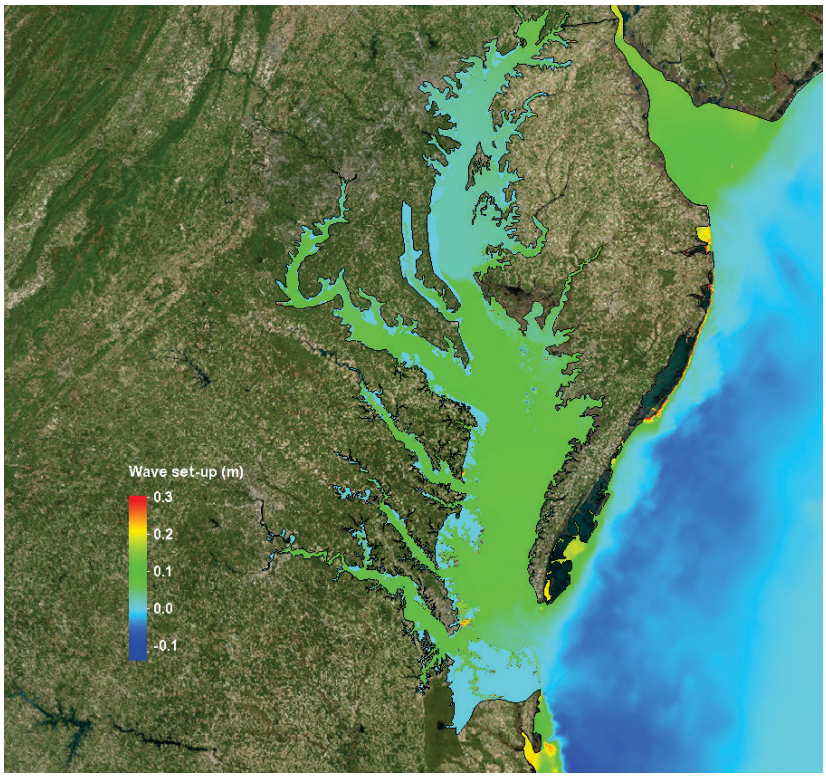

Figure 45: Wave setup on the maximum storm tide elevation in Chesapeake Bay.

CHAPTER 4. High-Resolution Sub-Grid Coastal Inundation Model – ELCIRC-sub

The second part of my dissertation is to address the coastal inundation modeling, as stated in my research objectives (Chapter 1.2). The challenge of the modeling coastal inundation compared to that of storm surge is that the former involved the water moving across land boundary onto the land while the latter is mainly water moving across different water bodies such as ocean and estuaries. The land surface upon which the inundation water is moving through is notoriously complicated such as water front berms, walkways, streets, building, factories, trees, railroads, parks, highways, to name a few, which can cause various scales and types of fluid motions. Therefore, it requires a much smaller scale of grid, to resolve motions from the smallest scale possible to full system level of scale. One of the main principles used in hydrodynamics to deal with the complicated flow pattern is to apply the conservation of mass and momentum onto each control volume and, by keeping track the flux in and out of the control volume, one can calculate the variation of the water volume over time. In this context, a flux-based, finite volume model ELCIRC (Eulerian-Lagrangian Circulation), was naturally chosen to implement the inundation modeling.

4.1. Description of ELCIRC Model

ELCIRC is an unstructured-grid model designed for the effective simulation of 3D baroclinic circulation across river-to-ocean scales. It was developed by Zhang et al. (2004). It uses a finite-volume/finite-difference Eulerian-Lagrangian scheme to solve the shallow water equations and realistically address a wide range of physical processes under atmospheric, ocean and river forcings. ELCIRC is governed by a set of equations that represent mass, momentum, salt and heat conservation, and is solved to obtain free surface water elevation, 3-D velocity, salinity, and temperature. Two main governing equations in the ELCIRC model include continuity equation (1) and momentum equations (2a, 2b) are shown as follows:

$$\frac{\partial u}{\partial x}+\frac{\partial v}{\partial y}+\frac{\partial w}{\partial z}=0 \qquad \Rightarrow \qquad \frac{\partial \eta}{\partial t}+\frac{\partial}{\partial x}\int_{H_R-h}^{H_R+\eta} u dz+\frac{\partial}{\partial y}\int_{H_R-h}^{H_R+\eta} v dz=0 \tag{1}$$

$$\frac{Du}{Dt}=fv-\frac{\partial}{\partial x}\left\{g(\eta-\alpha\hat{\psi})+\frac{P_a}{\rho_0}\right\}-\frac{g}{\rho_0}\int_z^{H_R+\eta}\frac{\partial \rho}{\partial x}dz+\frac{\partial}{\partial z}(K_{mv}\frac{\partial u}{\partial z})+F_{mx} \tag{2a}$$

$$\frac{Dv}{Dt}=-fu-\frac{\partial}{\partial y}\left\{g(\eta-\alpha\hat{\psi})+\frac{P_a}{\rho_0}\right\}-\frac{g}{\rho_0}\int_z^{H_R+\eta}\frac{\partial \rho}{\partial y}dz+\frac{\partial}{\partial z}(K_{mv}\frac{\partial v}{\partial z})+F_{my} \tag{2b}$$

where

(x, y)	horizontal Cartesian coordinates, (m)
z	vertical coordinate, positive upward, (m)
t	time, (s)
H_R	z-coordinate at reference level (geoid or mean sea level (MSL))
$\eta(x, y, t)$	free-surface elevation, (m)
$h(x, y)$	bathymetric depth, (m)
f	Coriolis factor, (s^{-1})
g	acceleration of gravity, (ms^{-2})
ψ	tidal potential, (m)

α	effective Earth elasticity factor (~0.69)
$\rho(x,t)$	water density; by default, reference value is set as 1025 kgm^{-3}
$P_a(x,y,t)$	atmospheric pressure at the free surface (Nm^{-2})
K_{mv}	vertical eddy viscosity, (m^2s^{-1})
F_{mx}, F_{my}	horizontal diffusion for momentum

Given the coupled governing equations, it was first solved by combining continuity and the vertically-averaged momentum equation into a single elevation equation via a conjugate gradient solver. The 3-D momentum equation was then solved with the known water elevation and an Eulerian-Lagrangian-based scheme for the advection terms (Casulli and Cheng, 1992; Casulli and Zanolli, 1998). The algorithm of ELCIRC has been shown to be efficient, reliable, mass conservative, and is capable of modeling wetting and drying process in near-shore areas. For a coastal inundation simulation, the robust treatment of wetting and drying originally retained in ELCIRC is a great asset ready to be further improved with the sub-grid method on simulating inundation over the land.

In this dissertation, a new technique called sub-grid modeling will be introduced and built into this model. The emerging of sub-grids was enabled by 1-5 m resolution LIDAR data and the total number of grid was pushed to an unpreceded level. This plus the fact that a sizable land watershed domain contributing to the flooding water will now be included as part of the model domain, not only the waterway. Thus, having a parallel computing capability built into ELCIRC along with sub-grid modeling becomes an essential part of strategy.

4.2. Description of Sub-Grid Techniques

The sub-grid method deals with two grids, a coarse computation grid and an underlying sub-grid with a higher resolution. The basic idea of sub-grid modeling is the use of available high-resolution bathymetric data at the sub-grid level while performed computations at relatively coarse grids allowing large time steps, enhanced accuracy and efficiency (Casulli, 2009 and Casulli and Stelling, 2010). The computational grid (also called base grid) is made of flow-aligned quadrilaterals while the sub-grids divide base computational grid into smaller equal parts to allow a detailed boundary fitting at sub-grid level. Essentially, the sub-grid modeling is an innovative method by which water elevation and velocity on the high-resolution sub-grid level can be obtained through the combination of elevations, velocities, and integrated friction calculated at the coarse computational grid without employing the computing resources to solve the full set of equations. Furthermore, depending upon DEM (Digital Elevation Model) resolution a sub-grid cell nested within base grid cell can carry information of LIDAR topography, bathymetry, bottom friction back to the computational grid level based on the conveyance approach (Casulli and Stelling, 2011).

For every computational edge, a set of sub-edges, each with one length and one depth (depth classes of the sub-edges), is created. Similarly, for every computational polygon, a set of sub-polygons, each with one area and one depth (depth classes of sub-polygons), is created. The number of depth classes may vary for each polygon or edge. User-defined grid subdivision at sub-grid level allows a correct representation of the volume up to measurement accuracy of LIDAR data. An example of sub-grid setup in Manhattan, New York City was shown in Figure 46, which demonstrates capability of the

sub-grid to resolve shoreline, the offshore structures, water front properties, the building in the city, and the streets connecting them amazingly well. The sub-grid also has the advantage in sub-dividing the cross-section of the channels into smaller separate sub-sections to better estimate the cross-sectional area. They help to sub-divide the river and creek cross-section into smaller separate areas and sum them up in a manner analogous to the calculus in better estimating the area underneath the curve (Figure 47). As a result, the accuracy of the total volume transport of the flood water as the sum of the product of perpendicular velocities to each of the cross-section area, is greatly enhanced.

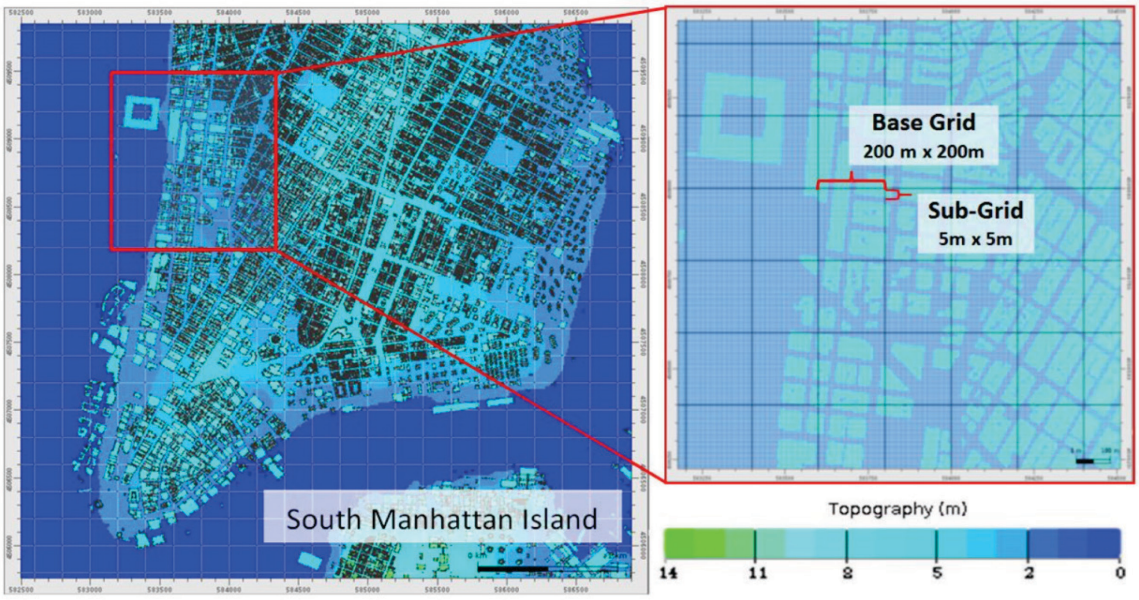

Figure 46: Representation of the square sub-grid used for modeling Hurricane Sandy in New York City on the southern tip of Manhattan Island. LIDAR-derived topography data are directly imported into the square sub-grid elements to effectively resolve buildings and streets.

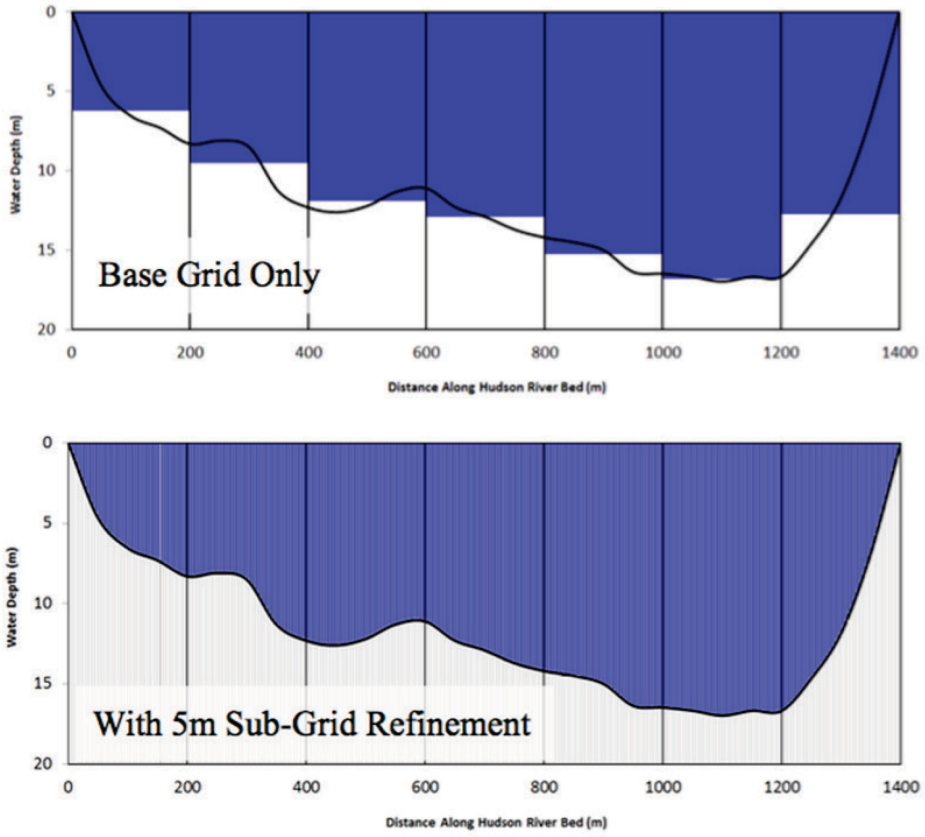

Figure 47: The transect across the Hudson River bed is shown at the 200-m base grid resolution without sub-grid refinement (top), and with 5-m sub-grid refinement (bottom).

The sub-grids, in the form of raster DEM derived from LIDAR and high-resolution bathymetry, is nested within the base computational grid cell to allow the fine-scale topography features to be recognized. To do so, an interpolation function "subdepth" is written in "misc_sub.F90" in ELCIRC-sub source code (Figure 48) to transform high-resolution bathymetry and topography data into sub-grid level. The center coordinate (x,y) of each sub-grid element is used as input of this function and the corresponding output is depth at the center of each sub-grid cell.


```
dx=dxy                                                                                                  1
dy=dxy                                                                                                  2
   Interpolate                                                                                          3
 if(x.gt.xmax.or.x.lt.xmin.or.y.gt.ymax.or.y.lt.ymin) then                                              4
    dp=dp0 !keep original                                                                               5
 else !inside structured grid                                                                           6
    x2=x                                                                                                7
    y2=y                                                                                                8
    ix=(x2-xmin)/dx+1 !i-index of the lower corner of the parent box                                    9
    iy=(y2-ymin)/dy+1                                                                                   10
    if(ix.lt.1.or.ix.gt.nx.or.iy.lt.1.or.iy.gt.ny) then                                                 11
      write(errmsg,*) 'Impossible:',x,y,ix,iy                                                           12
      call parallel_abort(errmsg)                                                                       13
    endif                                                                                               14
                                                                                                        15
    if(ix.eq.nx) then !for pts right on the right bnd                                                   16
      ix=nx-1                                                                                           17
      xrat=1                                                                                            18
    else                                                                                                19
      xrat=(x2-xmin)/dx-ix+1                                                                            20
    endif                                                                                               21
    if(iy.eq.ny) then !for pts right on the upper bnd                                                   22
      iy=ny-1                                                                                           23
      yrat=1                                                                                            24
    else                                                                                                25
      yrat=(y2-ymin)/dy-iy+1                                                                            26
    endif                                                                                               27
    if(xrat.lt.0.or.xrat.gt.1.or.yrat.lt.0.or.yrat.gt.1) then                                           28
      write(errmsg,*) 'ratios out of bound:',xrat,yrat                                                  29
      call parallel_abort(errmsg)                                                                       30
    endif                                                                                               31
                                                                                                        32
    if(abs(dp_dem(ix,iy)-fill_value)<1.e-2.or.abs(dp_dem(ix+1,iy)-fill_value)<1.e-2.or. &               33
&abs(dp_dem(ix,iy+1)-fill_value)<1.e-2.or.abs(dp_dem(ix+1,iy+1)-fill_value)<1.e-2) then                 34
      dp=dp0 !keep original                                                                             35
    else !all valid                                                                                     36
      hy1=dp_dem(ix,iy)*(1-xrat)+xrat*dp_dem(ix+1,iy)                                                   37
      hy2=dp_dem(ix,iy+1)*(1-xrat)+xrat*dp_dem(ix+1,iy+1)                                               38
      h=hy1*(1-yrat)+hy2*yrat                                                                           39
      dp=h*ih+vshift                                                                                    40
    endif !junk                                                                                         41
 endif                                                                                                  42
```

Figure 48: "subdepth" function used to interpolate high-resolution DEM onto sub-grid cells. Line number of code is shown on the right.

In the base grid and sub-grid framework, the core computation for solving the shallow water equations is performed on the base grid. Once the base grid finishes the calculations, the elevation on each sub-grid cell can be bi-linearly interpolated from the base grid elevation. Together with the bathymetry within each of the sub-grids, the total water depth of each sub-grid and the status of its wetting (or drying) can be determined.

Once the depth and the wetting and drying of each individual sub-grid are decided, the wetting, drying and/or partial wetting-and-drying of the "base grid" can then be determined collectively by the distribution of the sub-grid population within that base grid. Attributed to the sub-grid approach, it is important to recognize that the partial wetting-and-drying of the base computational grid, which is unavailable by the traditional method, is now possible to more accurately determine the extent, depth, and timing of the inundation.

4.3. Development of ELCIRC-sub Model

4.3.1. Nonlinear Solver

As shown by Aldrighetti and Zanolli (2005), the semi-implicit finite volume discretization of an open channel with arbitrary cross-section is a nonlinear system. It is non-linear because variation of volume co-varies with both cross-section area and the water level. If the wall of the cross-section is at a right angle to the bottom surface, then variation of volume to the water level is linear. Otherwise, any oblique angle of the wall (to the bottom surface) will lead to a nonlinear relationship between volume and water elevation, as shown in Figure 49. Based on Casulli (2009)'s study, assuming a domain $\Omega(t)$ is covered by an unstructured orthogonal grid consisting of Np non-overlapping convex polygons Ωi, i= 1, 2, … Np, each side of a polygon is either a boundary line or a side of an adjacent polygon. Within each polygon a center must be identified in such a way that the segment joining the centers of two adjacent polygons and the side shared by the two polygons, have a nonempty intersection, and are orthogonal to each other (Figure 50).

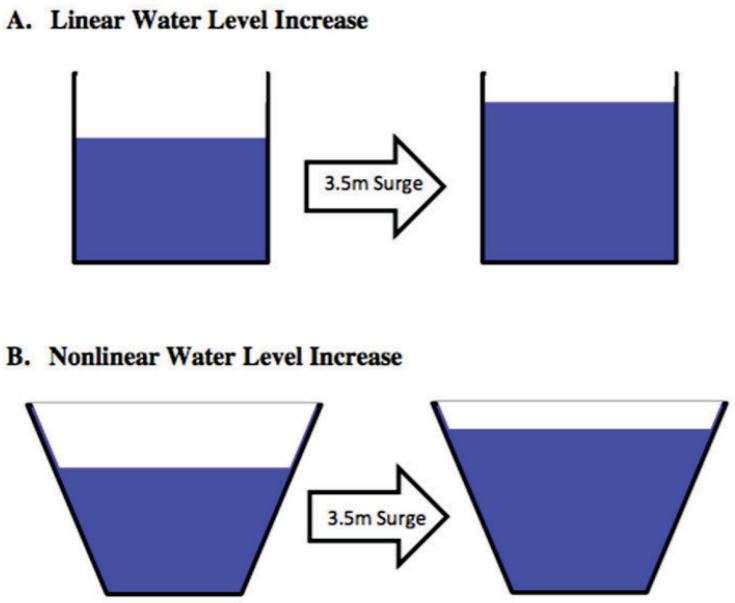

Figure 49: Depiction (A) linear vs. (B) nonlinear relationship between water level and volume changes.

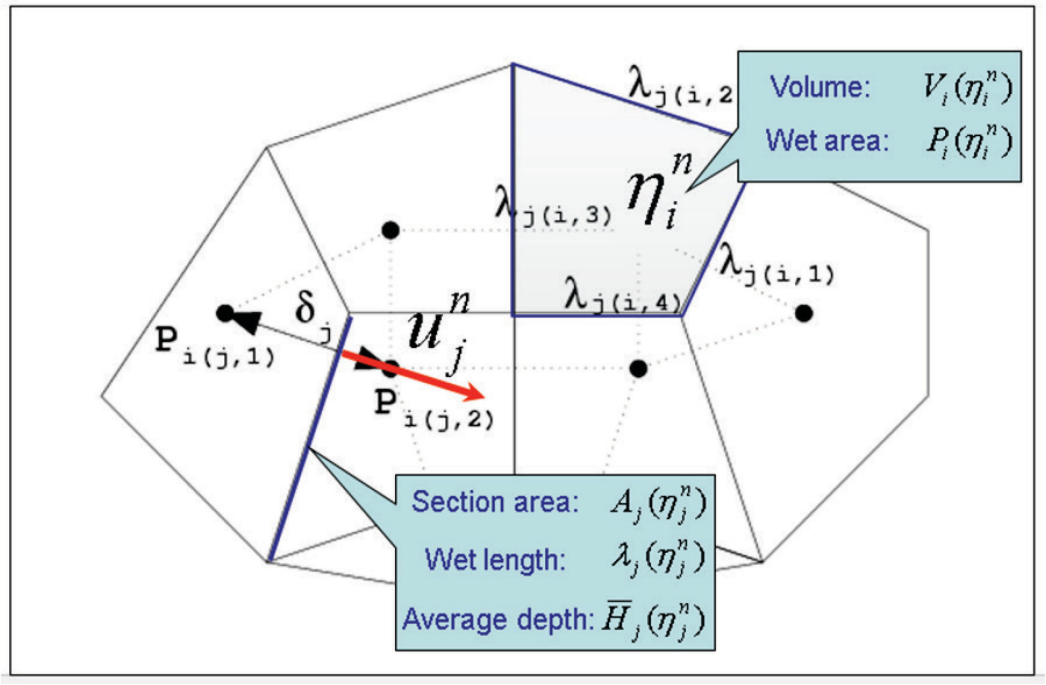

Figure 50: An example of part of model domain including labels of area, volume, and depth.

Given Ω is covered with an unstructured orthogonal grid, each polygon Ωi may have an arbitrary number of sides Si ≥ 3. Let Ns be the total number of sides in the grid, and let λj , j =1,2, . . . , Ns be the length of each side. The sides of the ith polygon are identified by an index j(i,l) so that 1 ≤ j(i, l) ≤ Ns, l =1,2, . . . , Si. Similarly, the two polygons that share the jth side of the grid are identified by the indices i(j,1) and i(j,2) so that 1≤ i(j,1) ≤ Np and 1 ≤ i(j,2) ≤ Np. Let Pi be the area of the ith polygon. Moreover, n(i, l) denotes the neighbor of polygon i that shares the side j(i, l) with the ith polygon, hence 1 ≤n(i,l) ≤ Np, l =1,2, . . . , Si. The nonzero distance between the centers of two adjacent polygons which share the jth side is denoted with δj. The discrete velocities and water surface elevation are defined at staggered locations as follows. The water surface elevation assumed to be constant within each polygon, is located at the center of the ith polygon; the velocity component normal to the jth edge is defined at the intersection between the edge and the segment joining the centers of the two polygons which share the edge.

To explain how the nonlinearity arises mathematically, the core of sub-grid method is discussed below. In the presence of wetting and drying, use of a fixed unstructured grid alone is insufficient for fitting boundaries because the boundary is itself moving and unknown a priori. To overcome this difficulty, and for any specified sub-grid bathymetry $h(x,y)$ and to exactly represent the free-surface area, a porosity function $p(x,y,z)$ is defined as:

$$p(x,y,z)=\begin{cases}1 & if\ h(x,y)+z>0\\ 0 & elsewhere\end{cases} \qquad (3)$$

Within each polygon i having an area P_i, the horizontal integral of the porosity evaluated at the free surface $z=\eta_i^n$ at time step n is given by:

$$p_i(\eta_i^n) = \int_{\Omega_i} p(x, y, \eta_i^n) dxdy \tag{4}$$

Equation (4) implies that $p_i(\eta_i^n)$ is nonnegative, nondecreasing, and bounded. When $p_i(\eta_i^n)$ is zero, the polygon is dry; when $p_i(\eta_i^n) = P_i$, it is wet; and when $0 < p_i(\eta_i^n) < P_i$, the polygon is partially wet. So, the water volume V_i within the ith polygon can be expressed either as a horizontal integral of the water depth or as a vertical integral of the surface wet area p_i:

$$V_i(\eta_i^n) = \int_{-\infty}^{\eta_i^n} p_i(z) dz = \int_{\Omega_i} H(x, y, \eta_i^n) dxdy \tag{5}$$

where $H(x, y, \eta_i^n)$ is the total water depth: $H(x, y, \eta_i^n) = \max[0, h(x, y) + \eta_i^n]$. Hence, if $V_i(\eta_i^n) > 0$, then necessarily $p_i(\eta_i^n) > 0$. Thus, this equation induces the nonlinearity of the sub-grid method. The water volume is no more a linear function of the water depth given that the latter varies with the prescribed sub-grid depth $h(x, y)$ inside a computational polygon. This is particularly true when the polygon is partially wet. In dry polygons, the volume is zero; in fully wet polygons, the volume becomes a linear function of water depth. To express the relation between V_i^n *and* η_i^n, the equations (1), (2a) and (2b) are vertically integrated as:

$$\frac{\partial H}{\partial t} + \frac{\partial (H u)}{\partial x} + \frac{\partial (H v)}{\partial y} = 0 \tag{6}$$

$$\frac{\partial u}{\partial t} + u\frac{\partial u}{\partial x} + v\frac{\partial u}{\partial y} - fv = -g\frac{\partial \eta}{\partial x} + \mu\left(\frac{\partial^2 u}{\partial x^2} + \frac{\partial^2 u}{\partial y^2}\right) - \frac{\gamma}{H}u \tag{7a}$$

$$\frac{\partial v}{\partial t} + u\frac{\partial v}{\partial x} + v\frac{\partial v}{\partial y} + fu = -g\frac{\partial \eta}{\partial y} + \mu\left(\frac{\partial^2 v}{\partial x^2} + \frac{\partial^2 v}{\partial y^2}\right) - \frac{\gamma}{H}v \tag{7b}$$

where $H(x, y, t)=h(x, y)+ \eta(x, y, t)$ is the total water depth, $\eta(x, y, t)$ is the water surface elevation measured from the undisturbed water surface and $h(x, y)$ is a bounded function representing the prescribed bathymetry; $u(x, y, t)$ and $\upsilon (x, y, t)$ are the vertically averaged velocity components in the horizontal x- and y-directions, respectively; t is the time; f is the Coriolis parameter; g is the gravitational acceleration; v is a nonnegative coefficient of eddy viscosity; and γ is a nonnegative bottom friction coefficient, which can be given by the Manning–Chezy formula. In these equation, the water surface elevation in the momentum equation and velocity in the vertically integrated continuity equation, are discretized by the θ –method. Using the semi-implicit finite volume method, the velocity component normal to each edge can be written as

$$H_j^n u_j^{n+1} = H_j^n G_j^n - \theta g H_j^n \frac{\Delta t}{\delta_j}[\eta_{i(j,2)}^{n+1} - \eta_{i(j,1)}^{n+1}] - \Delta t \gamma_j^n u_j^{n+1} \tag{8}$$

where the positive direction for u_j^n has been chosen to be from $i(j,1)$ to $i(j,2)$; G_j^n is an explicit finite difference operator that accounts for the explicit contributions from the discretization of the Coriolis, advection, viscosity and hydrostatic pressure. Upon integrating the continuity equation, the volume within each polygon can be written as:

$$V_i(\eta_i^{n+1}) = V_i(\eta_i^n) - \Delta t \sum_{\ell=1}^{\vartheta_i} s_{i,\ell} A_{j(i,\ell)}^n [\theta u_{j(i,\ell)}^{n+1} + (1-\theta) u_{j(i,\ell)}^n] \tag{9}$$

Where $V_i(\eta_i^n)$ is the water volume in the ith water column delimited by the surface elevation η_i^n, surface wet area $A_j^n = A_j(\eta_j^n)$, and $s_{i,l}$ is a sign function associated with the orientation of the normal velocity defined on the lth side of polygon i.

Since “volume” is introduced in the integral of continuity equation, the semi-implicit finite volume formulation for the combined momentum and continuity equations

eventually leads to the mildly nonlinear system in Equation (10). The nonlinearity is residing in the definition of the water volumes $V_i(\eta_i^{n+1})$.

$$\begin{aligned} & V_i(\eta_i^{n+1}) - g\Delta t^2\theta^2 \sum_{l=1}^{S_i} \frac{\lambda_{j(j,l)}}{\delta_{j(j,l)}} \left(\frac{H^2}{H+\Delta t\gamma}\right)_{j(i,l)}^{n} (\eta_{n(i,l)}^{n+1} - \eta_i^{n+1}) \\ & = V_i(\eta_i^n) - \Delta t \sum_{l=1}^{S_i} s_{i,l}\lambda_{j(i,l)} H_{j(i,l)}^{n} \left[\theta \frac{HG}{H+\Delta t\gamma} + (1-\theta)u\right]_{j(i,l)}^{n} \end{aligned} \quad \text{, i=1, 2, …, Np} \qquad (10)$$

where Δt is the time step and θ is an implicitness factor to be taken in the range [0.5, 1]. γ is the edge-averaged bottom friction coefficient, and $s_{i,l}$ is a sign function associated with the orientation of the normal velocity defined on the lth side of polygon i. G is an explicit finite difference operator that accounts for the explicit contributions from the discretization of the Coriolis, advection, viscosity and hydrostatic pressure.

In a compact matrix notation, the equation can be expressed as a nonlinear equation of η_i^n:

$$V(\zeta) + T\zeta = b \qquad (11)$$

Where

$$\zeta = \begin{bmatrix} \eta_1^{n+1} \\ \eta_2^{n+1} \\ \vdots \\ \eta_{N_\eta}^{n+1} \end{bmatrix}, \quad V(\zeta) = \begin{bmatrix} V_1(\zeta_1) \\ V_2(\zeta_2) \\ \vdots \\ V_{N_\eta}(\zeta_{N_\eta}) \end{bmatrix}$$

where V is water volume at ith polygon, T is a sparse and symmetric $N_\eta \times N_\eta$ matrix that arises from the second term on the left-hand side of Equation (10) and b is a vector with N_η elements given by the right-hand sides of Equation (10).

Equation (11) is proven to have a unique solution (Casulli, 2009; Casulli and Zanolli, 2012). An efficient Newton-type algorithm for solving system (11) can be given by:

$$\zeta^{m+1} = \zeta^{m} - [P(\zeta^{m}) + T]^{-1}[V(\zeta^{m}) + T\zeta^{m} - b], \quad \text{m=0, 1, 2, …} \qquad (12)$$

where m now denotes the iteration index (not time step) and $P(\zeta^{m})$ is a diagonal matrix whose diagonal entries are the surface wet areas $p_i(\zeta_i^{m})$. Equation (12) is proven to be converged to the exact solution of system (11) (Casulli, 2009). From a practical point of view, since $P(\zeta^{m}) + T$ is a symmetric M-matrix, it is positive definite. Reorganizing Equation (12) yields Equation 13,

$$[P(\zeta^{m}) + T]\zeta^{m+1} = P(\zeta^{m})\zeta^{m} - V(\zeta^{m}) + b \text{ , m=0, 1, 2, …} \qquad (13)$$

of which each iteration can be efficiently performed by using a conjugate gradient method (Casulli, 2009). The Newton method is a powerful technique for solving non-linear equations by linearizing the original equation and has the properties of quadratic convergence if current iteration variable specified is sufficiently close to the convergence solution. Standard algorithm put the nonlinear iteration that generates the sequence of ζ^{m} in the outer iteration and the linear iteration that generates the approximation in the inner iteration. As a result, a properly coded ELCIRC-sub model that includes the non-linear wetting and drying algorithm has been accomplished.

Part of the Fortran 90 code of new iterative nonlinear solver versus the linear solver is presented in Figure 51. The nonlinear solver can be turned on/off by setting flag "nonlinear_solver=1 or 0" (Line 1 and Line 12 in Figure 51). Within the new nonlinear solver, the Newton-type algorithm is shown to converge to the exact solution in a finite

number given the bathymetry is a piece-wise constant function while conjugate gradient method is an algorithm for the numerical solution for a system of linear equations whose matrix is symmetric and positive-definite (Cheney and Kincard, 2007). They combined to give ELCIRC-sub a robust, efficient, and accurate mass-balance solver.

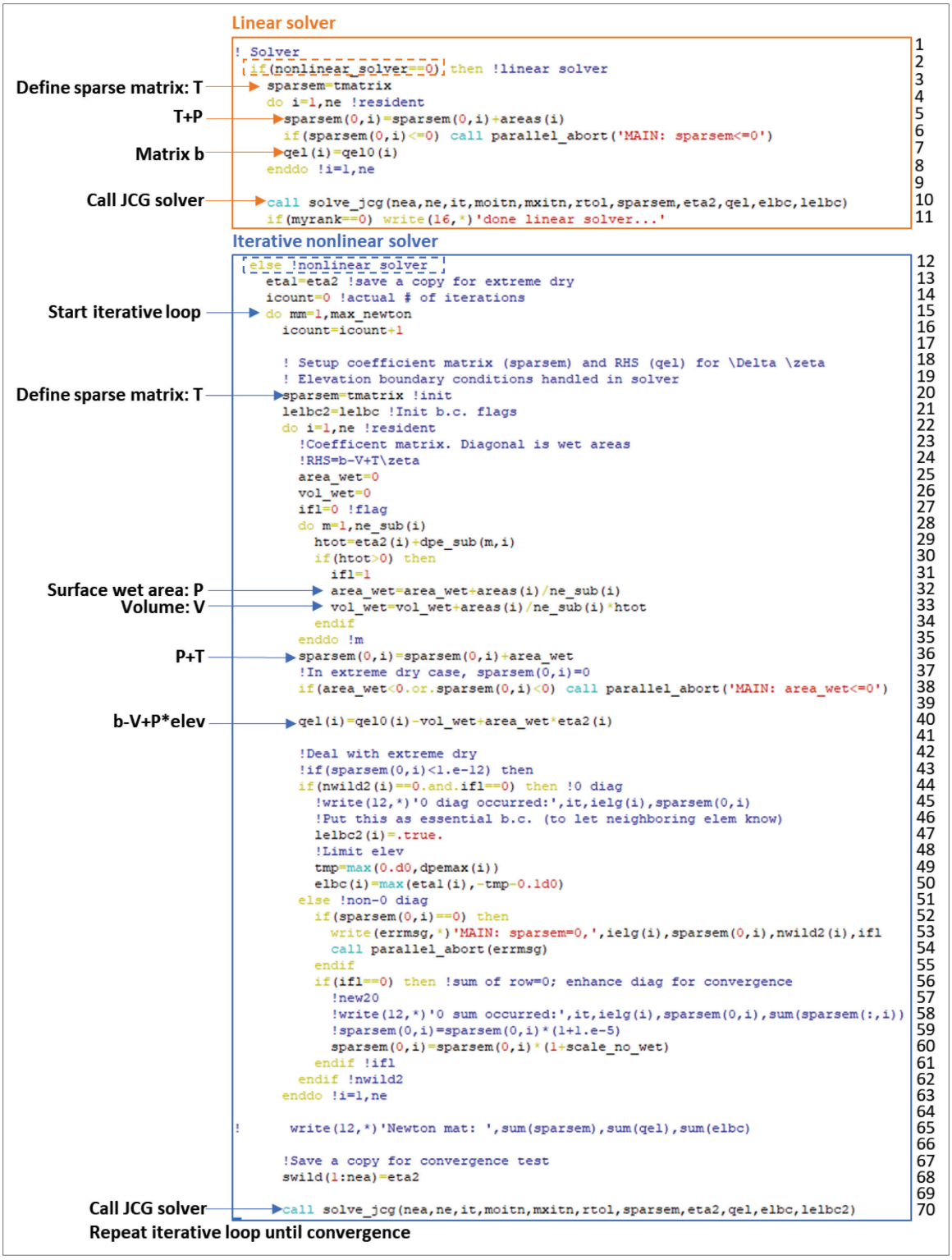


```
1  ! Solver
2  if(nonlinear_solver==0) then !linear solver
3    sparsem=tmatrix
4    do i=1,ne !resident
5      sparsem(0,i)=sparsem(0,i)+areas(i)
6      if(sparsem(0,i)<=0) call parallel_abort('MAIN: sparsem<=0')
7      qel(i)=qel0(i)
8    enddo !i=1,ne
9
10   call solve_jcg(nea,ne,it,moitn,mxitn,rtol,sparsem,eta2,qel,elbc,lelbc)
11   if(myrank==0) write(16,*)'done linear solver...'
12 else !nonlinear solver
13   etal=eta2 !save a copy for extreme dry
14   icount=0 !actual # of iterations
15   do mm=1,max_newton
16     icount=icount+1
17
18     ! Setup coefficient matrix (sparsem) and RHS (qel) for \Delta \zeta
19     ! Elevation boundary conditions handled in solver
20     sparsem=tmatrix !init
21     lelbc2=lelbc !Init b.c. flags
22     do i=1,ne !resident
23       !Coefficent matrix. Diagonal is wet areas
24       !RHS=b-V+T\zeta
25       area_wet=0
26       vol_wet=0
27       ifl=0 !flag
28       do m=1,ne_sub(i)
29         htot=eta2(i)+dpe_sub(m,i)
30         if(htot>0) then
31           ifl=1
32           area_wet=area_wet+areas(i)/ne_sub(i)
33           vol_wet=vol_wet+areas(i)/ne_sub(i)*htot
34         endif
35       enddo !m
36       sparsem(0,i)=sparsem(0,i)+area_wet
37       !In extreme dry case, sparsem(0,i)=0
38       if(area_wet<0.or.sparsem(0,i)<0) call parallel_abort('MAIN: area_wet<=0')
39
40       qel(i)=qel0(i)-vol_wet+area_wet*eta2(i)
41
42       !Deal with extreme dry
43       !if(sparsem(0,i)<1.e-12) then
44       if(nwild2(i)==0.and.ifl==0) then !0 diag
45         !write(12,*)'0 diag occurred:',it,ielg(i),sparsem(0,i)
46         !Put this as essential b.c. (to let neighboring elem know)
47         lelbc2(i)=.true.
48         !Limit elev
49         tmp=max(0.d0,dpemax(i))
50         elbc(i)=max(etal(i),-tmp-0.1d0)
51       else !non-0 diag
52         if(sparsem(0,i)==0) then
53           write(errmsg,*)'MAIN: sparsem=0,',ielg(i),sparsem(0,i),nwild2(i),ifl
54           call parallel_abort(errmsg)
55         endif
56         if(ifl==0) then !sum of row=0; enhance diag for convergence
57           !new20
58           !write(12,*)'0 sum occurred:',it,ielg(i),sparsem(0,i),sum(sparsem(:,i))
59           !sparsem(0,i)=sparsem(0,i)*(1+1.e-5)
60           sparsem(0,i)=sparsem(0,i)*(1+scale_no_wet)
61         endif !ifl
62       endif !nwild2
63     enddo !i=1,ne
64
65 !     write(12,*)'Newton mat: ',sum(sparsem),sum(qel),sum(elbc)
66
67     !Save a copy for convergence test
68     swild(1:nea)=eta2
69
70     call solve_jcg(nea,ne,it,moitn,mxitn,rtol,sparsem,eta2,qel,elbc,lelbc2)
```

Figure 51: Part of Fortran 90 code of linear and nonlinear solver implementation into ELCIRC-sub model. Explanation of code is shown on left, and line number of code is denoted on right.

4.3.2. Benchmark Test with Wetting/Drying Analytic Solution

A benchmark test was designed and conducted to verify the new sub-grid nonlinear solver developed in the ELCIRC-sub model by comparing with an analytical solution (Thacker, 1981). This is a simple 2-D and yet severe wetting/drying test case with the frictionless flow and is determined by the initial conditions of elevation. The horizontal model domain, as shown in Figure 52, is radially symmetric and has a radius of 450 km. The resolution of the base grid is 2.5km. The grid is constructed by taking mixed triangular and quadrilateral polygons in such a fashion that their vertices all lie on concentric circles such that their sides never exceed the interval between each circle. Each base grid side is divided in 10 subsides. No special grid refinement is used to cover the wetting and drying region. As a result, each base grid element consists of 100 sub-grid elements and in each sub-grid elements, the bathymetric data are specified. The bathymetry at each location is determined by the paraboloid formulation (Figure 53):

$$h(x,y) = h_0(1 - \frac{r^2}{L^2}) \qquad (14)$$

Where h_0 = 50m, L = 430 km, r is the distance from the origin (0,0).

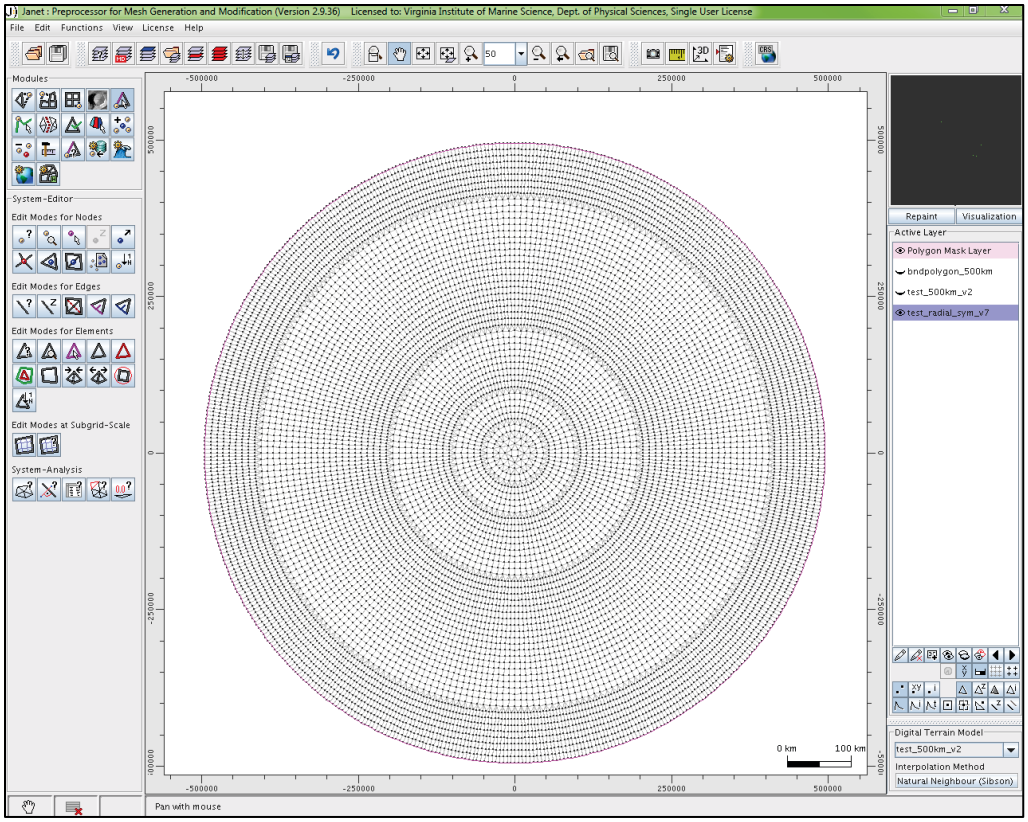

Figure 52: Horizontal model grid shown in Janet grid generation software.

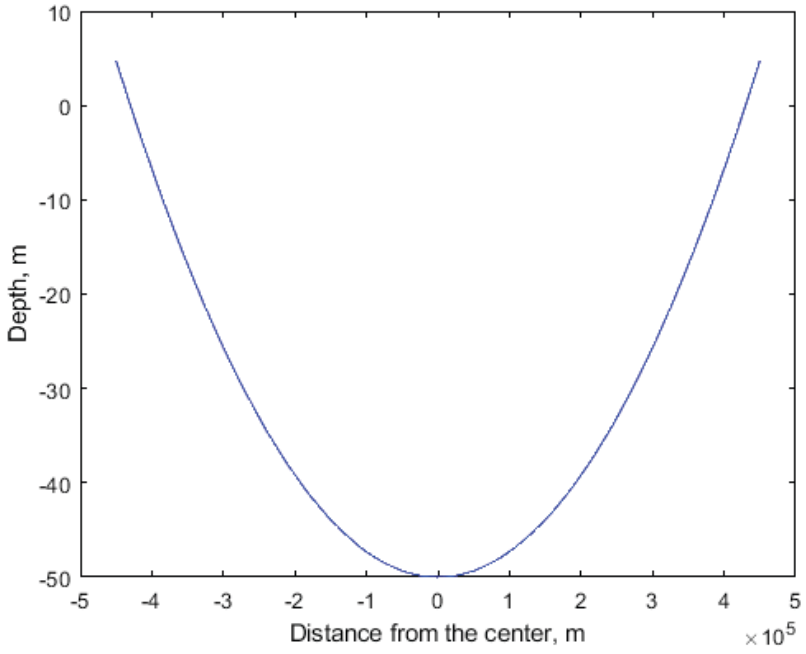

Figure 53: Cross-sectional view of the parabolic basin.

In the test, when a certain initial condition of free surface elevation is specified, the analytical solution of surface elevation (Eq. 15) and radial component of flow velocity (Eq. 16) at (x,y) for 2-D shallow water equations are given as:

$$\eta = h_0 \left\{ \frac{\sqrt{1-A^2}}{1-A\cos\omega t} - 1 - \frac{r^2}{L^2}\left[\frac{1-A^2}{(1-A\cos\omega t)^2} - 1 \right] \right\} \quad (15)$$

$$u_r = \frac{\omega r A \sin\omega t}{2(1-A\cos\omega t)} \quad (16)$$

where ω is the frequency of the prescribed surface wave signal. In this test case, the wave period is set to 12 hours (similar to the time scale of semi-diurnal tide) and the azimuthal velocity is zero because no Coriolis force is applied. For this specific period, L is calculated by Eq. 17 to be 430 km.

$$L = \sqrt{\frac{8gh_0}{\omega^2}} \quad (17)$$

The constant A is given by

$$A = \frac{(h_0+\eta_0)^2 - h_0^2}{(h_0+\eta_0)^2 + h_0^2} \quad (18)$$

Where η_0 is the initial elevation at the center of domain (0,0) and η_0 is set to 2 m. The cross-sectional view of initial surface elevation (t=0) derived from Eq. 15 is shown in Figure 54.

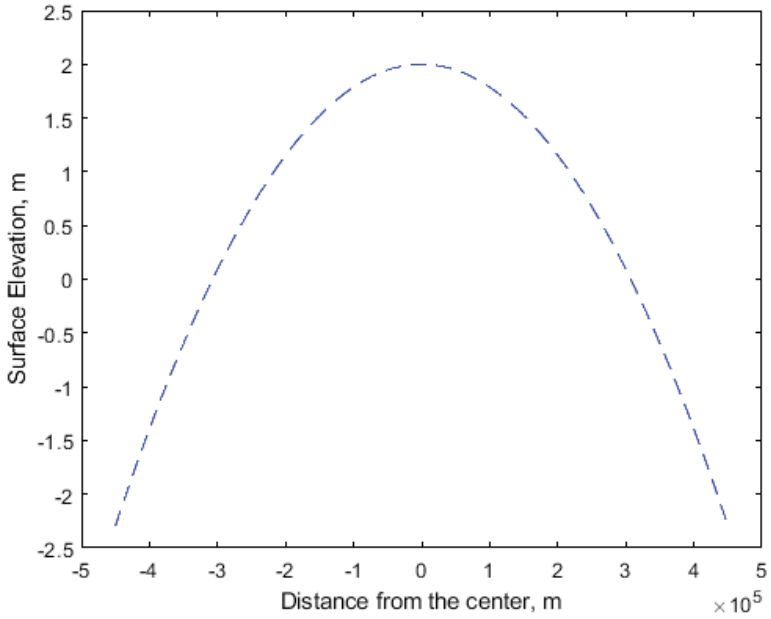

Figure 54: Cross-sectional view of initial surface elevation in this basic.

The shoreline is a circle whose center coincides with the center of the model domain and the radius of which is given by

$$R(t) = L\sqrt{\frac{1-A\,cos\omega t}{\sqrt{1-A^2}}} \qquad (19)$$

Thus, the permanently wet region is defined by the minimum value of R(t). The areas where r < min(R(t)) are always wet, and the wetting and drying occurs between min(R(t)) and max(R(t)), with min(R(t)) = 422 km and max(R(t)) = 439 km. So, the wetting and drying region is resolved by approximately 7 rings of the base grid elements.

The simulation started with the initial condition taken from Eq. 15 and Eq. 16 with t = 0. The model outputs elevation and velocity every 15 minutes and was computed for 10 wave periods (which is 120 hours) with a time step of 180s. The model run was performed using 16 CPUs on the Whirlwind sub-cluster of William and Mary's HPC

system, and the 120-hour simulation is finished within 6 minutes (i.e. 1,200 times real time speedup). It runs approximately 10 times faster than the UnTRIM^2 model for the same set up.

Elevation and velocity were determined at sixteen locations selected in the model domain and were compared with the analytical solution. These locations are along positive-x, negative-x, positive-y, and negative-y axes, and they are chosen at the distances from the center: 0.5*450 km, min(R) + 1.25 km, L + 1.25 km, and max(R) - 2.5 km. They cover both the "permanently wet" and the "wetting/drying" areas. Since the locations are radially symmetric to the center, theoretically speaking, the results should be identical at the same distance from the center. Based on this, the modeled results were compared with the analytic solution. Table 6 shows the (x,y) coordinates of all of those locations.

Table 6: X, Y coordinates of sixteen locations used for comparing model results with analytical solution.

ID	X (m)	Y (m)	Location
1	-223750	0	Permanently wet
2	-423750	0	Wet/dry
3	-431250	0	Wet/dry
4	-436250	0	Wet/dry (near Rmax)
5	223750	0	Permanently wet
6	423750	0	Wet/dry
7	431250	0	Wet/dry
8	436250	0	Wet/dry (near Rmax)
9	0	223750	Permanently wet
10	0	423750	Wet/dry
11	0	431250	Wet/dry
12	0	436250	Wet/dry (near Rmax)
13	0	-223750	Permanently wet
14	0	-423750	Wet/dry
15	0	-431250	Wet/dry
16	0	-436250	Wet/dry (near Rmax)

Figure 55 shows the time series of the modeled elevation and analytical solution at sixteen locations. The modeled surface elevation has the same period (12 hours) as the analytical solution. Over the permanently wet locations, the model results and analytical solution almost overlap everywhere. In wetting/drying zones, the elevation has a cut-off/discontinuity due to the element being dry and the duration of being dry increases as the location moves further from the center. At the locations near max(R), the dry duration is the longest. The elevation shows a radial symmetry in that at the same distance from the center the time series are the same, which is consistent with the symmetric properties anticipated. The ELCIRC-sub model also matches with analytical solution very well in terms of phase and amplitude at all locations, except that a relatively larger error is found after approximately 48 hours at locations 4, 8, 12, and 16, which are closer to the permanently dry zone, presumably due to the numerical dissipation of the model. The amplitude of surface elevation at those locations are generally smaller than that of the analytical solution and the largest error is within approximately 5% of the amplitude. The average RMSE of elevation in the wetting and drying zone is 0.08 m (less than 5% error).

Figure 56 shows the time series of the modeled radial velocity versus that of the analytical solution at sixteen locations. Over the permanently wet locations, the model results and analytical solution match almost everywhere. The modeled radial velocity has the same period (12 hours) as the analytical solution. In wetting/drying zones, the velocities show cut-off values due to the element being dry and the duration of dry increases as the location moves further away from the center. At the locations near max(R), the dry period is the longest. The velocity also possessed a radial symmetry property similar to that for the elevation plots. There is a very minor phase difference

(less than 10 min) between the model predictions and the analytical solution in the wetting/drying zone. A slightly larger error in amplitude was found at the location closer to the permanently dry zone. The average RMSE of radial velocity in the wetting and drying zone is 0.1 m/s (less than 10% error).

Figure 57 also shows the time series of the modeled azimuthal velocity and analytical solution at sixteen locations. In theory, the azimuthal velocity should be zero since the Coriolis force is not introduced in this test case. The model results verify this with zero velocity everywhere in both the domain including permanently wet and wet/dry zones. The high accuracy is also partly attributed to a better scheme (Thuburn et al., 2009) to reconstruct the tangential velocity at the cell edge as weighted sum of the known normal velocity at a set of nearby edges with analytically-derived weights. As a result, the conservation of mass, energy and potential vorticity are better preserved.

Lastly, the dry region simulated by EICIRC-sub can be recognized by having exactly zero water depth while the transition from wet to dry and from dry to wet is modeled smoothly, rather than a discontinuous surface. This has a strong implication on accuracy of the inundation extent.

The model results are consistent with Casulli's study (2009) and we were able to compare additional results of velocity not only in permanently wet regions but also in partially wet or dry regions. Without high-resolution sub-grid bathymetry, the model couldn't resolve the wetting and drying regions.

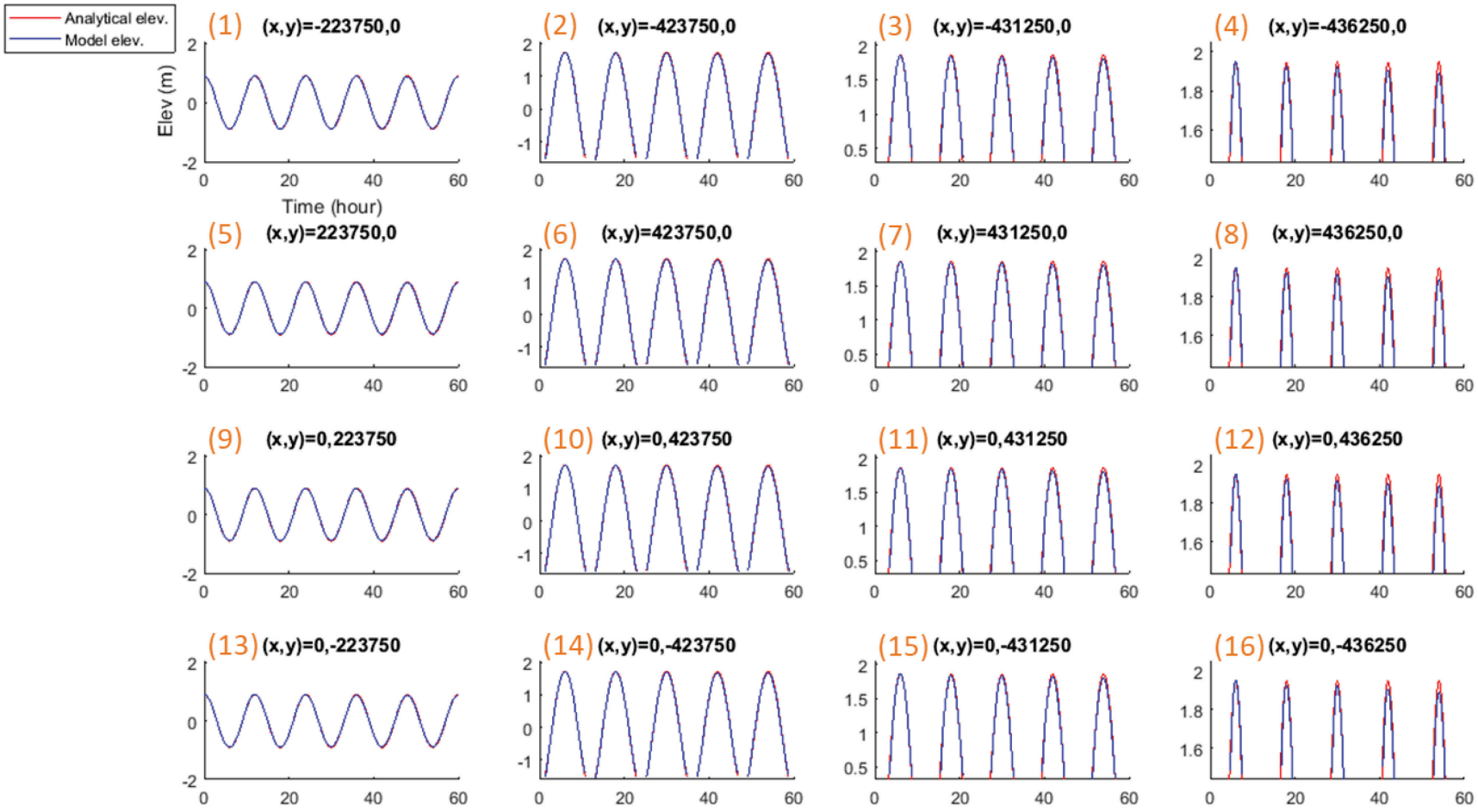

Figure 55: Time series comparisons of modeled surface elevation and analytical solution at sixteen locations in the model domain.

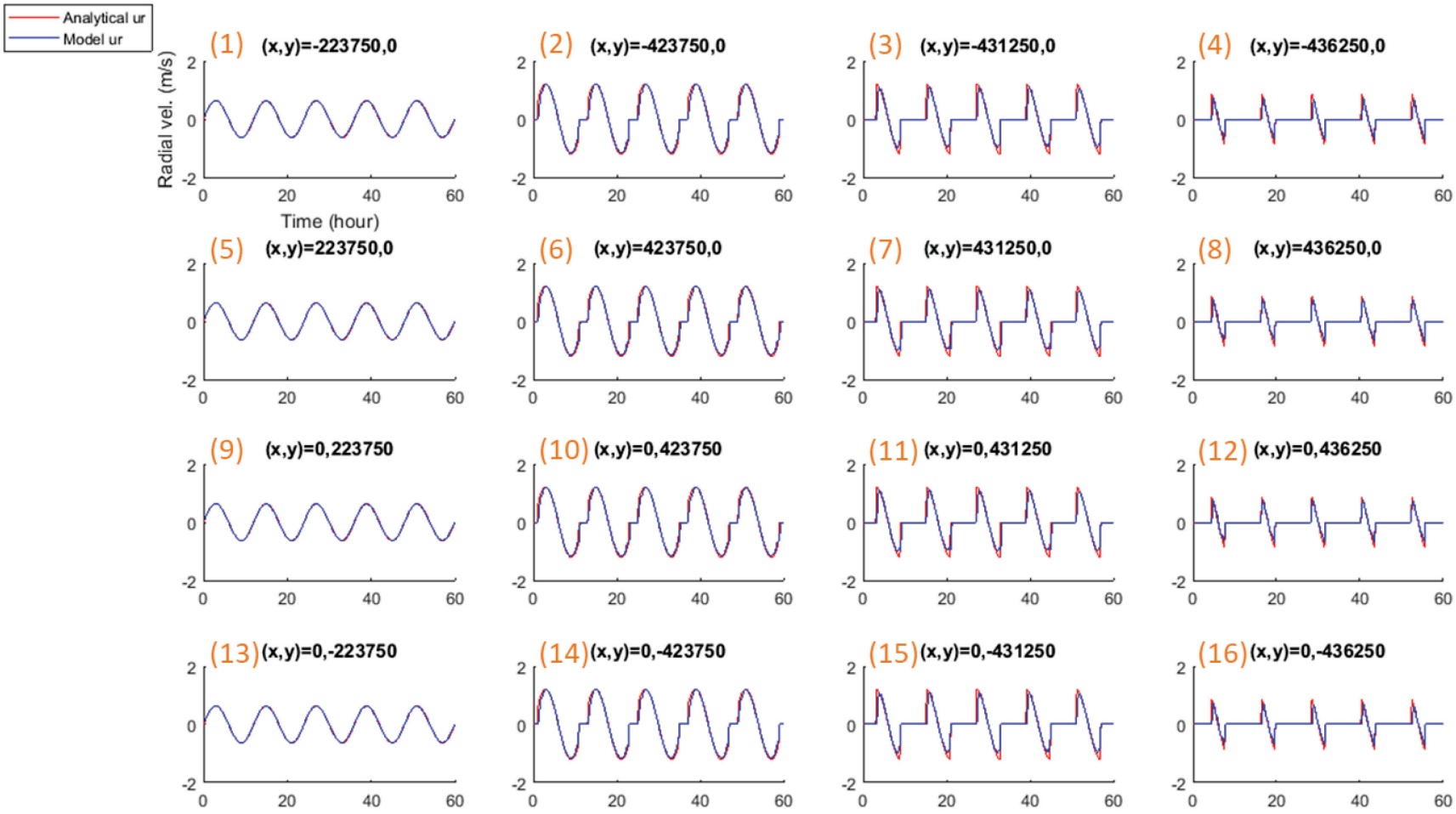

Figure 56: Time series comparisons of modeled radial velocity and analytical solution at sixteen locations in the model domain.

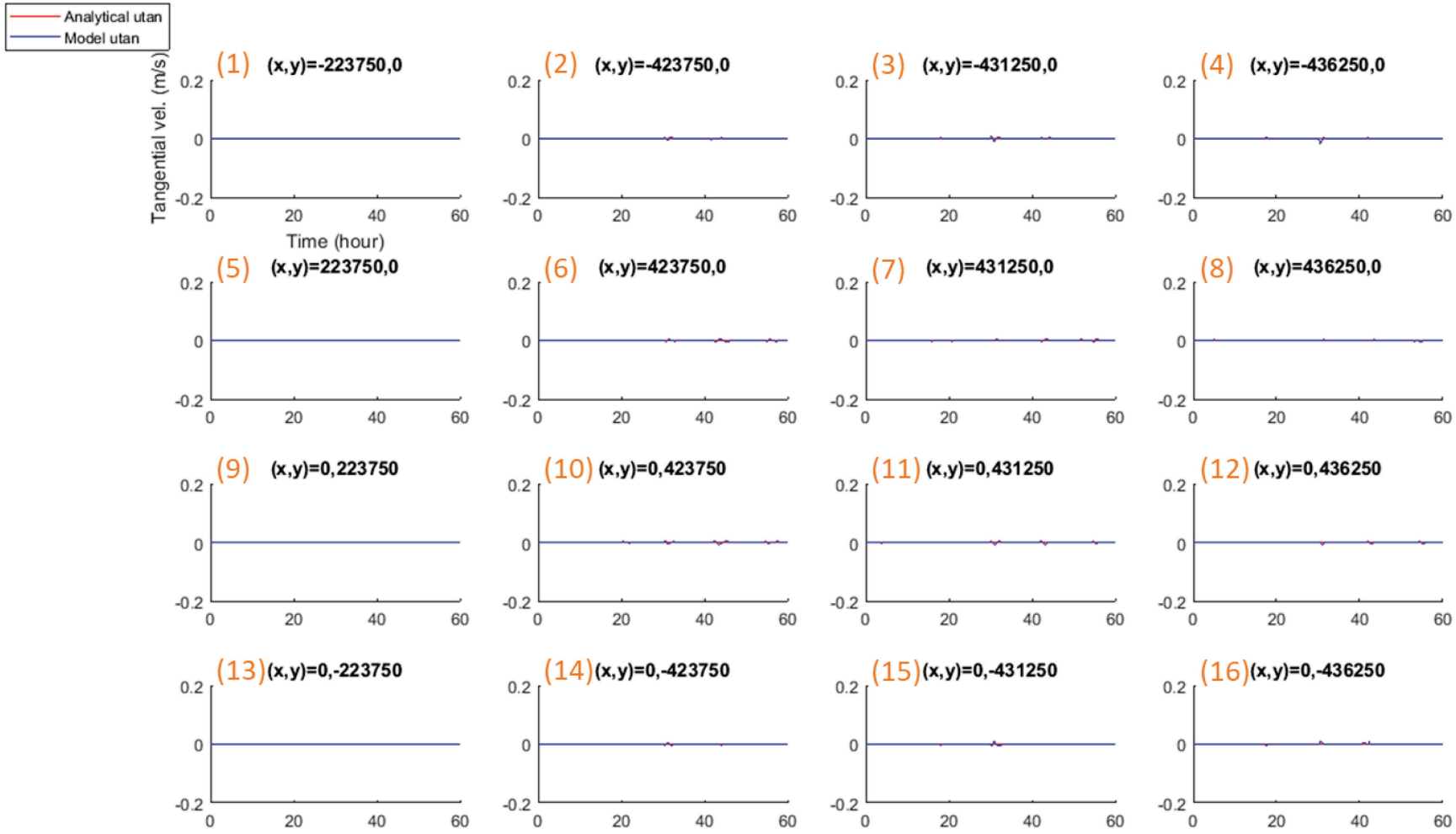

Figure 57: Time series comparisons of modeled azimuthal velocity and analytical solution at sixteen locations in the model domain.

Overall, it is confirmed that the proposed mildly nonlinear formulation of the wetting and drying processes in the ELCIRC-sub model yields excellent results at the sub-grid level compared with the analytic solution. In addition, the specification of bathymetric details at sub-grid level plays an important role to obtain an accurate mass balance in the wetting and drying region where any polygon is allowed to be wet, partially wet or dry.

In summary, in this chapter, we described an efficient and accurate iterative nonlinear solver built on sub-grids for wetting/drying process that was developed in the 2-D ELCIRC-sub inundation model. It was built on unstructured computational grid, consisting of mixed triangular and quadrilateral grids, and a high spatial resolution sub-grids to obtain an accurate mass balance in shallow flows with complex geometries. With the parallel computing capability of ELCIRC-sub model, it is more efficient and can have much larger horizontal coverage than UnTRIM^2. The benchmark test with wetting/drying analytic solution confirmed ELCIRC-sub has been properly coded with newly developed iterative nonlinear solver, which is accurate, stable, robust, and quite efficient. In the following Chapter 5, the ELCIRC-sub model will be tested in realistic inundation simulation during hurricane events, for example, Hurricane Sandy of 2012.

CHAPTER 5. Application of Sub-Grid Inundation Model for 2012 Hurricane Sandy

5.1. Model Setup and Configuration

5.1.1. Model Domain and Grid

The effect of storm surge on water level by Hurricane Sandy 2012 was studied by the wind-wave coupled 3-D barotropic SCHISM model in Chapter 3. In deriving the storm surge induced by the Hurricane, the water was piled up by wind, pressure, wind wave, and moved through the ocean into coastal water bodies. The water level was observed primarily by NOAA using tidal gauges installed in the waterways. In this chapter, our focus is on the inundation that is the water flooded across the shoreline onto the land surface and moved through the urban environment. The measurements for inundation is conducted primarily by USGS using high water mark and rapid deployed pressure gauge.

The ELCIRC-sub model was used to simulate the inundation during 2012 Hurricane Sandy in Greater New York. The sub-grid horizontal domain covers Staten Island, Hudson River, Manhattan, Bronx, Brooklyn, Queens, Harlem River, East River and further extended through Long Island Sound to New London, CT (Figure 58). This domain is much larger than the previous work by Wang et al. (2014). The square computational base grid of 200 m * 200 m was chosen and, the 20-by-20 sub-grids, resulted in 10 m * 10 m cells embedded within each base grid cell. The grid consists of 87,665 base grid nodes and 89,853 base grid elements and the number of sub-grid elements is approximately 35 million. The LIDAR topography data around New York City were obtained from the previous study in the same area (Loftis, 2014) in 10-m resolution DEM. The bathymetry data were based on integrating the data from the NOAA Bathymetry Survey Data with a spatial resolution of about 10 m (NOAA, 2006) and NOAA Coastal Relief Model with a spatial resolution of about 90 m (NOAA, 2011).

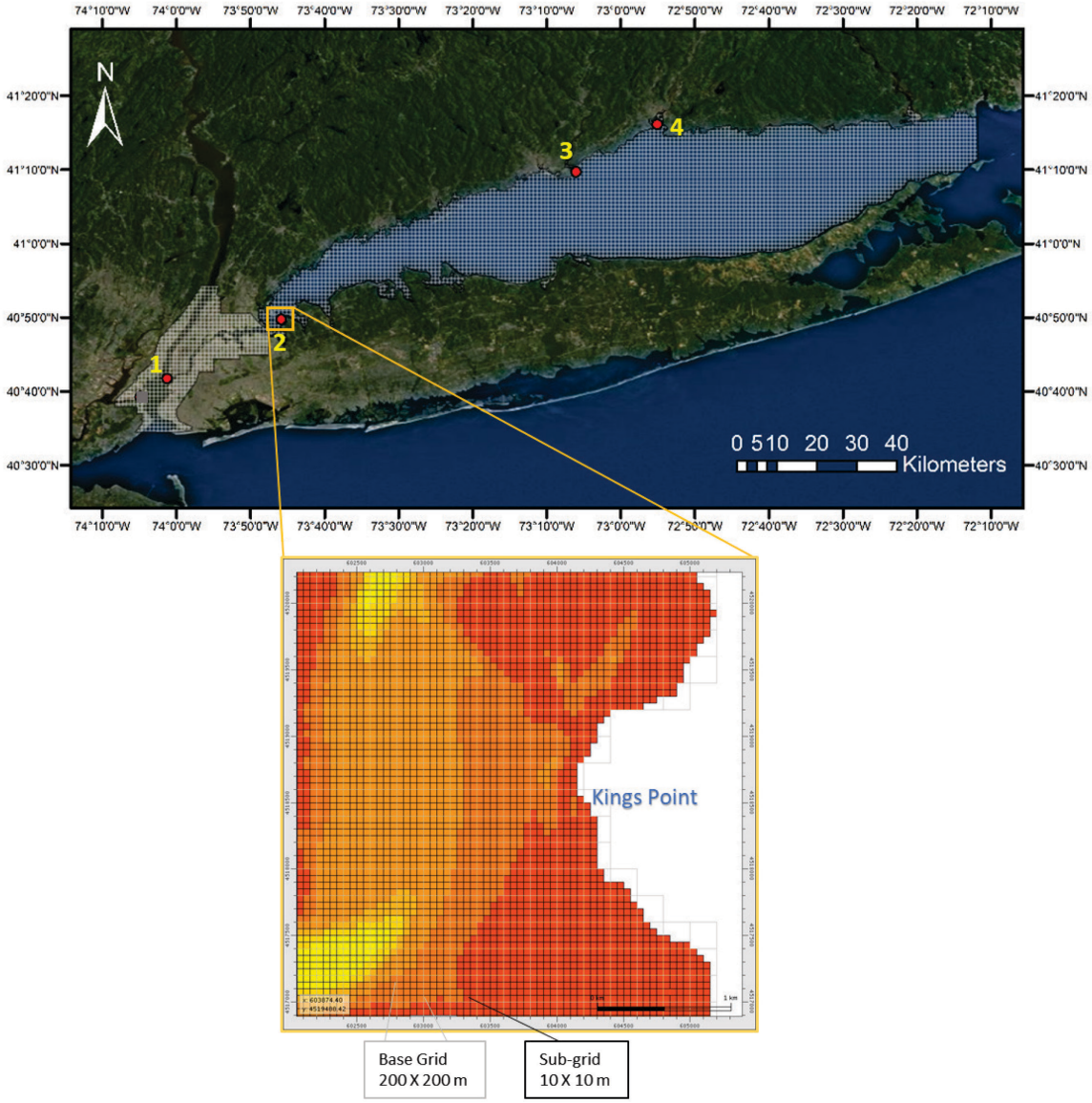

Figure 58: Top panel: The high resolution sub-grid domain (shaded regions) covering New York City, part of Hudson River up to Yonkers, part of Long Island Sound up to East Lyme, CT. Red dots labeled by numbers from west to east show NOAA tidal gauges: The Battery, NY, Kings Point, NY, Bridgeport, CT, and New Haven, CT; Bottom panel: The sub-grid 10 m-by-10 m embedded in the 200 m by 200 m resolution base grid shown in the zoom-in yellow box around Kings Point, NY.

5.1.2. Model Forcings and Efficiency

The ELCIRC-sub model setup in the greater New York City requires one river flux and two water level boundary conditions. Two water elevation forcing is applied at two open boundaries: one to the south, and one to the east. The southern open boundary is located at the mouth of New York Bay which uses observed water elevation data at USGS Rockaway Inlet (Station #1311875). The eastern open boundary is between Greenport, NY and New London, CT and uses observed water elevation data at NOAA tidal gauge New London, CT (Station #8461490) with adjustment in phase based on distance from this gauge location. The river flux is set at the northern boundary based on hourly water flow data for Hudson River obtained from USGS at Wappingers Falls (Station #01372500). The same bottom drag coefficient as in Section 3.2.1. was used.

The atmospheric forcing data - wind and pressure were collected in units of m/s and Pa from NOAA atmospheric observation data at NOAA buoy observations at Bridgeport, CT Station BRHC3 (NOAA NDBC, 2012) near the central location of Long Island Sound. Atmospheric observations were subsequently pre-processed and prepared as uniform wind and pressure inputs throughout the entire domain. The u and v wind velocities were extracted from wind data and interpolated to 6-minute time steps, commencing on October 22, 2012, at 00:00 UTC, and ending November 1, 2012, at 00:00 UTC. Subsequently, the wind speeds were adjusted to the values at a height of 10 m above ground based on logarithmic boundary layer profile.

The simulation period started on October 22, 2012 00:00 UTC and ended on November 1, 2012 00:00 UTC. The simulation was executed on the Bora subcluster of the College of William and Mary's HPC system. A total of 80 CPUs were used and the

10-day inundation simulation was completed in 19 minutes (i.e., 720 times real time speedup factor). In comparison, a simulation with the same resolution of base grids but no sub-grid set-up requires 16 minutes. So, the increase in computational time with introducing huge numbers of sub-grid is small, which confirms the efficiency of the new nonlinear solver developed in Section 4.3.1.

5.1.3. Observation Data

(1) NOAA Tidal Gauges

The tidal elevation observations from 4 NOAA tide gauges in New York Harbor and Long Island Sound were used to compare with ELCIRC-sub model's storm tide results relative to Mean Sea Level (MSL). The locations and detailed information of these stations are shown in Figure 58 and Table 7.

Table 7: Detailed information of NOAA tidal gauges.

Station ID	Station Name	Latitude (degrees N)	Longitude (degrees W)	Observation
NOAA-8518750	The Battery, NY	40.6957	-74.0210	Water level
NOAA-8516945	Kings Point, NY	40.8291	-73.7642	Water level
NOAA-8467150	Bridgeport, CT	41.1620	-73.1005	Water level
NOAA-8465705	New Haven, CT	41.2833	-72.9083	Water level

(2) USGS Water Level Gauges

The USGS deployed a monitoring network of rapid-deployed pressure gauge to measure water-levels over the land around New York City during Hurricane Sandy (McCallum et al., 2013). The measurements covered the period between October 28, 2012 and November 1, 2012 (USGS, 2013). Six of these rapid deployment gauges were used for evaluation of the model's accuracy for predicting storm tide (Figure 59). Detailed information of each water level gauges is shown in Table 8.

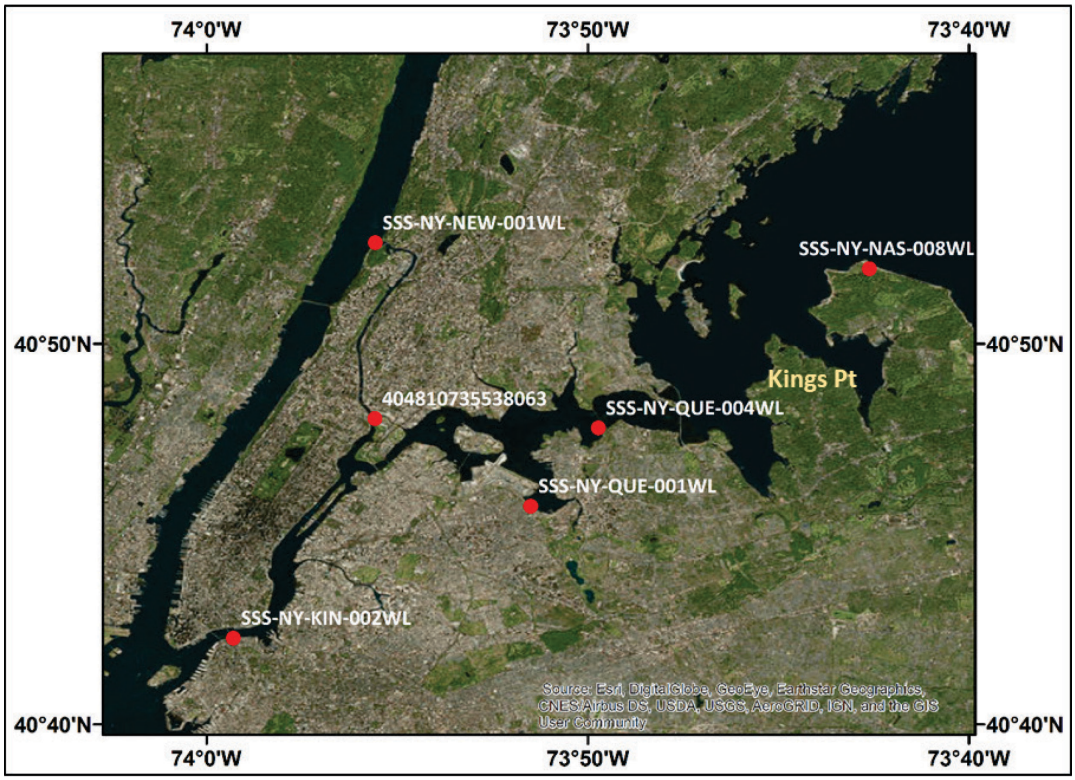

Figure 59: Location map of six USGS water level gauges within the model domain.

Table 8: Description of USGS water level gauges.

Station Name	Longitude (degrees W)	Latitude (degrees N)	Observation	Interval (s)
SSS-NY-KIN-002WL	-73.9883	40.7046	Water Level	30
404810735538063	-73.9265	40.8006	Water Level	900
SSS-NY-NEW-001WL	-73.9263	40.8776	Water Level	30
SSS-NY-QUE-001WL	-73.8583	40.7623	Water Level	30
SSS-NY-NAS-008WL	-73.7102	40.8662	Water Level	30
SSS-NY-QUE-004WL	-73.8288	40.7965	Water Level	30

(3) USGS High Water Marks

During Hurricane Sandy, the USGS surveyed 950 high water mark locations in the ranging from Virginia to Massachusetts (USGS, 2017). Among them, a total of 80 USGS non-wave affected high water mark measurements around New York City (Figure 60). The measurements were surveyed relative to NAVD88 and converted to Mean Sea Level. They were considered as the maximum extent for inundation during the event and later used for model-data comparison. Most of measurements were collected in New York City and New Jersey adjacent to the Hudson River where the impacts of the storm were the heaviest. The inundation extent output from ELCIRC-sub model is temporally varied; the maximum from them over the entire event in each sub-grid were selected to compare with field measured water mark at the observation sites.

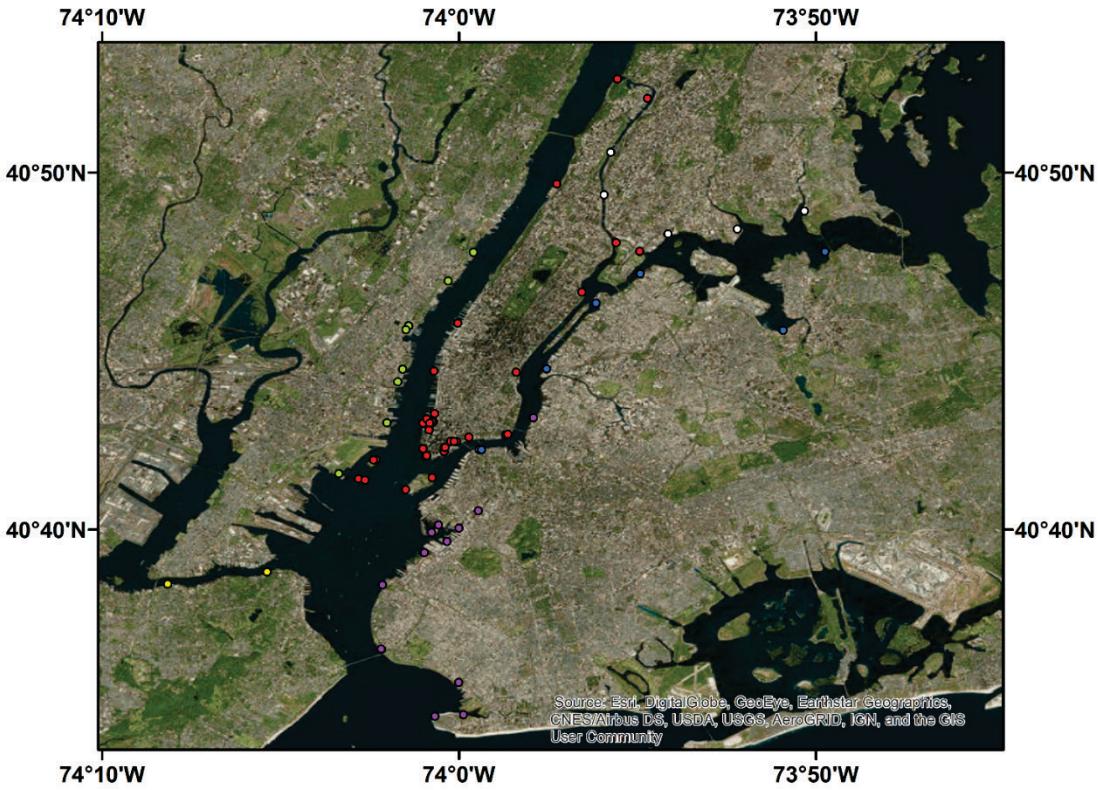

Figure 60: Location map of 80 non-wave affected USGS-recorded high water mark sites (colored dots) within the ELCIRC-sub domain utilized for spatial verification of model results. High water marks were used to verify the maximum spatial extent of inundation via vertical water height measurements.

FEMA also generated maximum extent inundation map. It was based upon interpolation of the USGS's water elevation measurements from the monitoring network including high water marks and water level gauges, presented in the previous sections, and were intersected with the best available elevation data. The water level measurements combined with DEM were utilized to create a water elevation, layer thickness and a 0-m contour for the maximum extent of inundation (Figure 61). The products include an inundation grid at 1 m resolution in New York City and 3 m resolution in New Jersey, along with a clipped surge boundary (FEMA MOTF, 2013).

Figure 61: Maximum extent of inundation map (blue areas) for New York City and New Jersey generated by FEMA via interpolation of high water marks measurements and the best available elevation dataset (FEMA MOTF, 2013). Note that the orange dashed polygon is part of the ELCIRC-sub model domain near New York City.

5.2. Temporal Comparisons of Storm Tide Results

5.2.1. NOAA Tidal Gauges

The sub-grid model results were first compared with time series of storm tides obtained from NOAA tidal observations (they were compared with measurements of rapid deployed gauge and high water marks later). Figure 62 shows the comparisons of NOAA observations and modeled storm tide results at four locations: The Battery, NY, Kings Point, NY, Bridgeport, CT, and New Haven, CT. Model performance at all four stations are excellent with the mean absolute error on the order of 5-10 cm (Table 9) and much better than other models' > 20 cm error for this same region. Among them, one unique surge record measured at Kings Point, whose water level changed nearly 4 m within 2 hours, was accurately simulated by the model both in term of the maximum height and its near abrupt surge shape (Figure 63). The error in modeling the peak storm surge is less than 10 cm, which is the best result from all the large-scale storm surge models making prediction for Hurricane Sandy such as SLOSH, ADIRC, ECOM-SED, and ROMS. The excellent skill is attributed to the high resolution sub-grids using 10 m resolution in ELCIRC-sub model.

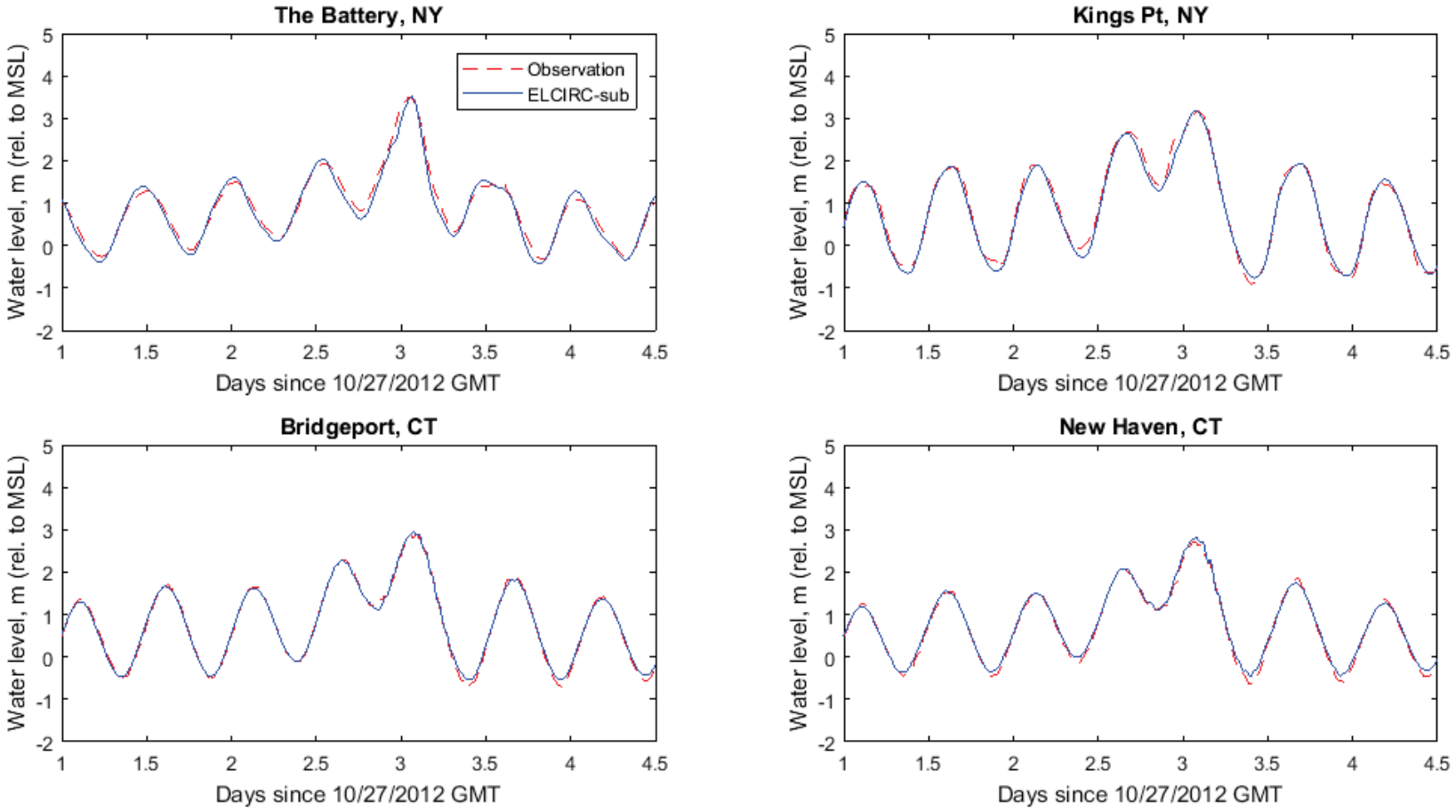

Figure 62: Time series of comparisons of modeled storm tide with NOAA observed water level at (a) The Battery, NY; (b) Kings Point, NY; (c) Bridgeport, CT; and (d) New Haven, CT

Table 9: Statistical evaluation of ELCIRC-SG modeled storm tide and NOAA observed water level at 4 stations.

Stations	R^2	RMSE (m)	MAE (m)
The Battery, NY	0.97	0.126	0.105
Kings Point, NY	0.97	0.111	0.085
Bridgeport, CT	0.98	0.057	0.045
New Haven, CT	0.98	0.075	0.058

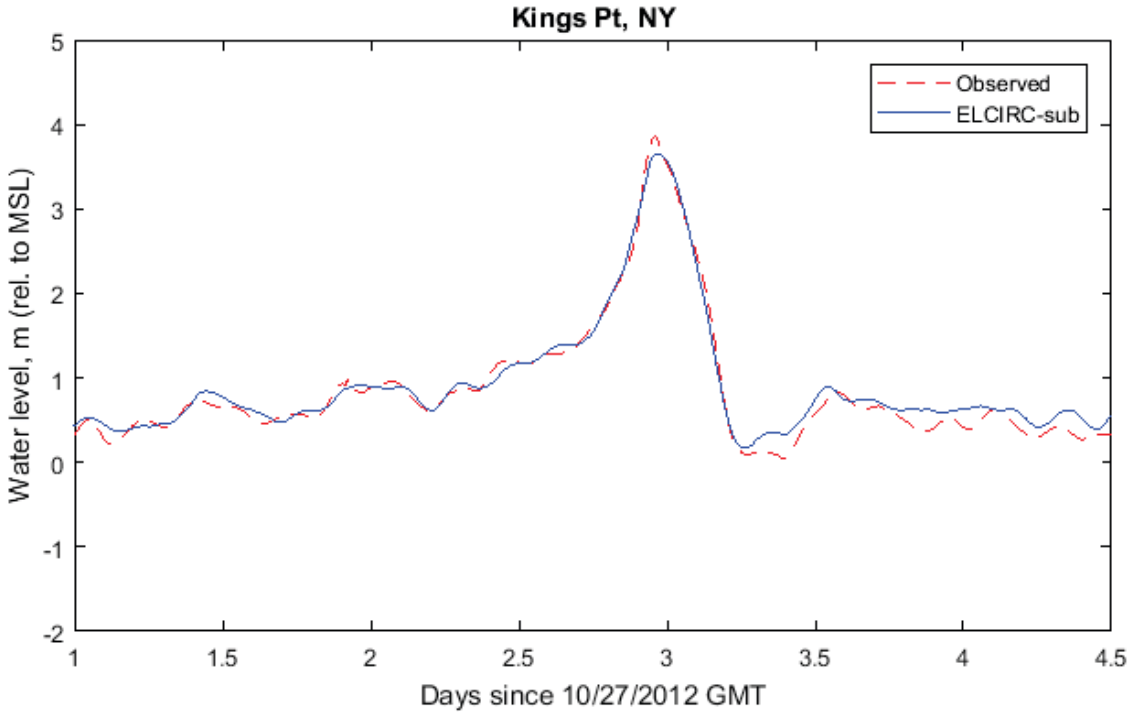

Figure 63: Time series of comparisons of modeled storm surge with NOAA observed surge at Kings Point, NY.

5.2.2. USGS Water Level Gauges

USGS undertook a great effort in deploying the on-land press gauge over an incredibly short time during Hurricane Sandy. Each of the USGS water level pressure gauges recorded data in 30-second intervals except for USGS 404810735538063, which recorded data in 15-minute intervals. All the measurements were relative to NAVD 88 datum and converted to Mean Sea Level datum. USGS 404810735538063 and SSS-NY-QUE-001WL remain permanently wet throughout the observation period. The overland gauges are set at a fixed height, so they can become dry when the water falls below the bottom of the elevation sensor. The data record for USGS 404810735538063 at the junction of the Harlem and East Rivers was lost before the peak of the storm surge. Station SSS-NY-NAS-008WL is outside the model's DEM coverage, so a nearby location was chosen to compare with observed data.

At all stations, the ELCIRC-sub's results agree very well compared with the measured data. Both amplitude and phase are modeled quite accurately (Figures 64-69). The ELCIRC-sub overlaps with the observed water level before its cut-off level, and it also captured the timing and the depth of the peak water level quite accurately. Even at 404810735538063 where the river geometry is quite complex, the ELCIRC-sub could model the water level accurately (Figure 65), which demonstrates the strong capability of sub-grid set-up in resolving the complex shoreline without a fully refined unstructured grid. At SSS-NY-QUE-001WL and SSS-NY-QUE-004WL, the modeled elevation is better than that of a previous study that compared at the same locations (Loftis, 2014). The comparisons of peak water level and timing between model and data for each station except 404810735538063 are shown in Table 10. The average error in modeling peak water level is on the order of 10 cm, and the average error in modeling the timing of peak water level is 8 minutes.

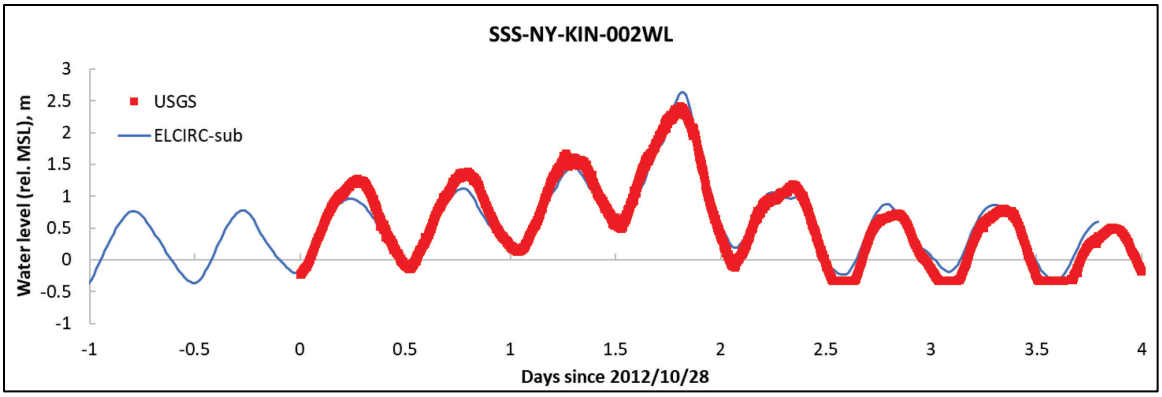

Figure 64: Time series of comparisons between ELCIRC-sub predictions and USGS gauge data at SSS-NY-KIN-002WL.

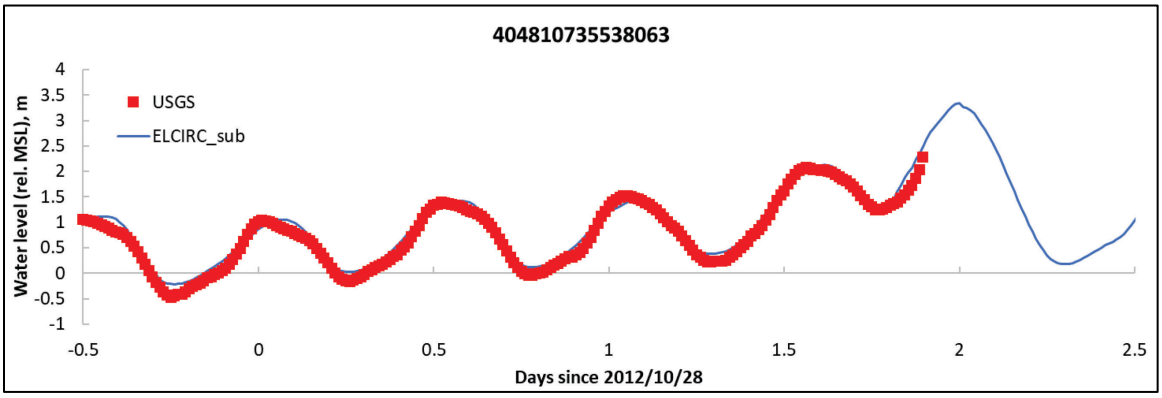

Figure 65: Time series of comparisons between ELCIRC-sub predictions and USGS gauge data at 404810735538063.

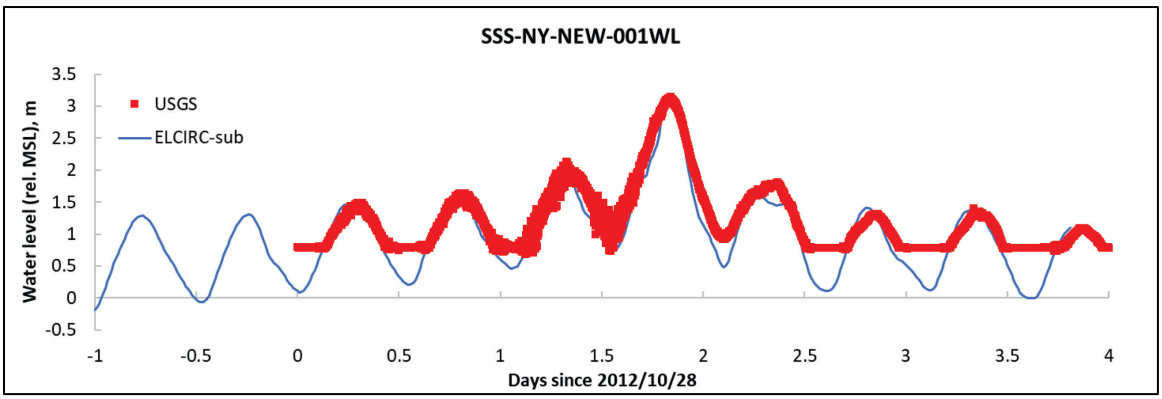

Figure 66: Time series of comparisons between ELCIRC-sub predictions and USGS gauge data at SSS-NY-NEW-001WL.

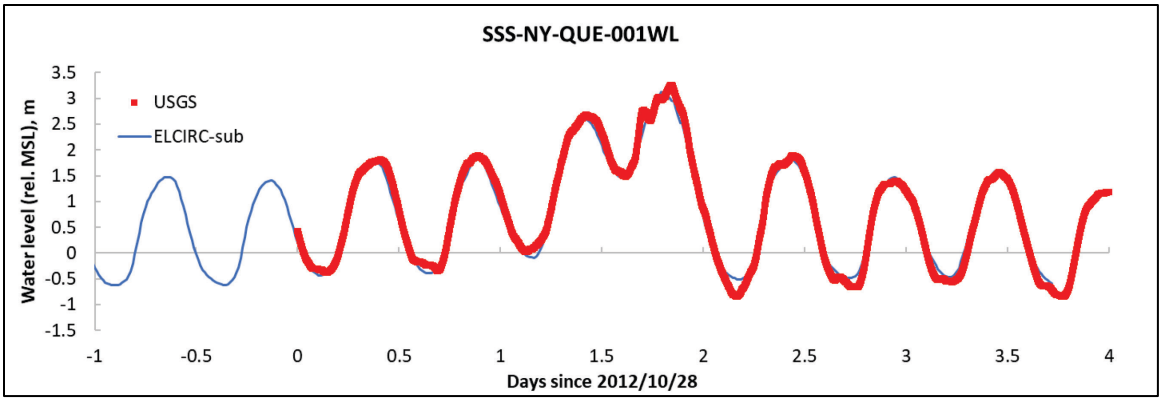

Figure 67: Time series of comparisons between ELCIRC-sub predictions and USGS gauge data at SSS-NY-QUE-001WL.

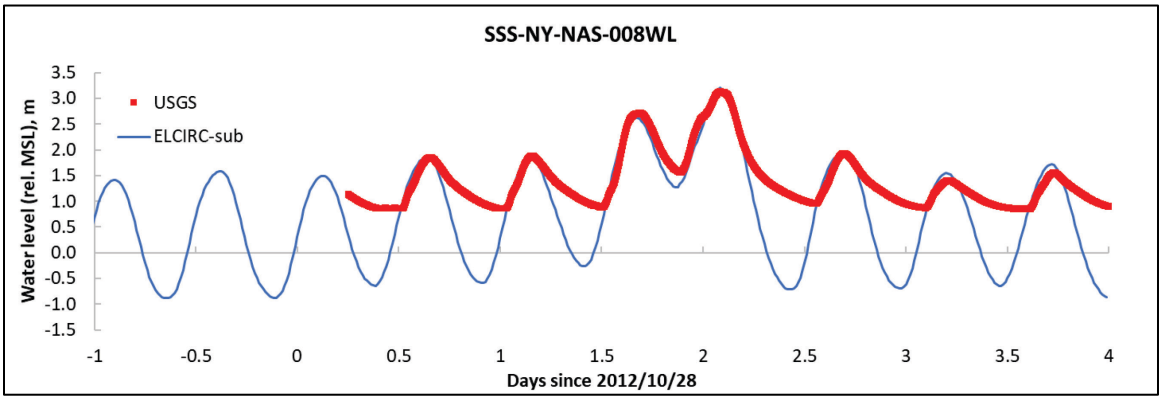

Figure 68: Time series of comparisons between ELCIRC-sub predictions and USGS gauge data at SSS-NY-NAS-008WL.

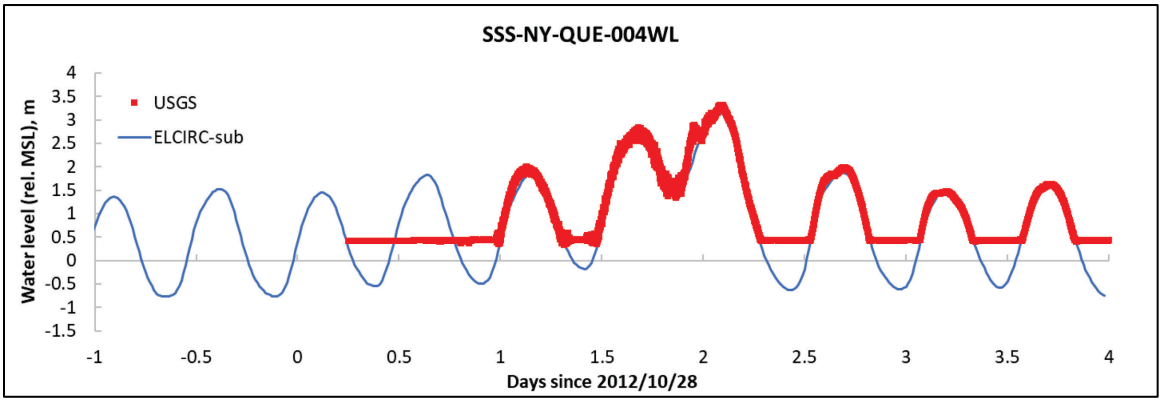

Figure 69: Time series of comparisons between ELCIRC-sub predictions and USGS gauge data at SSS-NY-QUE-004WL.

Table 10: Model-Data comparisons of peak water level and associated timing at five USGS water level gauges.

Station Name	Peak Water Level (m)		Time (GMT)	
	Model	Data	Model	Data
SSS-NY-KIN-002WL	2.54	2.39	2012/10/29 19:57	2012/10/29 19:48
SSS-NY-NEW-001WL	3.17	3.14	2012/10/29 20:09	2012/10/29 20:01
SSS-NY-QUE-001WL	3.13	3.25	2012/10/29 19:54	2012/10/29 20:06
SSS-NY-NAS-008WL	3.20	3.13	2012/10/30 01:57	2012/10/30 02:00
SSS-NY-QUE-004WL	3.16	3.32	2012/10/30 01:57	2012/10/30 02:05

5.3. Spatial Comparisons of Inundation Results

The modeled spatial extent of inundation and depth of flood water was evaluated via comparisons with various field measurements. First, 80 USGS-collected non-wave affected high water mark measurements around the New York City were compared with water level elevations above Mean Sea Level. Second, the modeled maximum flooded area coverage is compared with FEMA's maximum extent inundation map, which was generated from interpolation of the USGS's high water marks and the result of DEM.

5.3.1. USGS High Water Marks

The measurements were separated by counties in the New York City and the State of New Jersey. The ELCIRC-sub's maximum water level was extracted at each location of the high water mark. Then, the difference between model and measurement is calculated to assess the accuracy of ELCIRC-sub (Table 11). A total of 44 of the high water marks were measured on Manhattan, New York City, with an absolute difference between the observed high-water mark and the maximum water level height by the model ranging from 0.003 m to 0.282 m (Table 11: ID 1-44). There are 15 of the high water marks were in Brooklyn (or Kings County), ranging in difference from 0.006 m to 0.330 m (Table 11: ID 45-59), and 5 marks were in the Bronx County with model-measurement differences ranging from 0.001 m to 0.276 m (Table 11: ID 60-64). Five of the high water marks were located in Queens ranging from 0.011 m to 0.245 m in difference (Table 11: ID 65-69), and 2 marks were on Staten Island (or Richmond County) ranging from 0.079 m to 0.250 m (Table 11: ID 70-71).

Along the New Jersey coast, a total of nine high water marks were recorded in Hudson County. These marks had a large range of difference from 0.144 m to 0.521 m compared to the model results (Table 11: ID 72-80). This is somewhat anticipated due to the lack of accurate DEM-generated topography data along the New Jersey coast of the Hudson River. As a result, the model over-predicted the flooding extent due to lack of the building imprint in blocking flooding waters.

The statistics evaluation presented in Table 12 indicated overall accurate model prediction with an average difference of 0.102 m in New York City. In comparison, the model tended to over-predict the peak water level in the New Jersey side of the Hudson River. The average difference of 0.357 m for New Jersey coast obviously has a higher error than that in New York City. This difference of model performance between New York City and the State of New Jersey confirms the importance of the accurate DEM data and the buildings layer in the urban inundation modeling.

Table 11: Spatial comparisons of highest water elevation between USGS High Water Mark (HWM) and ELCIRC-sub model at 80 locations around New York City.

ID	HWM ID	Latitude (degrees N)	Longitude (degrees W)	State	USGS (m)	Model (m)	Difference (m)
1	HWM-NY-NEW-100	40.7011	-74.0156	NY	3.606	3.540	-0.065
2	HWM-NY-NEW-101	40.7011	-74.0150	NY	3.545	3.540	-0.004
3	HWM-NY-NEW-102	40.7044	-74.0169	NY	3.118	3.270	0.152
4	HWM-NY-NEW-103	40.7044	-74.0167	NY	3.423	3.560	0.137
5	HWM-NY-NEW-802	40.8770	-73.9260	NY	2.966	2.817	-0.149
6	HWM-NY-NEW-803	40.8680	-73.9119	NY	2.813	3.095	0.282
7	HWM-NY-NEW-806	40.7966	-73.9155	NY	3.453	3.334	-0.119
8	HWM-NY-NEW-113	40.7108	-73.9781	NY	3.484	3.402	-0.081
9	HWM-NY-NEW-114	40.7108	-73.9781	NY	3.392	3.402	0.010
10	HWM-NY-NEW-115	40.7108	-73.9781	NY	3.392	3.402	0.010
11	HWM-NY-NEW-116	40.7111	-73.9772	NY	3.392	3.402	0.010
12	HWM-NY-NEW-117	40.7111	-73.9772	NY	3.392	3.402	0.010
13	HWM-NY-NEW-118	40.7111	-73.9772	NY	3.423	3.402	-0.021
14	HWM-NY-NEW-119	40.7111	-73.9772	NY	3.392	3.402	0.010
15	HWM-NY-NEW-128	40.7208	-74.0114	NY	3.362	3.426	0.064
16	HWM-NY-NEW-108	40.7078	-74.0039	NY	3.453	3.515	0.062
17	HWM-NY-NEW-109	40.7078	-74.0011	NY	3.423	3.505	0.082
18	HWM-NY-NEW-110	40.7078	-74.0022	NY	3.453	3.515	0.062
19	HWM-NY-NEW-111	40.7078	-74.0022	NY	3.453	3.515	0.062

ID	HWM ID	Latitude (degrees N)	Longitude (degrees W)	State	USGS (m)	Model (m)	Difference (m)
20	HWM-NY-NEW-112	40.7097	-73.9953	NY	3.484	3.494	0.010
21	HWM-NY-NEW-120	40.7164	-74.0161	NY	3.392	3.572	0.179
22	HWM-NY-NEW-121	40.7164	-74.0167	NY	3.392	3.574	0.182
23	HWM-NY-NEW-122	40.7181	-74.0147	NY	3.514	3.576	0.062
24	HWM-NY-NEW-123	40.7183	-74.0150	NY	3.453	3.576	0.123
25	HWM-NY-NEW-124	40.7169	-74.0119	NY	3.392	3.568	0.175
26	HWM-NY-NEW-125	40.7169	-74.0125	NY	3.301	3.512	0.212
27	HWM-NY-NEW-126	40.7164	-74.0136	NY	3.057	3.322	0.265
28	HWM-NY-NEW-127	40.7131	-74.0139	NY	3.027	3.195	0.168
29	HWM-NY-NEW-104	40.7031	-74.0069	NY	3.514	3.519	0.005
30	HWM-NY-NEW-105	40.7050	-74.0067	NY	3.453	3.517	0.063
31	HWM-NY-NEW-106	40.7050	-74.0067	NY	3.484	3.517	0.033
32	HWM-NY-NEW-107	40.7050	-74.0064	NY	3.484	3.517	0.033
33	HWM-NY-NEW-981	40.8006	-73.9265	NY	3.209	3.363	0.154
34	HWM-NY-NEW-001	40.7776	-73.9425	NY	3.240	3.303	0.063
35	HWM-NY-NEW-002	40.8280	-73.9542	NY	2.966	2.792	-0.173
36	HWM-NY-NEW-003	40.7407	-74.0117	NY	3.819	3.604	-0.215
37	HWM-NY-NEW-004	40.7631	-74.0005	NY	3.240	3.422	0.182
38	HWM-NY-NEW-005	40.7401	-73.9733	NY	3.362	3.391	0.029
39	HWM-NY-NEW-008	40.6904	-74.0469	NY	3.514	3.547	0.033

ID	HWM ID	Latitude (degrees N)	Longitude (degrees W)	State	USGS (m)	Model (m)	Difference (m)
40	HWM-NY-NEW-009	40.6897	-74.0439	NY	3.545	3.542	-0.003
41	HWM-NY-NEW-011	40.6994	-74.0387	NY	3.453	3.551	0.098
42	HWM-NY-NEW-012	40.6909	-74.0125	NY	3.423	3.521	0.098
43	HWM-NY-NEW-013	40.6853	-74.0249	NY	3.484	3.529	0.046
44	HWM-NY-NEW-010	40.6991	-74.0399	NY	3.453	3.551	0.098
45	HWM-NY-KIN-604	40.7040	-73.9894	NY	3.423	3.459	0.036
46	HWM-NY-KIN-903	40.6109	-74.0363	NY	4.002	3.725	-0.276
47	HWM-NY-KIN-504	40.7040	-73.9905	NY	3.514	3.466	-0.048
48	HWM-NY-KIN-904	40.5952	-74.0001	NY	3.575	3.246	-0.330
49	HWM-NY-KIN-905	40.5802	-73.9979	NY	3.575	3.280	-0.295
50	HWM-NY-KIN-510	40.7189	-73.9652	NY	3.484	3.371	-0.113
51	HWM-NY-KIN-511	40.6688	-74.0096	NY	3.484	3.490	0.006
52	HWM-NY-KIN-715	40.5794	-74.0112	NY	3.850	3.622	-0.228
53	HWM-NY-KIN-724	40.6652	-74.0127	NY	3.514	3.493	-0.021
54	HWM-NY-KIN-725	40.6754	-73.9910	NY	3.057	3.216	0.159
55	HWM-NY-KIN-001	40.6408	-74.0356	NY	3.514	3.460	-0.054
56	HWM-NY-KIN-900	40.6673	-74.0000	NY	3.423	3.477	0.054
57	HWM-NY-KIN-901	40.6611	-74.0056	NY	3.484	3.485	0.002
58	HWM-NY-KIN-902	40.6558	-74.0162	NY	3.575	3.478	-0.097
59	HWM-NY-KIN-605	40.7040	-73.9894	NY	3.392	3.459	0.067

ID	HWM ID	Latitude (degrees N)	Longitude (degrees W)	State	USGS (m)	Model (m)	Difference (m)
60	HWM-NY-BRO-804	40.8428	-73.9290	NY	3.027	3.303	0.276
61	HWM-NY-BRO-805	40.8230	-73.9322	NY	3.088	3.216	0.128
62	HWM-NY-BRO-807	40.8047	-73.9023	NY	3.301	3.353	0.052
63	HWM-NY-BRO-808	40.8070	-73.8700	NY	3.209	3.340	0.131
64	HWM-NY-BRO-809	40.8154	-73.8386	NY	3.331	3.330	-0.001
65	HWM-NY-QUE-505	40.7417	-73.9590	NY	3.331	3.380	0.049
66	HWM-NY-QUE-506	40.7723	-73.9360	NY	3.392	3.304	-0.089
67	HWM-NY-QUE-509	40.7862	-73.9153	NY	3.270	3.026	-0.245
68	HWM-NY-QUE-520	40.7964	-73.8290	NY	3.362	3.284	-0.078
69	HWM-NY-QUE-603	40.7597	-73.8486	NY	3.270	3.259	-0.011
70	HWM-NY-RIC-722	40.6468	-74.0895	NY	3.636	3.557	-0.079
71	HWM-NY-RIC-723	40.6412	-74.1359	NY	3.575	3.325	-0.250
72	HWM-NJ-HUD-007	40.7619	-74.0234	NJ	3.209	3.652	0.442
73	HWM-NJ-HUD-008	40.7619	-74.0234	NJ	3.148	3.652	0.503
74	HWM-NJ-HUD-010	40.7416	-74.0263	NJ	3.270	3.425	0.155
75	HWM-NJ-HUD-108	40.6927	-74.0561	NJ	3.697	3.553	-0.144
76	HWM-NJ-HUD-109	40.7165	-74.0336	NJ	3.240	3.582	0.342
77	HWM-NJ-HUD-110	40.7356	-74.0285	NJ	3.301	3.611	0.311
78	HWM-NJ-HUD-421	40.7828	-74.0050	NJ	3.148	3.669	0.521
79	HWM-NJ-HUD-422	40.7961	-73.9932	NJ	3.057	3.415	0.358
80	HWM-NJ-HUD-420	40.7599	-74.0248	NJ	3.209	3.645	0.435

Table 12: Statistics Table including average difference, average absolute difference, and Root-Mean-Squared-Error for the comparison between USGS-measured high water level and ELCIRC-sub's modeled peak water level.

HWM Location	Average Difference (m)	Average Absolute Difference (m)	RMSE (m)
New York City (ID 1-71)	0.017	0.102	0.134
New Jersey Coast (ID 72-80)	0.325	0.356	0.379

5.3.2. FEMA Maximum Flooding Map

The ELCIRC-sub's maximum flooding extent map was generated by summing up maximum surface elevation and DEM (with the negative depth upward and positive depth downward relative to MSL) in each sub-grid (Figure 70). An area is defined as "flooded" when the total depth (surface water elevation plus DEM) is larger than zero. The QGIS software (https://qgis.org/en/site/), a similar software as ArcGIS but with better color map and being more compatible with Python scripts, was used for visualizing flooding extent and comparing the model result with FEMA map. To execute QGIS for visualizing flooding extent, the steps are as follows: (1) Loaded high-resolution DEM into QGIS as the model domain. Depending upon the pointing directions of positive depths, the "raster calculator" in QGIS may be used to change the sign of depths; (2) Loaded a base map from Google Map or ArcGIS as the background layer for visualizing street-level inundation. The "compute_maxelev" script was used to calculate maximum water elevation at all nodes and interpolate onto sub-grid element; (3) Loaded the output ".csv" file into QGIS as XY data and the "vector to raster" command is executed to convert it to raste; (4) The "raster calculator" was used to sum the values of DEM and elevation at the sub-grid level to attain the total water depth raster and finally, (5) The

maximum flooding extent is visualized by cropping out the raster with the original 0 m total depth shoreline.

The high-resolution, zoom-in comparisons of the FEMA map and the ELCIRC-sub flooding map show the model's good performance in simulating the maximum inundation extent (Figures 71-74). In lower Manhattan, model results match well visually with the FEMA map as the water flooded onto the streets near the southern tip of Manhattan (Figures 71 and 72). In East River and Harlem River, the ELCIRC-sub also did a great job in simulating the flooding around the LGA Airport and along the river banks (Figures 73 and 74). After taking out the surface building area, the match percentage between modeled inundation area and FEMA inundation map within ELCIRC-sub model domain was calculated as the ratio of the overlapping ("match") area to the total flooded area. Table 13 shows the statistical values for the entire New York City, two specific highlighted regions (lower Manhattan and West Brooklyn; Part of East River, Harlem River, and LGA) shown in Figures 71 and 73, respectively, New Jersey coastline within model domain, and the total flooded area around NJ coast and NYC.

Table 13: Statistical comparisons for inundated areas in different regions within ELCIRC-sub model domain around New Jersey coast and New York City.

Region	Match Flooded Area (million m^2)	Match (%)	Total Flooded Area (million m^2)
Entire New York City	31.46	73.7	42.68
Lower Manhattan and West Brooklyn	2.49	74.8	3.33
Part of East River, Harlem River, and LGA	6.37	72.3	8.81
New Jersey Coast	17.62	77.1	22.85
Across NJ Coast and NYC	49.08	74.9	65.53

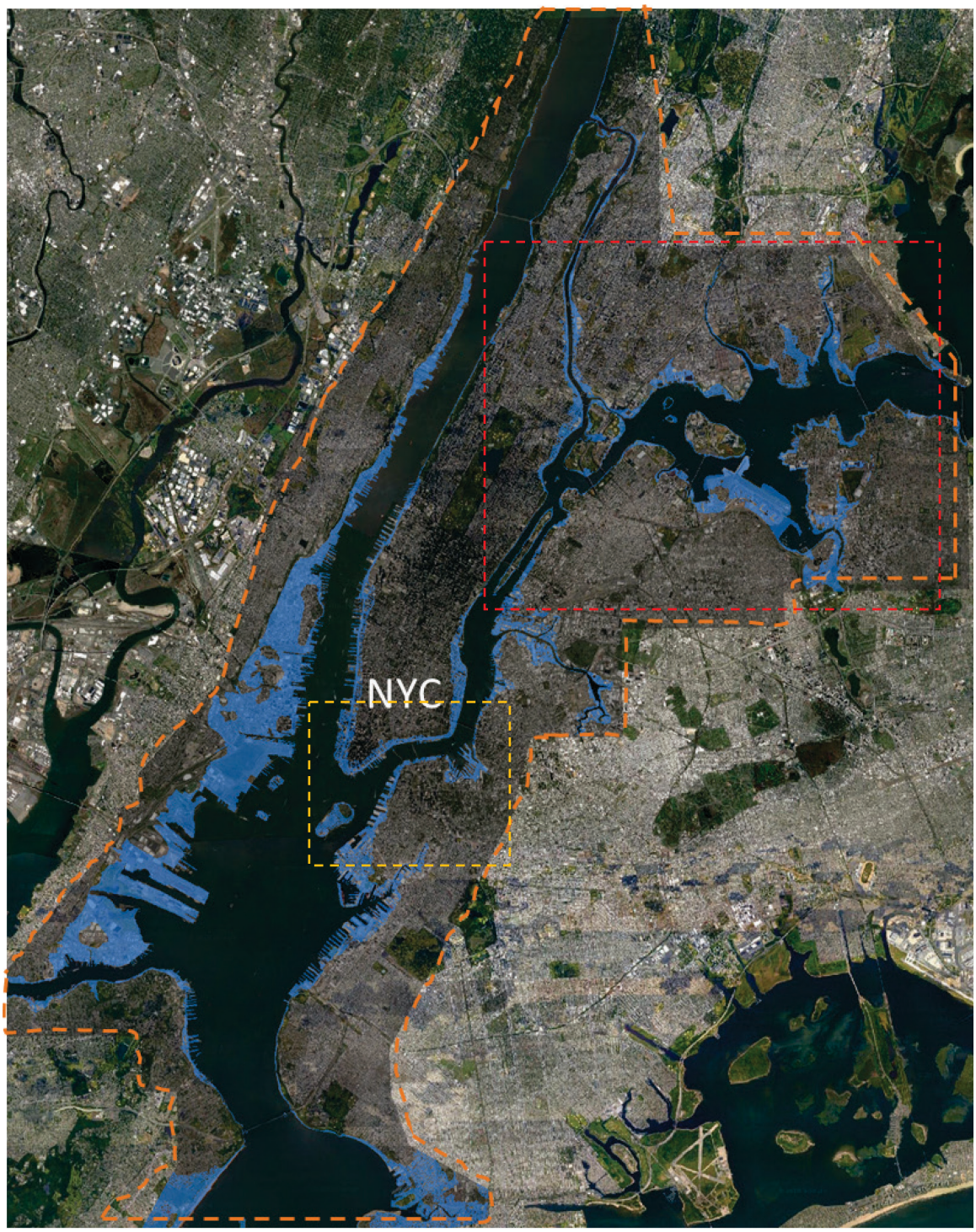

Figure 70: The ELCIRC-sub modeled maximum flooding map around New York City during Hurricane Sandy. Blue region is flooded area in the model. The orange dashed polygon is the part of ELCIRC-sub model domain near NYC.

Figure 71: FEMA maximum flooding extent in the zoom-in of yellow box in Figure 70.

Figure 72: The ELCIRC-sub modeled maximum inundation extent in the zoom-in of yellow box in Figure 70.

Figure 73: FEMA maximum flooding extent in the zoom-in of red box in Figure 70.

Figure 74: The ELCIRC-sub modeled maximum inundation extent in the zoom-in of red box in Figure 70.

Additional street-level comparisons between the modeled inundation extent and FEMA map extent are conducted for three local areas near lower Manhattan and La Guardia Airport which were socioeconomically vulnerable and were heavily damaged during Hurricane Sandy.

Near the Governors Island and Southwest Brooklyn, Figure 75 shows the ELCIRC-sub model elevation predictions matching with FEMA map elevations extremely well with 82% match. The model was able to accurately simulate the flooding over the Governors Island and onto the streets in the Red Hook area of Brooklyn. Figure 76 shows the model's street-level inundation results at the southern tip of Manhattan. On the west side of this area, although the FEMA map doesn't show inundation, the model was able to simulate the flooding from the Hudson River and thus a smaller match percentage (70%) due to the difference between these two. Figure 77 shows the flooded LaGuardia Airport during Hurricane Sandy. The ELCIRC-sub model captured the flooding over the airport's runways and low-lying areas well with 80% match. Although the flood extent map generated by FEMA is regarded as the benchmark reference for evaluating model performance, uncertainties and errors can also be introduced into it from spatial interpolation of limited and unevenly distributed monitoring points. In addition, many local inland streets, which were not hydraulically connected to the flood, have been incorrectly categorized as inundated areas because FEMA's planar method considered neither mass conservation nor hydraulic connectivity and surface roughness.

Figure 75: Comparisons of maximum flooding extent map between FEMA and ELCIRC-sub model near Governors Island and West Brooklyn.

Figure 76: Comparisons of maximum flooding extent map between FEMA and ELCIRC-sub model at the southern tip of Manhattan where one NOAA tidal gauge: The Battery is located.

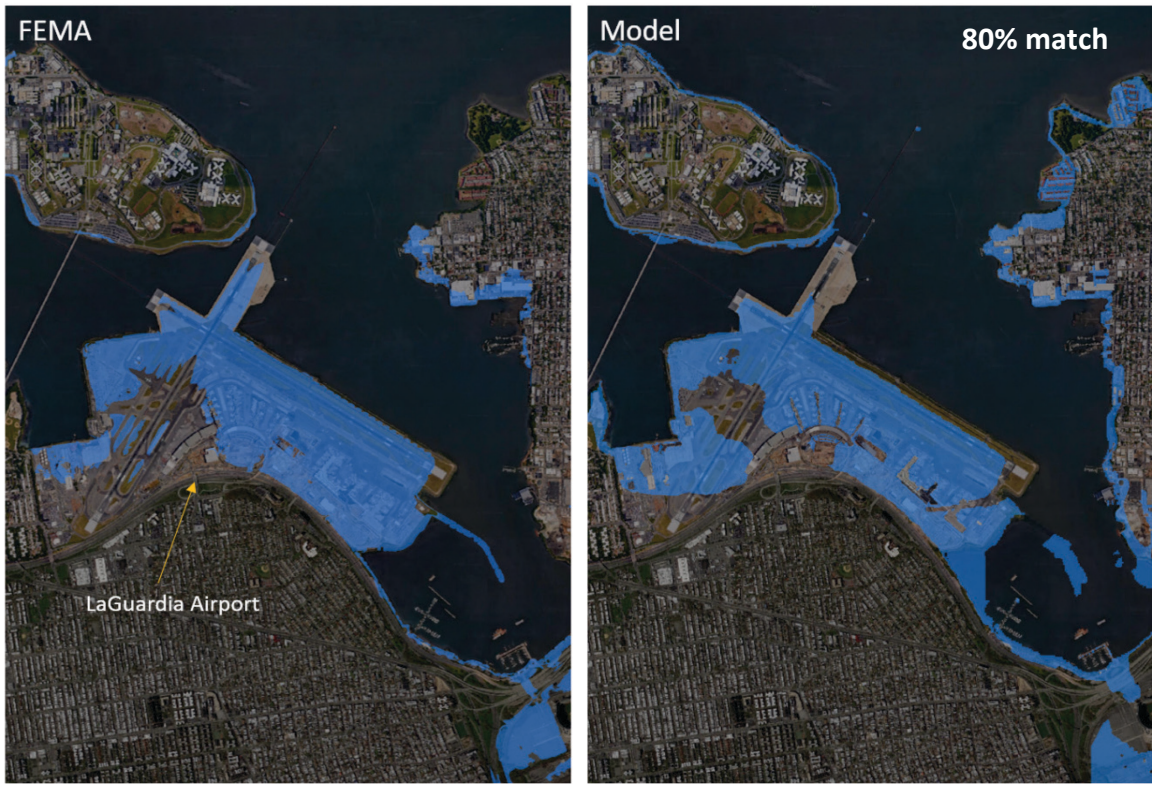

Figure 77: Comparisons of maximum flooding extent map between FEMA and ELCIRC-sub model near LaGuardia Airport.

CHAPTER 6. Discussions and Conclusions

6.1. Summary and Discussions

6.1.1. Large-Scale Storm Tide Model

A 3-D barotropic large-scale unstructured grid storm tide SCHISM model coupled with Wind Wave Model (WWMIII) was developed in Chapter 2 to cover the entire U.S. East Coast and Gulf Coast with an open boundary aligning on the 60-degree West longitude. The reason the open boundary condition was specified similar to a gateway more than 1,500 km away is to ensure that any hurricanes potential to land the US continent will be within the domain. Furthermore, with the Hurricane's radius of maximum wind (RMW) on average of 50 km, that means the open boundary is at the least 10 times of the RMW distance away from the hurricane. It is with this safety distance that the open boundary condition can be assumed to be unaffected by the hurricane storm and be specified with mean sea level and astronomical tide.

In Chapter 3, The SCHISM storm tide model accurately simulates tidal propagation along the U.S. Eastern Seaboard and embayments within the model grid with good accuracy. The excellent tidal harmonic analysis results for both amplitude and phase suggest that the large-scale SCHISM model grid is sufficient when compared with NOAA prediction data. After verifying the model's superior capability in simulating tide propagation, the model was tested to hindcast storm tide during Hurricane Sandy in 2012 and Hurricane Irene in 2011. For Hurricane Sandy simulation, the 3-D barotropic SCHISM model coupled with WWMIII simulated the maximum storm tide with an error less than 8 cm at The Battery, NY, which is located at the tip of Lower Manhattan. The overall model performance is quite good: RMSE values are on the order of 8-15 cm, and MAE values are on the order of 6-12 cm. In general, this large-scale 3-D storm surge

simulation performed very well during this severe hurricane event, especially over the location of most concern, New York City. For Hurricane Irene simulation, the coupled model using ECMWF atmospheric forcing was able to simulate the maximum storm tide with an error on the order of 7-8 cm. The average R^2 for all stations is 0.97, the average RMSE is 11 cm, and the average MAE is 9 cm.

In both hurricane simulations, WWMIII model's results (significant wave heights and peak wave periods) were also compared with NDBC observation at different stations off coasts. The wave model worked well with average relative error in wave height around 10%, and the error in peak period is 1-3 seconds.

Hurricane wind fields can be complex. A range of phenomena form complicated wind features such as spiral bands, embedded high velocity burst region, and eye wall break down and re-establishment, which can markedly affect winds fields in a storm. Despite the complexity, the hurricane wind field produced by two hurricane models - NAM and ECMWF, out-perform other atmospheric models to provide adequate forcing for storm surge models (Cho et al. 2009; Loftis et al. 2014; Garzon et al., 2018). That is the very reason why they were chosen for this study. In Section 3.2.3.1, comparisons of storm tide simulations using NAM and ECMWF show that simulations using the ECMWF atmospheric model have better results than those using the NAM model in all comparison scenarios. The comparisons of wind speeds provided by these two models also confirmed the direct impact of wind forcing on the accuracy of storm tide results.

Constrained by the computational cost, traditionally, the 2-D model was used. Implicitly, it assumes the vertical motion of the coastal water can be neglected relative to horizontal motion and an ideal depth averaged slab of water will act like an actual water

movement. This is over-simplification of the reality and the simulation of 3-D mode should be better than that of 2-D mode for at least the following two reasons: 1) 3-D model has better parameters of bottom stress with the knowledge of vertical velocity structure. Since it uses near-bottom velocity for the bottom stress calculation, the bottom stress is generally more accurate and smaller than that of the 2-D model (if both models use similar bottom friction parameters). This is especially important when surface and bottom currents are counter directional where faster surface currents reduce the difference between wind and water speeds resulting the reduction of momentum transfer rate between air and sea, and vice versa; 2) 3-D model can account for the interior dissipation process better because momentum dispersion is strongly affected by the 3-D vertical shear. As a result, the transfer rate of momentum is different over the water column with different eddy viscosity. Decreasing 2-D model's drag coefficient to match with 3-D model's bottom stress magnitude still doesn't solve the problem that when there is a counter current near the shore, the 2-D models can't simulate the undertow return current as represented in 3-D models. In that case, the directions of bottom stress in 2-D and 3-D models are totally different. In Section 3.2.3.2., Hurricanes Sandy's sensitivity tests of 3-D versus 2-D demonstrate clearly that the 3-D circulation models' results over New York City have higher and more accurate peak water level than the 2-D models.

Coastal surge is driven primarily by momentum transmitted to the water column by winds as well as by momentum that enters to the coastal domain after being transported over distance by waves. Early surge models neglected the wave input and attempted to use local model calibration to compensate the omission. Much of the deficiency now can be remedied by including moment transfers by waves, termed radiation stress gradient,

which arises from a wave momentum flux divergence that is primarily related to wave breaking. This explains why the SCHISM model coupled wind-wave consistently performs better across the board than without the wave. In 3.2.3.3. and 3.3.3., sensitivity tests of "with" and "without" wave model in Hurricane Sandy and Hurricane Irene demonstrated that the increase contributed by wind wave model (effect of wave-induced radiation stress) is on the order of 5-10% of the total water level. Also, the effects of wave radiation stress gradients in larger estuaries (e.g., Chesapeake Bay) and their tributaries are much more complicated than a small-size estuary (e.g., New York Bay). The effects were spatially and temporally varying because of the difference in bathymetry and geometry.

In summary, different model runs were conducted to study the impacts of quality of atmospheric forcings, 3-D modeling, and coupling with the wind wave model. Based on the study, the 3-D barotropic SCHISM storm tide model coupled with wind wave model WWMIII using ECMWF atmospheric forcing performs the best in hindcasting water elevation during both the 2012 Hurricane Sandy and the 2011 Hurricane Irene along coasts and inside the estuary.

Despite overall excellent performance of SCHISM model for simulating storm tide during Hurricane Sandy, we did observe over-prediction of the water level for 1 day after the peak storm surge in New York City. This over-prediction of water level in the later stage of hurricane was also observed in the lower Chesapeake Bay during Hurricane Isabel (not shown). As indicated in Section 3.2.3, it is our belief that the unusual water level drop after the peak surge was due to the sea level set down offshore because of the Ekman transport by the prevailed southerly wind after landfall. To model the sea level set

down properly, it may require more accurate wind after landfall and a 3-D baroclinic model with proper representation of the vertical stratification over the coastal water. Gulf Stream is a baroclinic phenomenon which maintains the geostrophic balance across two sides of the stream. It can influence the water level in the East Coast when Gulf Stream is weakened or strengthened. For example, the sea level at the City of Norfolk rises when Gulf Stream weakens, resulting in the King Tide. Its long-term impacts cannot be simulated without accounting for baroclinic circulation. Other important baroclinic processes like estuarine circulation, vertical stratification on upwelling and down welling occurred in the coastal shelf, and the thermal expansion on long-term sea level rise in the open ocean, are topics of great interest but beyond the scope of this dissertation.

6.1.2. Sub-Grid Inundation Model

In Chapter 4, the ELCIRC model with sub-grid capability was introduced for simulating coastal inundation. The sub-grid modeling is an innovative method by which water elevation and velocity on the high-resolution sub-grid level were obtained through the combination of the high-resolution bathymetry and the elevations and velocities calculated at the coarse computational grid without using the computing resources required to solve the full set of equations. A converging Newton-type iterative scheme is developed in Section 4.3.1 and included into the ELCIRC-sub inundation model. In Section 4.3.2, a benchmark test with wetting/drying analytic solution (Thacker, 1981) was designed and conducted to verify the coding for the new sub-grid nonlinear solver. The time series comparisons of the modeled elevation/velocity and analytical solution show that the model results and analytical solution almost match at all sixteen locations

in terms of phase and amplitude. Overall, the results confirm that, with the proper nonlinear solver and a better scheme in re-constructing the tangential velocity for the numerical simulation of wetting-and-drying process, an excellent accuracy at the sub-grid level can be achieved without resorting to costly and unnecessary grid refinements.

The accurate modeling of the wetting-and-drying dynamic is crucial because without it, the erroneous wave will be reflected from the shoreline and inevitably propagate across the model domain without damping. Regarding the model's efficiency, the new ELCIRC-sub model could reach 1,200 times real time speedup using the College of William and Mary's HPC system. It runs more than 10 times faster than the UnTRIM^2 model for this same set up, enabling coverage of a larger domain and a longer simulation period at a fixed given computational cost.

In Chapter 5, this new ELCIRC-sub model was applied in a realistic simulation during Hurricane Sandy in 2012. For inundation simulation, it consisted 89,853 number of 200-m resolution square base grid and approximately 35 million of sub-grid elements. The 10-day sub-grid inundation simulation was completed within 19 minutes, equal to 720 times real time speedup. In Section 5.2, the comparisons between modeled water level and NOAA observations show that model performance was excellent with the mean absolute error on the order of 5-10 cm. At Kings Point where the storm surge was the largest during Hurricane Sandy, the model accurately caught the peak amplitude, the timing, and the explosive rising of the water level. The error associated with the model-data comparison was less than 0.1 m, which is superior to those of most of the large-scale models such as ADCIRC (USACE, 2015), NYHOPS (Orton et al., 2012), Stony Brook Surge Model^2 (DiLiberto et al., 2011), SLOSH (Forbes et al., 2014), all of which under-

predicted the maximum surge by 0.3 – 1 m (about 10-25% relative error). The ELCIRC-sub's inundation water elevation was also compared with 6 USGS' rapid-deployed water with average error of 10 cm in the peak water level and 8 minutes in the timing.

In Section 5.3, spatial verification of the inundation results by the ELCIRC-sub model was first addressed by comparison with 80 high water mark measurements collected by the USGS. The overall mean absolute errors of model prediction were 0.102 m and 0.325 m for the New York City and New Jersey coasts, respectively. For sub-grid inundation modeling, the ability of visualizing the inundation area is critical because it not only enables the model to depict the parameters for the area of flooding, but also allowed for model results to compare closely with the observation. In this dissertation, QGIS software was used to compare the modeled and observed inundation extent. QGIS functions, as a geographic information system (GIS) software, allows users to analyze and edit spatial information, in addition to composing and exporting graphical maps. QGIS can read in high-resolution DEM as the model domain and high-resolution base maps from Google Map or ArcGIS as the background layer for visualizing street-level inundation. Additional python scripts were also developed to calculate maximum water elevation at all nodes, interpolate elevation onto sub-grid element, and generate final map of modeled inundation extent. Due to QGIS's superior compatibility with Python and its parallel processing capability in development, a near real-time visualization of flooding extent is possible, which can greatly improve operational flood forecast. The maximum extent of inundation from FEMA's spatial flood coverage map was generated through interpolating the data from high water mark, water level gauge, and the best available digital elevation data. With the high-resolution zoom-in comparison of the FEMA map

and the ELCIRC-sub flooding map, the inundated area coverage comparison become possible and was achieved robustly, as shown in Table 13 of Chapter 5. The match percentage between maximum flood extents obtained from ELCIRC-sub model versus from FEMA were calculated area-to-area for the entire New York City and local important areas, New Jersey coastline within model domain, and the total flooded area around NJ coast and NYC. Overall, the model matched approximately 75% with FEMA map, with higher than 80% match in local areas such as lower Manhattan and LGA airport, which is comparable to a previous study (Loftis, 2014).

The sub-grid modeling approach may be further improved by implementing information exchange of bottom friction between sub-grid and base-grid using the conveyance approach (Casulli and Stelling, 2011). When we assume the inundation flow is frictionally dominated and the pressure gradient is constant over each cell element (note, the velocity, friction, and depth are variable at the side), the following conservative formula can be obtained:

$$\|u_j\| = \Omega_j \frac{\|U\|}{\boldsymbol{\Omega}} \qquad (1)$$

$$\text{with} \quad \|U\| = \frac{\sum_{j=1}^{J} h_j \|u_j\|}{\sum_{j=1}^{J} h_j} \quad \text{and} \quad \boldsymbol{\Omega} = \frac{\sum_{j=1}^{J} h_j \Omega_j}{\sum_{j=1}^{J} h_j} \qquad (2)$$

Where ($||u_j||$, Ω_j) and ($||U||$, Ω) are the velocity and conveyance for the sub-grid and base grid, respectively, hj is the depth in this sub-grid, and J defines the total number of wet sub-grids within a base grid. This can thus be used to determine the spatial varying friction parameter for the base grid, an important feedback from the sub-grid. Computational-wise, this is done without having to resort to using a fine-scale computational mesh.

For mitigating the hazard of coastal inundation, it is desirable to know how much the marshes and coastal forests can slow the inland surge penetration. The sub-grid model coupling with Submerged Aquatic Vegetation (SAV) will be a great extension to quantify the SAV induced friction effects on both vertical and lateral structure of the currents. Another aspect of improvement of ELCIRC-sub is to include the effect of the precipitation. In this dissertation, the precipitation was not added because the water on the ground both for Hurricane Sandy and Irene is quite saturated. On other cases, the precipitation could cause riverine flooding (from upstream of watershed) and exacerbate the coastal plain already battered by the storm surge.

6.2. Conclusions

In part I, the 3-D barotropic storm tide model SCHISM was developed which covers the entire U.S. East Coast and Gulf Coasts, with open ocean boundary aligning along the 60-degree West longitude. The model forced with high-resolution ECMWF atmospheric fields, simulated storm surge in 3-D barotropic mode rather than the traditional 2-D vertical average mode and was coupled with WWMIII to account for wind wave effects. The model-data comparison in the Hurricane Sandy simulation revealed that the fully coupled 3-D wave-current interaction model using the ECMWF atmospheric forcing performs better than 2-D models or 3-D models using the NAM atmospheric forcing. The similar model setup was tested again for Hurricane Irene. Again, the results are excellent and robust when comparing with observed water levels along the southeast coastline and inside Chesapeake Bay.

In part II, the sub-grid inundation model ELCIRC-sub is developed from the original finite-volume based hydrodynamic model ELCIRC by utilizing the sub-grid technology to combine with high-resolution topography/bathymetry data into the traditional model grid and delivering the street-level inundation prediction. The coding to interpolate high-resolution DEM and a new and efficient non-linear solver were developed and embedded into ELCIRC model. The ELCIRC-sub was validated by a benchmark test with a wetting/drying analytic solution. The model is then used to simulate coastal flooding during Hurricane Sandy. Both temporal and spatial analysis show excellent match between observations and model results. It should be noted that the ELCIRC-sub developed here can cover much larger model domain with better computational efficiency than UnTRIM^2 which was used in the previous studies.

To summarize, the dissertation has addressed the primary objectives in improving modeling storm surge and coastal inundation as follows:

a. A wind-wave coupled unstructured-grid 3-D storm tide SCHISM model was applied to a large domain with an open boundary aligned to the 60-degree West longitude covering the entire U.S. East Coast and Gulf Coast. The excellent performance (accuracy and robustness) of the model in hindcasting storm tide and wind wave during Hurricane Sandy (2012) and Hurricane Irene (2011) demonstrates its feasibility for operational forecast.

b. The sensitivity of the model performance to different practices among NAM and ECMWF atmospheric models, 2-D versus 3-D, and "with wave" versus "no-wave" storm surge simulations was identified by analyzing model results from different runs with various set ups. The result indicated that the coupled-wind wave 3-D, barotropic SCHISM model forced by ECMWF wind has the best performance.

c. The sub-grid modeling capability has been developed and incorporated into ELCIRC-sub model for simulating the coastal inundation. The newly developed nonlinear solver enhanced the accuracy for simulating wetting-and-drying processes while the parallel computing enables larger watershed coverage and greater efficiency.

d. The developed ELCIRC-sub model has been rigorously verified by benchmark wetting/drying tests with analytic solution. The model was then applied in the realistic street-level inundation simulation in the greater New York City during Hurricane Sandy. The simulation has been visualized and compared with water gauges and FEMA flooding map with excellent results. It demonstrated that the sub-grid modeling in ELCIRC-sub model is a viable tool for reducing the risk of coastal inundation in the future.

APPENDICES

Appendix 1. Definition of Statistical Formulas

The following statistical formulas have been utilized to assess the accuracy of the large-scale storm tide model and sub-grid inundation model for both tidal calibrations and storm surge simulations in this study.

X represents the water level time series data, while N is the total number of model-data comparison pairs. The subscripts "mod" denotes the model results and "obs" are the observations.

(1) The Root-Mean-Square Error (RMSE) is calculated as:

$$RMSE = \sqrt{\left\{\frac{1}{N}\sum_{i=1}^{N}(X_{mod} - X_{obs})^2\right\}}$$

(2) The Mean Absolute Error (MAE) is calculated as:

$$MAE = \frac{1}{N}\sum_{i=1}^{N}|X_{mod} - X_{obs}|$$

(3) The R-squared (R^2) is calculated as:

$$R^2 = 1 - \frac{\sum_{i=1}^{N}(X_{mod} - X_{obs})^2}{\sum_{i=1}^{N}(X_{obs} - \overline{X_{obs}})^2}$$

Appendix 2. Tidal Calibration and Harmonic Analysis

(1) Astronomical tide simulation between 09/01/2012 and 11/30/2012

Time series of tidal calibration are shown in Figure 78-80. The modeled tides match well with NOAA prediction at all 9 locations. Statistical values such as correlation coefficient (R^2), Root-Mean-Square Error (RMSE), and Mean Absolute Error (MAE) were calculated and presented in Table 14. SCHISM tidal simulation is quite accurate with R^2 values larger than 0.98 and RMSE less than 6 cm at all stations.

Harmonic analysis was also conducted via MATLAB using the 'T-Tide' software (Pawlowicz et al., 2002), on tidal results from the hourly model outputs between September and November, 2012 at these stations: Montauk, NY, Bridgeport, CT, Kings Point, NY, The Battery, NY, Sandy Hook, NJ, Atlantic City, NJ, Cape May, NJ, CBBT, VA, and Duck, NC. The analysis results for phase and amplitude of 5 major constituents' (M_2, N_2, S_2, O_1, and K_1) phase and amplitude are shown in Table 15 and Table 16, respectively.

In the tidal amplitude comparison, the SCHISM model simulates the amplitude of the dominant M_2 tidal constituent excellently at all of the 9 stations with a difference on the order of 1-4 cm (Table 15). The principal solar diurnal constituent, S_2, had a maximum difference of 2 cm between the modeled tide and the NOAA prediction. Stations along the open coast had a better comparison, while those located inside estuaries were observed to have relatively larger error in tidal amplitude. As for the diurnal tidal amplitudes, the maximum differences for the 9 stations were 1 cm for O_1, and 2 cm for K_1.

In the tidal phase comparison, Table 16 presents the difference of tidal phase between modeled tide and NOAA predicted tide. The difference for M_2, N_2, and S_2 is 1-4 degrees, 1-5 degrees, and 2-5 degrees, respectively. Sandy Hook, NJ, observed a larger shift in M_2 tide by 4 degree, accounting for much of the deviation. The phase differences for the diurnal constituents, O1 and K1, were 2-6 degree, 1-5 degree, respectively. The excellent tidal harmonic analysis results for both amplitude and phase suggest that the large-scale SCHISM model grid is sufficient when compared with NOAA prediction data. Thus, the large-scale SCHISM grid developed for the hindcaste prediction of the 2012 Hurricane Sandy is quite capable of simulating long-period wave propagation along the open coast and inside New York Bay.

Table 14: Statistical evaluation of SCHISM modeled tide and NOAA predicted tide for 9 tidal gauges.

Stations	R^2	RMSE (m)	MAE (m)
Montauk, NY	0.983	0.049	0.040
Bridgeport, CT	0.992	0.060	0.053
Kings Point, NY	0.988	0.059	0.046
The Battery, NY	0.984	0.043	0.032
Sandy Hook, NJ	0.982	0.059	0.048
Atlantic City, NJ	0.991	0.052	0.044
Cape May, NJ	0.992	0.043	0.035
CBBT, VA	0.991	0.051	0.044
Duck, NC	0.986	0.045	0.039

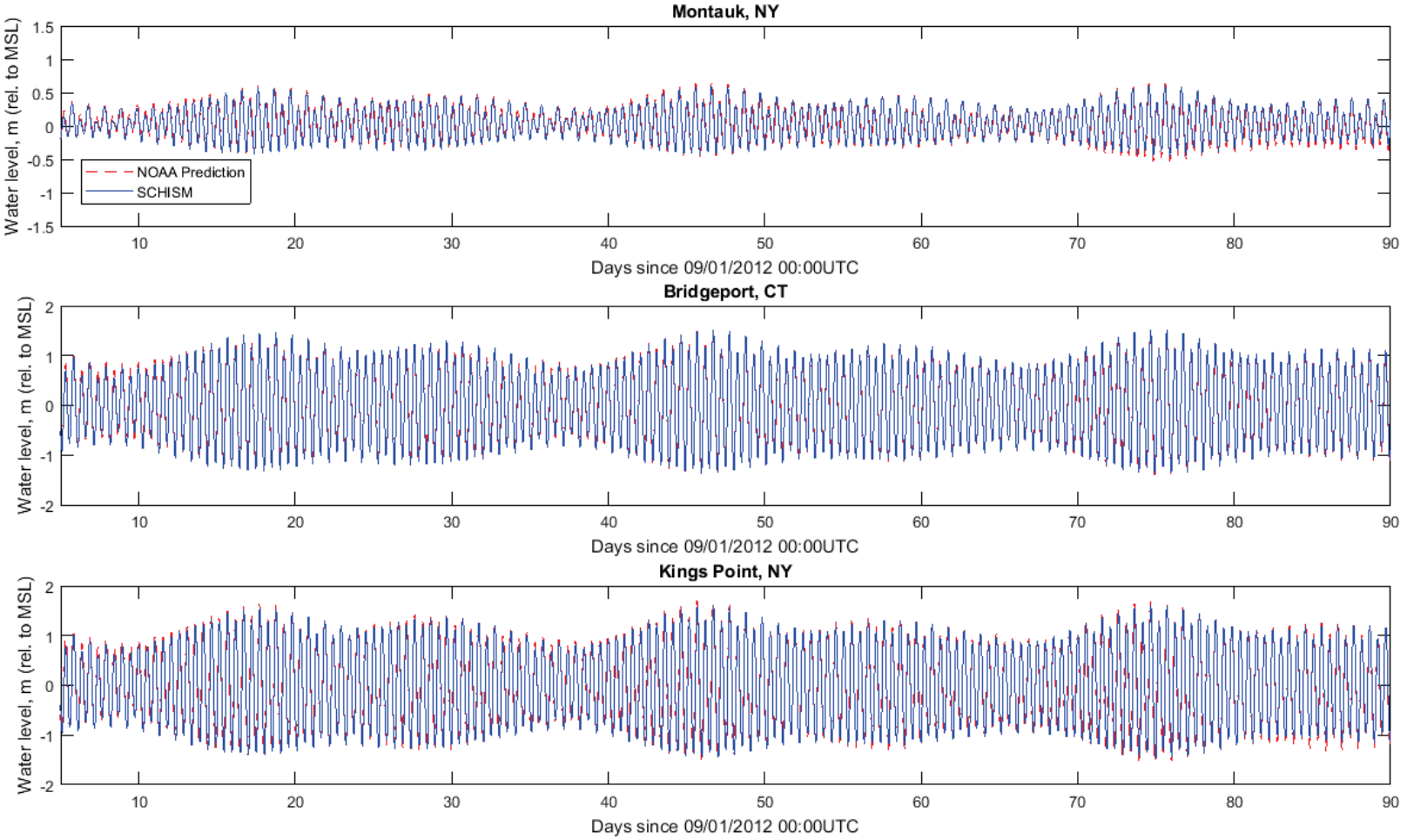

Figure 78: Comparisons of NOAA predicted tide and SCHISM tide simulation results in Long Island Sound in Sept - Nov, 2012.

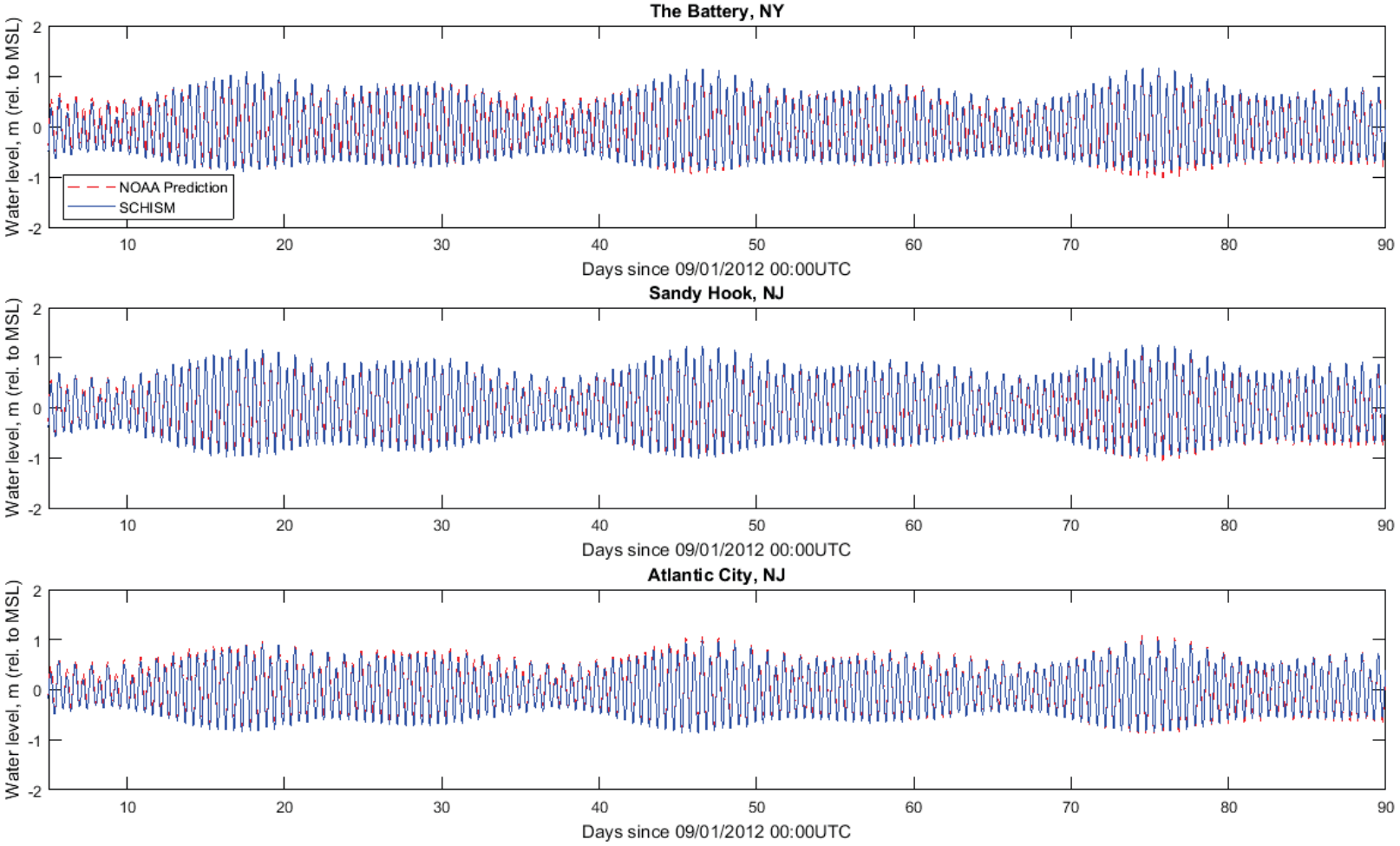

Figure 79: Comparisons of NOAA predicted tide and SCHISM tide simulation results in NY and NJ coasts in Sept - Nov, 2012.

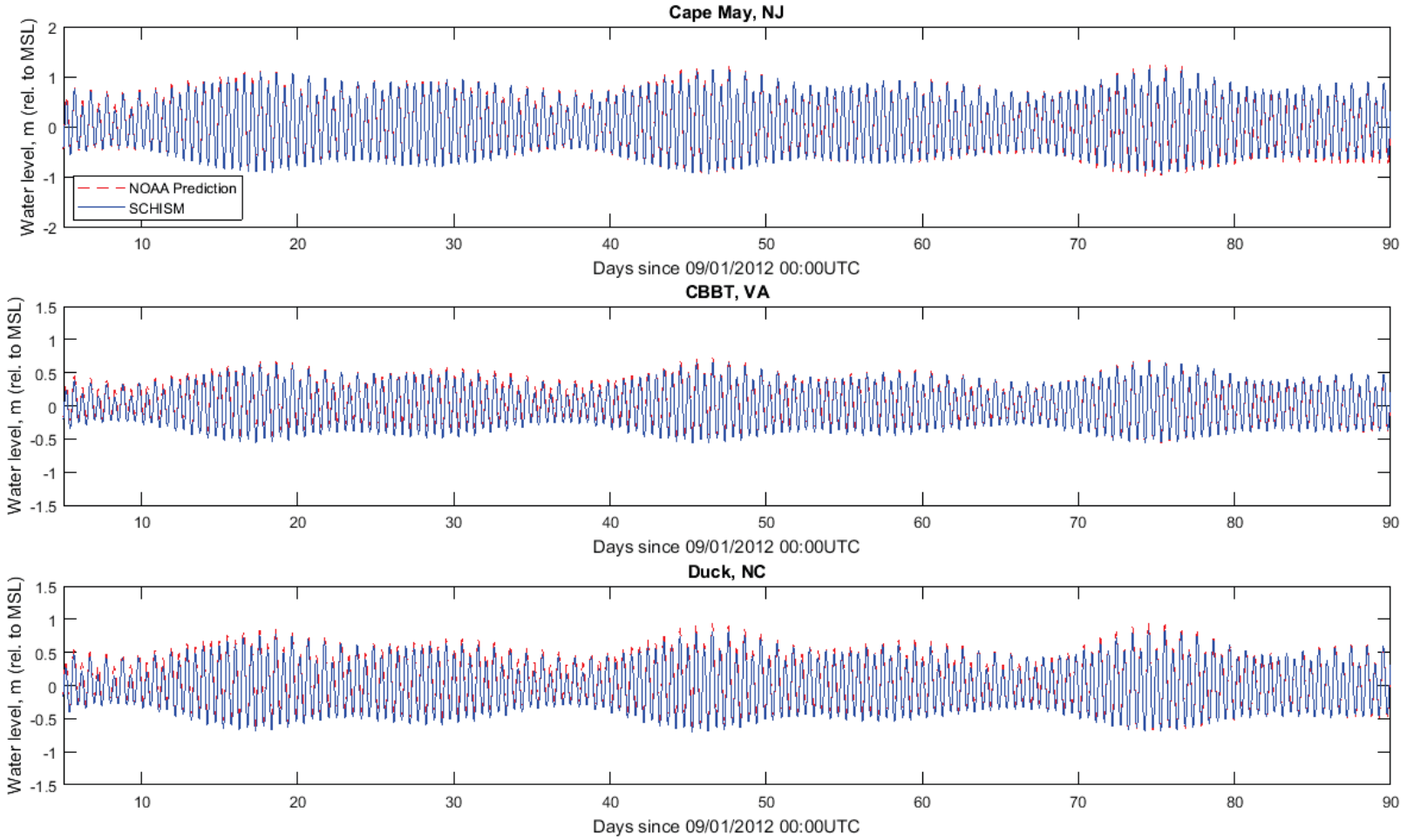

Figure 80: Comparisons of NOAA predicted tide and SCHISM tide simulation results in NJ, VA and NC coasts in Sept - Nov, 2012.

Table 15: Comparisons of tidal amplitudes in meters relative to MSL for 3 major semidiurnal constituents (top) and 2 major diurnal tidal constituents (bottom) between NOAA predicted tide and SCHISM modeled tide at 9 stations.

Amplitude	M2			N2			S2		
Station	**Model**	**NOAA Prediction**	**Difference**	**Model**	**NOAA Prediction**	**Difference**	**Model**	**NOAA Prediction**	**Difference**
Montauk	0.2925	0.3080	-0.0155	0.0743	0.0827	-0.0084	0.0625	0.0678	-0.0053
Bridgeport	0.9772	1.0128	-0.0356	0.1909	0.2116	-0.0207	0.1468	0.1515	-0.0047
Kings Point	1.1495	1.1677	-0.0182	0.2355	0.2564	-0.0209	0.1870	0.1827	0.0042
The Battery	0.6584	0.6821	-0.0237	0.1381	0.1636	-0.0255	0.1151	0.1267	-0.0116
Sandy Hook	0.7308	0.7042	0.0266	0.1647	0.1670	-0.0023	0.1468	0.1306	0.0162
Atlantic City	0.6050	0.6075	-0.0025	0.1366	0.1488	-0.0121	0.1160	0.1144	0.0016
Cape May	0.7016	0.7306	-0.0290	0.1495	0.1688	-0.0193	0.1143	0.1212	-0.0068
CBBT	0.4053	0.3889	0.0164	0.0909	0.0954	-0.0045	0.0736	0.0688	0.0048
Duck	0.4967	0.5010	-0.0043	0.1147	0.1214	-0.0068	0.0909	0.0859	0.0049

Cont'd	O1			K1		
Station	**Model**	**NOAA Prediction**	**Difference**	**Model**	**NOAA Prediction**	**Difference**
Montauk	0.0377	0.0505	-0.0128	0.0856	0.0705	0.0152
Bridgeport	0.0477	0.0600	-0.0123	0.1134	0.0903	0.0231
Kings Point	0.0514	0.0622	-0.0108	0.1211	0.0973	0.0237
The Battery	0.0548	0.0490	0.0058	0.0855	0.0991	-0.0136
Sandy Hook	0.0625	0.0510	0.0115	0.0987	0.1003	-0.0015
Atlantic City	0.0768	0.0706	0.0061	0.0883	0.1064	-0.0181
Cape May	0.0777	0.0791	-0.0013	0.0829	0.1028	-0.0199
CBBT	0.0394	0.0421	-0.0027	0.0660	0.0605	0.0056
Duck	0.0574	0.0552	0.0022	0.0889	0.0871	0.0018

Table 16: Comparisons of tidal phases in degree for 3 major semidiurnal constituents (top) and 2 major diurnal tidal constituents (bottom) between NOAA predicted tide and SCHISM modeled tide at 9 stations.

Phase	M2			N2			S2		
Station	**Model**	**NOAA Prediction**	**Difference**	**Model**	**NOAA Prediction**	**Difference**	**Model**	**NOAA Prediction**	**Difference**
Montauk	68.35	71.07	-2.72	24.45	28.97	-4.52	47.57	51.43	-3.85
Bridgeport	134.67	134.06	0.62	91.99	94.79	-2.80	128.09	125.13	2.96
Kings Point	142.01	140.16	1.85	102.89	99.20	3.69	134.59	130.50	4.09
The Battery	42.60	43.37	-0.77	4.54	5.44	-0.90	39.89	35.32	4.57
Sandy Hook	33.90	30.37	3.53	355.72	354.74	0.97	29.45	25.92	3.53
Atlantic City	17.42	19.76	-2.34	339.40	342.22	-2.82	13.18	10.72	2.46
Cape May	52.97	53.04	-0.07	13.34	16.05	-2.71	49.70	45.35	4.35
CBBT	42.50	45.36	-2.86	5.49	7.69	-2.20	39.56	37.65	1.91
Duck	20.11	22.34	-2.23	340.18	344.84	-4.66	15.14	13.87	1.27

Cont'd	O1			K1		
Station	**Model**	**NOAA Prediction**	**Difference**	**Model**	**NOAA Prediction**	**Difference**
Montauk	354.90	358.87	-3.97	53.39	57.30	-3.91
Bridgeport	9.45	11.40	-1.95	68.09	69.66	-1.57
Kings Point	10.12	12.60	-2.48	74.98	70.05	4.93
The Battery	332.98	327.91	5.07	62.49	59.22	3.27
Sandy Hook	323.36	323.96	-0.61	57.38	54.45	2.93
Atlantic City	322.58	317.80	4.78	56.55	60.33	-3.78
Cape May	343.07	337.33	5.74	74.36	78.53	-4.17
CBBT	354.02	358.41	-4.39	65.19	62.90	2.29
Duck	340.91	344.44	-3.53	52.81	51.69	1.12

(2) Astronomical tide simulation between 07/01/2011 and 09/30/2011

Time series comparisons of tidal simulation results and NOAA prediction are shown in Figures 81 and 82. Statistical evaluation at all stations are presented in Table 17. R^2 is larger than 0.96 and the average RMSE is 4 cm at all stations. At the upper Bay stations such as Baltimore and Cambridge, the error was relatively larger than at the middle and lower Bay stations, but the results were still very reasonable. Harmonic analysis (Tables 18 - 21) of tidal amplitude and tidal phase between modeled tide and NOAA predicted tide for the 5 major harmonic constituents show that the SCHISM model accurately simulates tidal propagation across the Western Atlantic to the U.S. coasts and all the way to the upper Chesapeake Bay.

In the tidal amplitude comparison, the SCHISM model simulates the dominant M_2 constituent excellently at all of the 12 stations with a diffrence on the order of 1-4 cm (Table 18 and Table 20). At Baltimore, an upper Bay station, the error is relatively larger, due to its unique location inside narrow tributaries. At Charleston, the discrepancy in amplitude is also larger, because the tidal gauge is located inside a narrow river where the model grid doesn't fully resolve it. The error in the N_2 constituent magnitude is smaller than 1 cm at all stations. The principal solar diurnal constituent, S_2, has maximum errors of 2 cm inside of the Chesapeake Bay and 3 cm outside of the Bay. Generally, stations along the open coast had a better comparison than locations inside of the Bay; and stations in the lower Bay had better results than stations in the upper Bay. As for the diurnal tidal amplitudes, the maximum differences for the 12 stations were both 1 cm for both the O_1 and K_1 constituents.

In the tidal phase comparison, Tables 19 and 21 present the difference of tidal phase between modeled tide and NOAA predicted tide inside Chesapeake Bay and outside along coasts, respectively. For example, the error for M_2 tide is 1-7 degrees. Baltimore and Charleston showed larger differences in M_2 tide phase by 4-7 degrees, accounting for much of the deviation. The phase differences for the diurnal constituents were less than 4 degrees at most stations. The excellent tidal harmonic analysis results again suggest that the large-scale SCHISM model grid is sufficient for hindcasting 2011 Hurricane Irene along the open coast and inside Chesapeake Bay.

Table 17: Statistical evaluation of SCHISM modeled tide and NOAA predicted tide at 12 tidal gauges.

Stations	R^2	RMSE (m)	MAE (m)
Baltimore, MD	0.965	0.075	0.054
Cambridge, MD	0.962	0.069	0.049
Annapolis, MD	0.964	0.069	0.052
Lewisetta, VA	0.964	0.058	0.040
Windmill Point, VA	0.971	0.057	0.402
Sewells Point, VA	0.991	0.042	0.357
Kiptopeke, VA	0.989	0.048	0.036
CBBT, VA	0.988	0.050	0.036
Duck, NC	0.983	0.052	0.042
Wrightsville Beach	0.979	0.066	0.054
Springmaid Pier	0.977	0.070	0.053
Charleston, SC	0.961	0.073	0.064

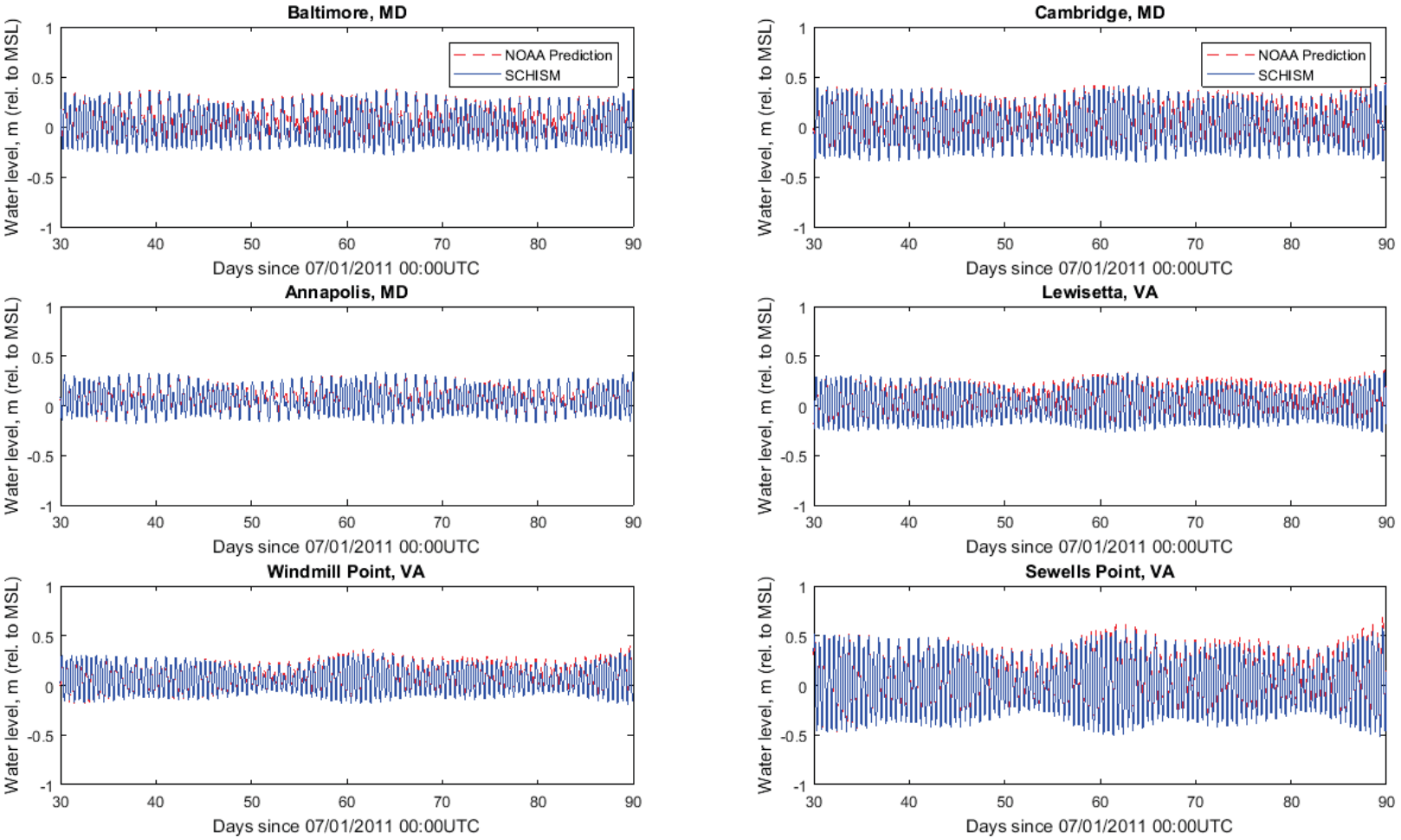

Figure 81: Comparisons of NOAA predicted tide and SCHISM tide simulation results inside Chesapeake Bay in Jul-Sept, 2011.

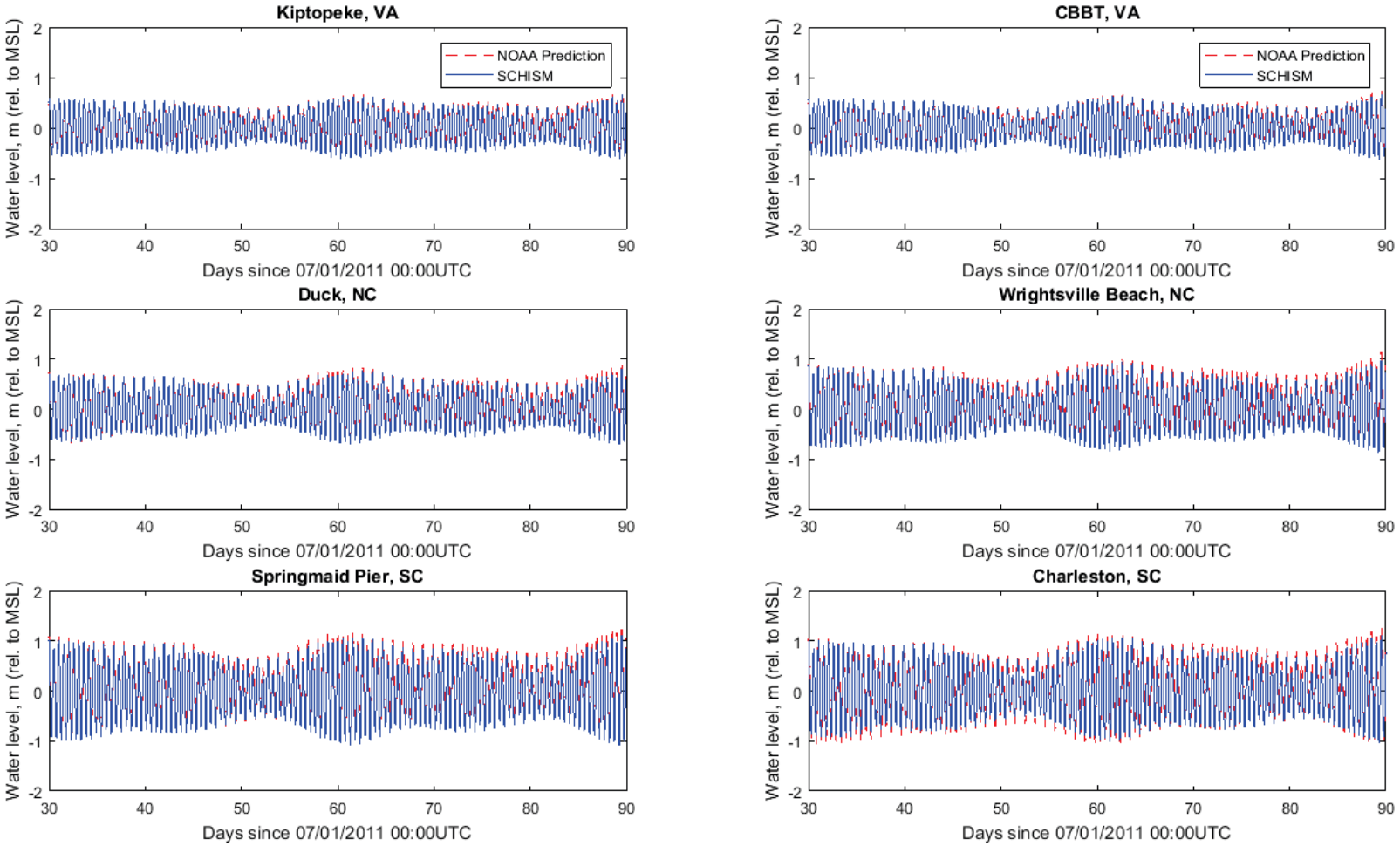

Figure 82: Comparisons of NOAA predicted tide and SCHISM tide simulation results in VA and NC coasts in Jul-Sept, 2011.

Table 18: Comparisons of tidal amplitudes in meters relative to MSL for 3 major semidiurnal constituents (top) and 2 major diurnal tidal constituents (bottom) between NOAA predicted tide and SCHISM modeled tide at 6 stations inside Chesapeake Bay.

Amplitude	M2			N2			S2		
Station	**Model**	**NOAA Prediction**	**Difference**	**Model**	**NOAA Prediction**	**Difference**	**Model**	**NOAA Prediction**	**Difference**
Baltimore	0.2002	0.1593	0.0410	0.0423	0.0332	0.0090	0.0329	0.0220	0.0109
Cambridge	0.2770	0.2395	0.0375	0.0544	0.0458	0.0086	0.0455	0.0315	0.0140
Annapolis	0.1493	0.1391	0.0102	0.0324	0.0288	0.0036	0.0254	0.0213	0.0041
Lewisetta	0.2138	0.1843	0.0295	0.0452	0.0395	0.0057	0.0356	0.0258	0.0097
Windmill Point	0.1746	0.1751	-0.0005	0.0404	0.0372	0.0032	0.0324	0.0265	0.0060
Sewells Point	0.3699	0.3663	0.0036	0.0811	0.0798	0.0013	0.0683	0.0578	0.0105

Cont'd	O1			K1		
Station	**Model**	**NOAA Prediction**	**Difference**	**Model**	**NOAA Prediction**	**Difference**
Baltimore	0.0640	0.0553	0.0086	0.0891	0.0812	0.0079
Cambridge	0.0462	0.0386	0.0076	0.0637	0.0603	0.0035
Annapolis	0.0539	0.0476	0.0064	0.0744	0.0709	0.0035
Lewisetta	0.0225	0.0190	0.0036	0.0335	0.0231	0.0104
Windmill Point	0.0221	0.0227	-0.0007	0.0394	0.0290	0.0103
Sewells Point	0.0409	0.0415	-0.0007	0.0652	0.0531	0.0121

Table 19: Comparisons of tidal phases in degrees for 3 major semidiurnal constituents (top) and 2 major diurnal tidal constituents (bottom) between NOAA predicted tide and SCHISM modeled tide at 6 stations inside Chesapeake Bay.

Phase	M2			N2			S2		
Station	**Model**	**NOAA Prediction**	**Difference**	**Model**	**NOAA Prediction**	**Difference**	**Model**	**NOAA Prediction**	**Difference**
Baltimore	8.239	5.201	3.038	131.053	133.313	-2.260	9.469	7.351	2.118
Cambridge	287.390	291.297	-3.907	57.430	60.704	-3.274	288.670	286.171	2.499
Annapolis	321.773	319.744	2.029	86.907	89.469	-2.562	322.296	320.190	2.105
Lewisetta	204.563	204.622	-0.060	327.721	331.332	-3.610	200.042	199.797	0.245
Windmill Point	131.817	131.524	0.293	260.180	263.217	-3.037	121.721	120.898	0.823
Sewells Point	73.168	74.946	-1.778	204.390	206.755	-2.365	68.442	71.286	-2.844

Cont'd	O1			K1		
Station	**Model**	**NOAA Prediction**	**Difference**	**Model**	**NOAA Prediction**	**Difference**
Baltimore	107.370	110.211	-2.841	303.649	303.192	0.457
Cambridge	87.585	90.870	-3.285	277.842	281.800	-3.958
Annapolis	98.343	100.774	-2.431	290.840	292.853	-2.012
Lewisetta	32.806	33.833	-1.026	219.759	223.842	-4.083
Windmill Point	338.676	341.519	-2.844	164.514	163.474	1.040
Sewells Point	316.383	319.972	-3.589	138.276	135.793	2.484

Table 20: Comparisons of tidal amplitudes in meters relative to MSL for 3 major semidiurnal constituents (top) and 2 major diurnal tidal constituents (bottom) between NOAA predicted tide and SCHISM modeled tide at 6 stations outside Chesapeake Bay along VA and NC coasts.

Amplitude	M2			N2			S2		
Station	**Model**	**NOAA Prediction**	**Difference**	**Model**	**NOAA Prediction**	**Difference**	**Model**	**NOAA Prediction**	**Difference**
Kiptopeke	0.4201	0.3882	0.0319	0.0948	0.0864	0.0084	0.0793	0.0615	0.0178
CBBT	0.4153	0.3801	0.0352	0.0954	0.0889	0.0066	0.0795	0.0629	0.0166
Duck	0.4837	0.4906	-0.0069	0.1124	0.1119	0.0005	0.0902	0.0762	0.0140
Wrightsville Beach	0.6002	0.5933	0.0069	0.1384	0.1400	-0.0016	0.1070	0.0913	0.0157
Springmaid Pier	0.7368	0.7413	-0.0046	0.1688	0.1759	-0.0072	0.1321	0.1099	0.0222
Charleston	0.7328	0.7831	-0.0503	0.1643	0.1707	-0.0064	0.1288	0.1013	0.0275

Cont'd	O1			K1		
Station	**Model**	**NOAA Prediction**	**Difference**	**Model**	**NOAA Prediction**	**Difference**
Kiptopeke	0.0463	0.0452	0.0010	0.0760	0.0635	0.0125
CBBT	0.0454	0.0441	0.0012	0.0741	0.0643	0.0098
Duck	0.0623	0.0582	0.0041	0.0936	0.0942	-0.0006
Wrightsville Beach	0.0702	0.0680	0.0022	0.0965	0.1012	-0.0047
Springmaid Pier	0.0752	0.0717	0.0034	0.1030	0.1110	-0.0080
Charleston	0.0775	0.0778	-0.0003	0.1057	0.1153	-0.0096

Table 21: Comparisons of tidal phases in degrees for 3 major semidiurnal constituents (top) and 2 major diurnal tidal constituents (bottom) between NOAA predicted tide and SCHISM modeled tide at 6 stations outside Chesapeake Bay along VA and NC coasts.

Phase	M2			N2			S2		
Station	**Model**	**NOAA Prediction**	**Difference**	**Model**	**NOAA Prediction**	**Difference**	**Model**	**NOAA Prediction**	**Difference**
Kiptopeke	57.932	60.707	-2.775	186.028	190.983	-4.955	50.760	53.779	-3.019
CBBT	45.899	49.246	-3.347	174.261	179.415	-5.154	38.697	42.320	-3.623
Duck	24.161	26.266	-2.105	152.174	156.517	-4.343	15.176	19.613	-4.437
Wrightsville Beach	17.711	21.342	-3.632	146.492	151.784	-5.291	6.107	10.970	-4.863
Springmaid Pier	21.622	25.848	-4.226	151.038	156.233	-5.196	9.558	14.970	-5.412
Charleston	31.782	38.618	-6.836	167.289	173.448	-6.159	24.185	31.995	-7.811

Cont'd	O1			K1		
Station	**Model**	**NOAA Prediction**	**Difference**	**Model**	**NOAA Prediction**	**Difference**
Kiptopeke	302.226	308.757	-6.531	130.167	128.609	1.558
CBBT	298.213	304.154	-5.940	123.042	118.335	4.707
Duck	284.879	287.611	-2.732	112.407	109.176	3.231
Wrightsville Beach	287.820	287.354	0.466	120.893	124.484	-3.591
Springmaid Pier	288.735	287.867	0.868	122.325	127.492	-5.167
Charleston	296.170	298.159	-1.989	132.324	140.137	-7.813

Appendix 3. Alternative bottom drag coefficient for 3-D models

As explained in Section 2.1.2., the bottom drag coefficient is one of the key parameters in formulating bottom shear stress. In Chapter 3, we adopted the Manning's n formulation to C_{db} as shown here:

$$C_{db} = \frac{n^2 * g}{H^{\frac{1}{3}}} \qquad (1)$$

where n is Manning's value, g is gravity acceleration, and H is the water depth. The Manning's n values in general are not known a priori. In the present approach they were obtained by calibrating with astronomical tide simulations and the same Manning's n values (thus the derived C_{db}) were used for both 2-D SCHISM and 3-D SCHSIM storm tide model simulation. This approach yields reasonable model results comparing with NOAA predicted astronomical tide and observed storm tide water elevations.

In 3-D models, C_{db} can be determined by specifying the bottom roughness height in a logarithmic bottom boundary layer. In this formulation, a roughness height formulation equivalent to the Manning's n can also be obtained.

(a) The logarithmic boundary layer profile

In the wall-bounded shear flow, the key concepts of the shear flow reside in three layers: inner layer (dominated by viscous shear), outer layer (dominated by turbulent shear), overlap layer (dominated by both viscous and turbulent flow).

For the inner layer, the law of the wall states that velocity is determined by the wall shear stress τ_w , density ρ , dynamic viscosity μ , and distance from the wall y (Prandtl, 1933):

$$u = f(\tau_w, \rho, \mu, y) \qquad (2)$$

In the outer layer, the velocity defect law by von Karman (1930) states that the difference between the free stream velocity u_∞ and local velocity u is independent of dynamic viscosity but depends on the boundary layer thickness (von Karman, 1930):

$$u_\infty - u = F(\tau_w, \rho, y, \delta) \quad (3)$$

where δ is the boundary layer thickness.

In the overlap layer, (2) and (3) are assumed to merge together smoothly over this overlapping region (Millikan, 1938):

$$u_{[inner\ layer]} = u_{[outer\ layer]} \quad (4)$$

The friction velocity is defined as $u_* = \sqrt{\frac{\tau_w}{\rho}}$. Based on the dimension analysis (Kundu et al., 2004), the law of the wall yields:

$$\frac{u}{u_*} = f\left(\frac{yu_*}{\upsilon}\right) = f(y_+) \quad (5)$$

where $y_+ = \frac{yu_*}{\upsilon}$.

Then, according to the velocity defect law, we can get:

$$\frac{u_\infty - u}{u_*} = F\left(\frac{y}{\delta}\right) = F(\xi) \quad (6)$$

where $\xi = \frac{y}{\delta}$.

From (5) and (6), we find that y is scaled quite differently in the inner and outer layers. By taking the limit $y_+ \to \infty$ and $\xi \to 0$ simultaneously, the solutions in inner and outer layers can be matched together. Instead of matching velocity directly, their gradients can be matched to yield:

$$-\xi \frac{dF}{d\xi} = (y_+) \frac{df}{dy_+} = \frac{1}{k} \quad (7)$$

where $\kappa = 0.4$ is von Karman's constant.

Integrating (7) yields:

$$f(y_+) = \frac{1}{\kappa} \ln(y_+) + A \quad (8)$$

$$F(\xi) = -\frac{1}{\kappa} \ln(\xi) + B \quad (9)$$

Substituting velocity expression (5) and (6) into (8) and (9) respectively yields:

$$\frac{u}{u_\infty} = \frac{1}{\kappa} \ln\left(\frac{y u_*}{\upsilon}\right) + A \quad (10)$$

$$\frac{u - u_\infty}{u_*} = \frac{1}{\kappa} \ln\left(\frac{y}{\delta}\right) + B' \quad (11)$$

So, the forgoing method justifies the logarithmic profile near a wall. The boundary layer flow will be analyzed using only the logarithmic expression as an approximation. Based on (10) and (11), we can get the velocity gradient as:

$$\frac{du}{dy} = \frac{1}{\kappa} \frac{u_*}{y} \quad (12)$$

Then the integration over y gives:

$$u = \frac{u_*}{\kappa} \ln(y) + constant \quad (13)$$

Near a rough wall, if y_0 denotes the bottom roughness, Eq. 13 would become:

$$u = \frac{u_*}{\kappa} \ln\left(\frac{y}{y_0}\right) \quad (14)$$

which suggests that the wall-bounded turbulent shear stress flow can be approximated by the logarithmic profile and the shear stress at the wall can be explicitly expressed if the bottom roughness is provided.

(b) An alternative bottom drag coefficient for 3-D models

Based on the formulation of wall shear stress $\tau_w = \rho u_*^2$ and Eq. 14:

$$\tau_w = \rho u_*^2 = \rho \left(\frac{u\kappa}{\ln\left(\frac{z}{z_0}\right)} \right)^2 = \rho \left(\frac{\kappa^2}{\ln\left(\frac{z}{z_0}\right)} \right) u^2 \quad (15)$$

we can get the expression of bottom drag coefficient in 3-D models:

$$C_{db} = \left(\frac{1}{\kappa} \ln \frac{\delta_b}{z_0} \right)^{-2} \quad (16)$$

where δ_b is the thickness of the bottom computational cell (if the bottom is sufficiently resolved in SCHSIM that the bottom cell is inside the boundary layer), z_0 is the bottom roughness, and $\kappa = 0.4$ is von Karman's constant.

Combining Eqs. (1) and (16):

$$\left(\frac{1}{\kappa} \ln \frac{\delta_b}{z_0} \right)^{-2} = \frac{n^2 * g}{H^{\frac{1}{3}}} \quad (17)$$

we obtained the equivalent bottom roughness z_0 in a 3-D model based on 2-D Manning's n value:

$$z_0 = \delta_b * \exp\left(-\frac{\kappa * H^{\frac{1}{6}}}{\sqrt{g} * n} \right) \quad (18)$$

The equation (18) yields reasonable bottom roughness values in shallow water (e.g., less than 50 m) while the bottom roughness in the deeper water calculated from equation (18)

tends to be very small. (e.g., the bottom roughness is on the order of 10^{-7} m at 5,000 m deep).

Thus, if the reference values of bottom roughness are given for the 3-D models, Equation (16) can be used to obtain C_{db} directly. If this information is not available, the C_{db} can be obtained by converting from Manning's n value based on equation (18).

REFERENCES

1. Abgrall, R. (2006). Residual distribution schemes: Current status and future trends. *Computers & Fluids*, 35(7), 641-669.
2. ADCIRC Tidal Database. (2011). Version ec2001: http://adcirc.org/products/adcirc-tidal-databases.
3. Aldrighetti, E. and P. Zanolli. (2005). A high-resolution scheme for flows in open channels with arbitrary cross-section. *Int. J. Numer. Meth. Fluids*, 47: 817-824.
4. Andrews, D. G., and M. E. McIntyre. (1978a). "On wave-action and its relatives". *J. Fluid Mech.*, 89, 647–664. Corrigendum Vol 95, pp. 796; also Vol. 106, pp.331.
5. Andrews, D. G., and M.E. McIntyre. (1978b). An exact theory of nonlinear waves on a Lagrangian- mean flow. *J. Fluid Mech.*, 89, 609-646.
6. Blumberg, A.F. and G.L. Mellor. (1987). A description of a three dimensional coastal ocean circulation model. In N. Heaps (ed.), Three Dimensional Coastal Ocean Circulation Models, American Geophysical Union, Washington, D.C., 4:1-16.
7. Blumberg, A., L. Khan, A., and J.P. St. John. (1999). Three-dimensional hydrodynamic model of New York Harbor region. *Journal of Hydraulic Engineering*, 125(8): 799-816.
8. Bretherton, F. P., and C. J. R. Garrett (1968). Wavetrains in inhomogeneous moving media, *Proc. R. Soc. London A*, 302(1471), 529–554, doi:10.1098/rspa.1968.0034.

9. Casulli, V. (1999). A semi-implicit finite difference method for non-hydrostatic, free-surface flows, *International Journal for Numerical Methods in Fluids* 30, 425-440.

10. Casulli, V. (2009). A high resolution wetting and drying algorithm for free-surface hydrodynamics. *Int. J. Numer. Methods Fluid* 2009, *60*, 391–408.

11. Casulli, V. and R.T. Cheng. (1992). Semi-implicit finite difference methods for three-dimensional shallow water flow. *International Journal of Numerical Methods in Fluids*, 15, 629–648.

12. Casulli, V. and G. Stelling. (2011). Semi-implicit sub-grid modeling of three-dimensional free-surface flows, *Intl. Journal for Numerical Methods in Fluid Dynamics*, 67, 441-449.

13. Casulli, V. and P. Zanolli. (1998). A three-dimensional semi-implicit algorithm for environmental flows on unstructured grids, Univ. of Oxford. *Methods for Fluid Dynamics* 57-70.

14. Casulli, V. and P. Zanolli. (2005). High resolution methods for multidimensional advection-diffusion problems in free-surface hydrodynamics, *Ocean Modelling* 10, 137–151.

15. Casulli, V. and P. Zanolli. (2012). Iterative Solutions of Mildly Nonlinear Systems. *Journal of Computational and Applied Mathematics*. Elsevier, 2012.

16. Cheney, W. and D. Kincard. (2007). Numerical Mathematics and Computing 6th Edition. Cengage Learning. 2007.

17. Cho, K.-H. (2009). A numerical modeling study on barotropic and baroclinic responses of the Chesapeake Bay to hurricane events. Ph.D. Dissertation, Virginia Institute of Marine Science, College of William and Mary.

18. Craig, P. D., and M. L. Banner (1994). Modeling Wave-Enhanced Turbulence in the Ocean Surface Layer. *Journal of Physical Oceanography*, 24(12), 2546-2559.

19. DiLiberto, T., Colle, B. A., Georgas, N., Blumberg, A., and A. Taylor. (2011). Verification of a multiple model storm surge ensemble for the New York Metropolitan Region., *Wea. Forecasting*. 26, 922-939.

20. FEMA MOTF (Federal Emergency Management Agency Modeling Task Force). (2013). Hurricane Sandy Impact Analysis (https://www.arcgis.com/home/item.html?id=307dd522499d4a44a33d7296a5da5ea0)

21. Flather, R.A., Proctor, R., and J. Wolf. (1991). Oceanographic forecast models. Computer Modeling in the Environmental Sciences. D.G. Famer and M.J. Rycroft (Eds.), Oxford. U.K., 15-30.

22. Forbes, C., Rhome, J., Mattocks, C., and A. Taylor. (2014). Predicting the Storm Surge Threat of Hurricane Sandy with the National Weather Service SLOSH Model. *J. Mar. Sci. Eng*. 2014, 2, 437-476.

23. Gao, J. (2011). A Numerical Modeling Study of Storm Surge and Inundation in the Chesapeake Bay during the November 2009 Mid-Atlantic Nor'easter. Master's Thesis, Virginia Institute of Marine Science, College of William and Mary.

24. Garratt, J.R. (1977). Review of drag coefficients over oceans and continent. *Mon. Weather Rev.* 1977, *105*, 915–929.

25. Garzon, Juan L., Ferreira, Celso. M., Padilla-Hernandez, Roberto. (2018). Evaluation of Weather Forecast System for Storm Surge Modeling in the Chesapeake Bay, *Ocean Dynamics*, Vol. 68, p91-107.

26. Glahn, B., Taylor, A., Kurkowski, N., and W. Shaffer. (2009). The role of the SLOSH model in national weather service storm surge forecasting. *National Weather Digest*, 33(1):3-14.

27. Gottlieb, S., and C.-W. Shu (1998). Total Variation Diminishing {R}unge-{K}utta Schemes. *Mathematics of Computation*, 67, 73-85.

28. Grant, W. D., and O. S. Madsen (1979). Combined Wave and Current Interaction With a Rough Bottom. *J. Geophys. Res.*, 84(C4), 1797-1808.

29. Harris, D.L. (1963). Characteristics of the Hurricane storm surge. Technical Paper No. 48, U.S. Weather Bureau.

30. Hersbach, H., and P. A. E. M. Janssen (1999). Improvement of the Short-Fetch Behavior in the Wave Ocean Model (WAM). *Journal of Atmospheric and Oceanic Technology*, 16(7), 884-892.

31. Holthuijsen, L. H., A. Herman, and N. Booij (2003). Phase-decoupled refraction–diffraction for spectral wave models. *Coastal Engineering*, 49(4), 291-305.

32. Hsu, T.-W., S.-H. Ou, and J.-M. Liau. (2005). Hindcasting nearshore wind waves using a FEM code for SWAN, *Coastal Eng*., 52(2), 177-195, doi:10.1016/j.coastaleng.2004.11.005.

33. Huang, Y., Weisberg, R. H., and L. Zheng. (2010). Coupling of surge and waves for an Ivan-like hurricane impacting the Tampa Bay, Florida region, *J. Geophys. Res*., 115, C12009, doi:10.1029/2009JC006090.

34. Janssen, P. (1991). Quasi-linear Theory of Wind-Wave Generation Applied to Wave Forecasting. *Journal of Physical Oceanography*, 21(11), 1631-1642.

35. Jelesnianski, C.P., Chen, J., and W.A. Shaffer. (1992). SLOSH: sea, lake, and overland surges from hurricanes. National Weather Service, Silver Springs, MD.

36. Von Karman, T. (1930). Mechanische ahnlichkeit und turbulenz. *Goott. Nachr*. 58–76.

37. Keller, J. B. (1958). Surface waves on water of non-uniform depth, *J. Fluid Mech.*, 4(6), 607–614, doi:10.1017/S0022112058000690.

38. Komen, G. J., L. Cavaleri, M. Donelan, K. Hasselmann, S. Hasselmann, and P. A. E. M. Janssen (1994). Dynamics and Modelling of Ocean Waves. Cambridge Univ. Press, New York, 532 pp.

39. Kundu, Pijush K, Cohen, Ira M, and Hu, Howard H. Fluid Mechanics. 3rd Ed. ed. Amsterdam: Elsevier Academic Press, 2004.

40. Lapetina A, Sheng YP. (2015). Simulating complex storm surge dynamics: Three‐dimensionality, vegetation effect, and onshore sediment transport. *Journal of Geophysical Research: Oceans* 120: 7363‐7380.

41. Liu, Z., Wang, H.V., Zhang, J., and D. Forrest. (2014). Large-Scale Storm Tide Modeling in the Mid-Atlantic Bight during Hurricane Sandy, The 17th Biennial Ocean Sciences Meeting in Honolulu from 23-28 February 2014 (conference poster).
42. Liu, Z., Zhang, Y., Wang, H.V., Wang, Z., Ye, F., Huang, H., and M. Sisson. (2018). Impact of small-scale structures on estuarine circulation, *Ocean Dynamics*, https://doi.org/10.1007/s10236-018-1148-6.
43. Loftis, J.D. (2014). Development of a Large-Scale Storm Surge and High-Resolution Sub-Grid Inundation Model for Coastal Flooding Applications: A Case Study During Hurricane Sandy. Ph.D. Dissertation. College of William & Mary.
44. Longuet-Higgins, M. S., and R. W. Stewart (1964). Radiation stresses in water waves; a physical discussion, with applications. *Deep Sea Research and Oceanographic Abstracts*, 11(4), 529-562.
45. Luettich, R. A., and J.J. Westerink. (1999). Implementation of the wave radiation stress gradient as a forcing for the ADCIRC hydrodynamic model: Upgrades and documentation for ADCIRC version 34.12, Dept. of the Army, U.S. Army Corps of Eng., Waterw. Exp. Stn., Vicksburg, Miss: http://www.unc.edu/ims/adcirc/publications/1999/1999_Luettich02.pdf
46. Magnusson, L., Bidlot, J., Lang, S.T., Thorpe, A., Wedi, N., and M . Yamaguchi. (2014). Evaluation of medium-range forecasts for Hurricane Sandy. *Mon. Wea. Rev*., 142, 1962–1981, doi:https://doi.org/10.1175/MWR-D-13-00228.1.

47. Mastenbroek, C., G. Burgers, and P. Janssen (1993). The dynamical coupling of a wave model and a storm surge model through the atmospheric boundary layer. *J. Phys. Oceanogr*. 23, 1856–1867.

48. Mathisen, P. P., and O. S. Madsen (1996). Waves and currents over a fixed rippled bed 2. Bottom and apparent roughness experienced by currents in the presence of waves. *J. Geophys. Res.*, 101(C7), 16543-16550.

49. McCallum, B.E., Wicklein, S.M., Reiser, R.G., Busciolano, R., Morrison, J., Verdi, R.J., Painter, J.A., Frantz, E.R., and A.J. Gotvald. (2013). Monitoring Storm Tide and Flooding from Hurricane Sandy along the Atlantic Coast of the United States, Submitted October 2012. United States Geological Survey Hurricane Sandy Impact Report. http://pubs.usgs.gov/of/2013/1043/pdf/ofr2013-1043.pdf.

50. Mellor, G. (2003). The Three-Dimensional Current and Surface Wave Equations. *J. Phys. Oceanography*, 33(9), 1978-1989.

51. Mellor, G. (2005). Some consequences of the three-dimensional current and surface wave equations. *J. Phys. Oceanography*, 35,2291-2298

52. Mellor, G. L. (2008). The Depth-Dependent Current and Wave Interaction Equations: A Revision. *Journal of Physical Oceanography*, 38(11), 2587-2596.

53. Mellor, G. (2011a). Reply. *Journal of Physical Oceanography*, 41(10), 2013-2015.

54. Mellor, G. (2011b): Wave radiation stress. *Ocean Dynamics*, 61(5), 563-568.

55. Millikan, C. B. (1938). A Critical Discussion of Turbulent Flow in Channels and Circular Tubes. *Proceedings of the 5th International Congress for Applied Mechanics*, Cambridge, MA, 1938, pp. 386–392.

56. National Ocean Service. (1997). Hydrographic survey digital database. Vol. 1, 3rd ed. National Oceanic and Atmospheric Administration: https://ngdc.noaa.gov/mgg/bathymetry/hydro.html

57. National Weather Service (NWS). (2009). November 11-13th, 2009 Nor'easter. National Oceanic and Atmospheric Administration. Retrieved October 14, 2010.

58. NOAA NOS (National Ocean Service). (2006). NOS Hydrographic Survey Data Viewer. Hydrographic survey digital database. NYC Surveys. National Oceanic and Atmospheric Administration. http://maps.ngdc.noaa.gov/viewers/nos_hydro/.

59. NOAA NDBC (National Buoy Data Center). NDBC (2012). Buoy Map for Atmospheric and Oceanic Observations. http://www.ndbc.noaa.gov/.

60. NOAA NGDC (National Geophysical Data Center). (1999). ETOPO1 Global Relief Model. http://www.ngdc.noaa.gov/mgg/global/.

61. NOAA NGDC (National Geophysical Data Center). (2011). 90m Integrated Models of Coastal Relief. http://www.ngdc.noaa.gov/mgg/coastal/grddas01/grddas01.htm.

62. NOAA Service Assessment. (2011). Tropical Cyclone Report: Hurricane Irene, August 21-28, 2011; National Weather Service, NOAA: Silver Spring, MD, USA, 2011.

63. NOAA Service Assessment. (2012). Hurricane/Post-Tropical Cyclone Sandy, October 22–29, 2012; National Weather Service, NOAA: Silver Spring, MD, USA, 2012.

64. Orton, P., Georgas, N., Blumberg, A., and J. Pullen. (2012). Detailed modeling of recent severe storm tides in estuaries of the New York City region, *J. Geophys. Res*., 117, C09030, doi:10.1029/2012JC008220.

65. Pawlowicz, R., Beardsley, B., and S. Lentz. (2002). Classical tidal harmonic analysis including error estimates in MATLAB using T_TIDE. *Computers Geosciences*. 28, 929-937.

66. Phillips, O. M. (1977). The Dynamics of the upper Ocean, Cambridge University Press, pp. 336.

67. Prandtl, L. (1933). Neuere Ergebnisse der Turbulenzforschung. Z. Ver. Dtsch. Ing., 77, pp. 105 – 114 (translated as NACA Technical Memorandum 720).

68. Pond, S. and G.L. Pickard. (1998). Introductory Dynamical Oceanography. Butterworth-Heinmann.

69. Rogers, E., Y. Lin, K. Mitchell, W.-S. Wu, B. Ferrier, G., Gayno, M. Pondeca, M. Pyle, V. Wong, and M. Ek, (2005). The NCEP North American mesoscale modeling system: final eta model/analysis changes and preliminary experiments using the WRF-NMM. Preprints, *21st Conf. on Wea. Analysis and Forecasting/17th Conf. on Numerical Wea. Prediction*, Washington, DC, Amer. Meteor. Soc., CD-ROM, 4B.5.

70. Roland, A. (2009). Development of WWMIII II: Spectral wave modeling on unstructured meshes, Ph.D. thesis, Inst. of Hydraul. and Water Resour. Eng., Tech. Univ. Darmstadt, Darmstadt, Germany.

71. Roland, A., Zhang, Y., Wang, H.V., Meng, Y., Teng, Y., Maderich, V., Brovchenko, I., Dutour-Sikiric, M., and U. Zanke. (2012). A fully coupled wave-current model on unstructured grids. *J. Geophys. Res.* 2012, *117*, doi:10.1029/2012JC007952.

72. Shapiro, R. (1970). Smoothing, filtering, and boundary effects. *Rev. Geophys*., 8(2): 359-387.

73. Sheng, Y. P., V. Alymov, and V. A. Paramygin. (2010). Simulation of storm surge, wave, currents, and inundation in the Outer Banks and Chesapeake Bay during Hurricane Isabel in 2003: The importance of waves, *J. Geophys. Res.*, 115, C04008, doi:10.1029/2009JC005402.

74. Stephens, S.A., Coco, G., and Bryan, K.R. (2011). Numerical Simulations of Wave Setup over Barred Beach Profiles: Implications for Predictability. *J. Waterw. Port Coast. Ocean Eng*, 137, 175–181.

75. Svendsen, I. A. (2006). Introduction to nearshore hydrodynamics, *Advanced Series on Ocean Engineering*, Singapore, World Scientific, 24, pp. 772.

76. Teng, Y.-C. (2012). Developing an Unstructured Grid, Coupled Storm Surge, Wind Wave and Inundation Model for Super-Regional Applications. Ph.D. Dissertation, Virginia Institute of Marine Science, College of William and Mary.

77. Thacker, W.C. (1981). Some exact solution to the nonlinear shallow water equations. *Journal of Fluid Mechanics*, vol. 107, p499-508.

78. Thuburn, J., Ringler, T.D., Skamarock, W.C., Klemp, J.B. (2009). Numerical representation of geostrophic modes on arbitrarily structured C-grids, *Journal of Computational Physics*, 228 (22), 8321-8335.

79. Tolman, H. L. (1992). Effects of Numerics on the Physics in a Third-Generation Wind-Wave Model. *Journal of Physical Oceanography*, 22(10), 1095-1111.

80. Umlauf, L. and H. Burchard. (2003). A generic length-scale equation for geophysical turbulence models. *J. Mar. Res*. 6, 235–265.

81. U.S. Army Engineer Research and Development Center. (2015). North Atlantic Coast Comprehensive Study (NACCS) Coastal Storm Model Simulations: Waves and Water Levels, pp. 1-246, US Army Corps of Engineers, Washington, DC, USA.

82. U.S. Department of Defense. (1999). Digital nautical chart. National Imagery Mapping Agency, Washington, DC.

83. USGS. Sandy Flood Event Viewer. (2013). https://stn.wim.usgs.gov/fev/#Sandy

84. USGS. High Water Mark Data during Sandy. (2017). https://wim-project-data-east.s3.amazonaws.com/data/Sandy/USGS_hurricane_sandy_data.mdb

85. Volp, N.D., B.C. Prooijen, and G.S. Stelling. (2013). A finite volume approach for shallow water flow accounting for high resolution bathymetry and roughness data", *Water Resources Research*, 49(7), 4126-4135.

86. Wang, H.V., Loftis, J.D., Liu, Z., Forrest, D., and J. Zhang. (2014). The Storm Surge and Sub-Grid Inundation Modeling in New York City during Hurricane Sandy. *J. Mar. Sci. Eng.* 2014, *2*, 226-246, doi:10.3390/jmse2020437.

87. Wang, H., Loftis, J.D., Forrest, D., Smith, W., and B. Stamey. (2015). Modeling Storm Surge and inundation in Washington, D.C., during Hurricane Isabel and the 1936 Potomac River Great Flood. *Journal of Marine Science and Engineering*, 3(3), 607-629.

88. Weaver, R. and R. Luettich, Jr. (2010). 2D vs. 3D Storm Surge Sensitivity in ADCIRC: Case Study of Hurricane Isabel. *Estuarine and Coastal Modeling*: pp. 762-779. doi: 10.1061/41121(388)44.

89. Weisberg, R.H. and L. Zheng. (2008), Hurricane storm surge simulations comparing three-dimensional with two-dimensional formulations based on an Ivan-like storm over the Tampa Bay, Florida region, *J. Geophys. Res*. 113, C12001, doi:10.1029/2008JC005115.

90. Westerink, J.J., Luettich, R.A., and J. Muccino. (1994). Modeling tides in the western North Atlantic using unstructured graded grids. *Tellus* 46A: 178-199.

91. Xia, H., Z. Xia, and L. Zhu (2004). Vertical variation in radiation stress and wave-induced current. *Coastal Engineering*, 51(4), 309-321.

92. Yanenko, N. N. (1971). The method of fractional steps. Springer-Verlag.

93. Zeng, X., Zhao, M., and R.E. Dickinson. (1998). Intercomparison of bulk aerodynamic algorithms for the computation of sea surface fluxes using TOGA COARE and TAO data. *J. Clim*. 11, 2628–2644.

94. Zhang, H., O. S. Madsen, S. A. Sannasiraj, and E. Soon Chan (2004). Hydrodynamic model with wave–current interaction in coastal regions. *Estuarine, Coastal and Shelf Science*, 61(2), 317-324.

95. Zhang, Y.L., Baptista, A.M., and E.P. Myers. (2004). A cross-scale model for 3D baroclinic circulation in estuary–plume–shelf systems: I. Formulation and skill assessment. *Cont. Shelf Res.* 24, 2187-2214.

96. Zhang, Y. and A.M. Baptista. (2008). SELFE: A semi-implicit Eulerian-Lagrangian finite-element model for cross-scale ocean circulation, *Ocean Model.* 2008, *21*, 71–96.

97. Zhang, Y., Ateljevich, E., Yu, H-C., Wu, C-H., and J.C.S. Yu. (2015). A new vertical coordinate system for a 3D unstructured-grid model, *Ocean Modelling*, 85, 16-31.

98. Zhang, Y., Ye, F., Stanev, E. V., and S. Grashorn. (2016). Seamless cross-scale modeling with SCHISM, *Ocean Modelling*, 102, 2016, 64-81.

99. Zheng LY., R.H. Weisberg, Y. Huang, R. A. Luettich, J. J. Westerink, P. C. Kerr, A. Donahue, G. Crane, and L. Akli (2013). Implications from the comparisons between two- and three-dimensional model simulations of the Hurricane Ike storm surge. *Journal of Geophysical Research* 118: 3350-3369.

VITA

Zhuo Liu

Zhuo was born in Dalian, China. He earned a Bachelor of Science degree in Marine Science from Xiamen University in 2012. He entered Master of Science program in Marine Science of the College of William and Mary, School of Marine Science at the Virginia Institute of Marine Science in the Fall of 2012, and then bypassed to Ph.D. program in Marine Science in February 2015. In March 2018, he started to work as Hydrodynamic Modeler at Texas Water Development Board in Austin, Texas.